Computer Simulation of Biological Ion Channels

Matthew Hoyles

September, 1999

A thesis submitted for the degree of Doctor of Philosophy of The Australian National University

This thesis is my own original work, however it incorporates material which has been previously published in scientific papers of which I am a joint author (see the list of publications). My main role in the collaborative project which this thesis describes was the design, implementation, and testing of the algorithms for solving Poisson's equation. Thus I am primarily responsible for the work described in chapters 3, 4, and 6, except for the derivation of the analytical solution described in section 4.1, for which Serdar Kuyucak is primarily responsible. I participated in all aspects of the project, including making improvements to the Brownian dynamics techniques described in chapter 5, designing the model channels, and helping to analyze and understand the results described in chapters 5, 7, and 8, for instance by developing the technique for generating multi-ion energy profiles. Chapters 1, 2, and 9, as well as the discussion sections in chapters 5, 7, and 8, are newly written for this thesis. They represent my own interpretation of the results of the simulations, and my own views on the aims and significance of the project and possible future directions.

Matthew Hoyles

To my parents

Acknowledgments

Thanks to my supervisors, Serdar Kuyucak and Shin-Ho Chung, for their patience and understanding. Thanks to my other collaborators, Toby Allen and Sandy Li, for helping to make the project a success. Thanks to Janey Wood for helping to prepare the figures for this thesis. Thanks to my brother, Daniel Hoyles, and Arrow Consulting, for paying me a retainer when the money ran out. And finally, thanks to my parents, for their unfailing support over the years. This thesis is dedicated to them.

Abstract

This thesis describes a project in which algorithms are developed for the rapid and accurate solution of Poisson's equation in the presence of a dielectric boundary and multiple point charges. These algorithms are then used to perform Brownian dynamics simulations on realistic models of biological ion channels. An iterative method of solution, in which the dielectric boundary is tiled with variable sized surface charge sectors, provides the flexibility to deal with arbitrarily shaped boundaries, but is too slow to perform Brownian dynamics. An analytical solution is derived, which is faster and more accurate, but only works for a toroidal boundary. Finally, a method is developed of pre-calculating solutions to Poisson's equation and storing them in tables. The solution for a particular configuration of ions in the channel can then be assembled by interpolation from the tables and application of the principle of superposition. This algorithm combines the flexibility of the iterative method with greater speed even than the analytical method, and is fast enough that channel conductance can be predicted. The results of simulations for a model single-ion channel, based on the acetylcholine receptor channel, show that the narrow pore through the low dielectric strength medium of the protein creates an energy barrier which restricts the permeation of ions. They further show that this barrier can be removed by dipoles in the neck of the channel, but that the barrier is not removed by shielding by counter-ions. The results of simulations for a model multi-ion channel, based on a bacterial potassium channel, show that the model channel has conductance characteristics similar to those of real potassium channels. Ions appear to move through the model multi-ion channel via rapid transitions between a series of semi-stable states. This observation suggests a possible physical basis for the reaction rate theory of channel conductance, and opens up an avenue for future research.

List of Publications

Hoyles, M., S. Kuyucak, and S.-H. Chung. 1996. Energy barrier presented to ions by the vestibule of the biological membrane channel. *Biophys. J.* 70:1628–1642.

Kuyucak, S., M. Hoyles, and S.-H. Chung. 1998. Analytical solutions of Poisson's equation for realistic geometrical shapes of membrane ion channels. *Biophys. J.* 74:22–36.

Li, S. C., M. Hoyles, S. Kuyucak and S.-H. Chung. 1998. Brownian dynamics study of ion transport in the vestibule of membrane channels. *Biophys. J.* 74:37–47.

Hoyles, M., S. Kuyucak, and S.-H. Chung. 1998a. Computer simulation of ion conductance in membrane channels. *Phys. Rev. E.* 58:3654–3661.

Hoyles, M., S. Kuyucak, and S.-H. Chung. 1998b. Solutions of Poisson's equation in channel-like geometries. *Computer Phys. Commun.* 115:45–68.

Chung, S.-H., M. Hoyles, T. W. Allen, and S. Kuyucak. 1998. Study of ionic currents across a model membrane channel using Brownian dynamics. *Biophys. J.* 75:793–809.

Chung, S.-H., T. W. Allen, M. Hoyles, and S. Kuyucak. 1999. Permeation of ions across the potassium channel: Brownian dynamics studies. *Biophys. J.* 77:2517–2533.

Allen, T. W., M. Hoyles and S. Kuyucak, and S.-H. Chung. 1999. Molecular and Brownian dynamics study of ion selectivity and conductivity in the potassium channel. *Chem. Phys. Lett.* 313:358-365.

Contents

List of Figures

Chapter 1

Ion Channels

The project described by this thesis is an effort to improve the understanding of ion channels by devising methods of computer simulation that can predict channel conductance from channel structure. Ion channels are an essential part of the molecular machinery of life, performing a role in biological information systems analogous to that of transistors in artificial information systems. They are the fundamental amplifiers, transducers, and regulators of the nervous system and the reactive tissues attached to it. Many of the roles that ion channels play are now understood, thanks to decades of careful electrophysiological research, culminating in the patch-clamp technique which can measure the current through a single channel. The structures of ion channels are less well known, but a recent breakthrough has revealed the detailed molecular structure of one type of potassium channel, and the structures of more channels may soon follow. What is missing from this picture are physical theories that predict channel function from channel structure. Without such theories we cannot claim to understand *how* ion channels work.

Although the lack of detailed channel structures has impeded the development of such theories, a more fundamental difficulty is the physical complexity of describing a working ion channel. The size of ion channels (typically 50–100 Å long) places them in the grey area between the statistical laws of physics used for bulk materials, and the atomic laws used for individual atoms and molecules. Ion channels are small enough that interactions between individual atoms are likely to be important to their operation, but large enough that calculation of all such interactions is impractical. In addition, ion channels are biological objects, the product of a billion or more years of evolution. The process of natural selection can be expected to have improved their efficiency and effectiveness by all available means, very likely operating on multiple scales and using multiple physical effects. We should expect ion channels to be sophisticated pieces of molecular machinery, not simple holes in the cell membrane.

As a result of this complexity, most physical descriptions of ion channel operation (including this one) rely on computer simulations or computer calculations. Computers are good at performing complex calculations, and are the tool of choice for attacking an intrinsically complex problem such as this. While a simple analytical theory would be easier to use and give a clearer intuitive picture, the complexity of the problem means that such a construct is unlikely to be found. A good simulation technique may be an acceptable alternative. Graphical visualization can assist in gaining intuition from a simulation, and powerful desktop computer systems (with good graphics) are now common. The most important requirement of a theory is that it make testable, non-obvious predictions about the system it attempts to describe, rendering it potentially both falsifiable, if its predictions are contrary to experiment, and useful, if its predictions agree with experiment. The method by which the predictions are made is not so important, as long as it can be accurately described and reproduced. Unfortunately, even using a modern supercomputer (as for this project), simplifying assumptions need to be made for conductance to be predicted. Simplifying assumptions are undesirable at this stage because they are dangerous. We do not yet know which aspects of the physical reality of ion channels are important to their operation and which are incidental. Making too many assumptions will likely result in something important being missed, and it may be impossible to track down which assumption is responsible. However, the ultimate test of any theory is comparison with experiment, which in the case of ion channels means single channel currents from patch-clamp recordings. If too few assumptions are made the theory will be unable to predict the conductance of a model channel, and comparison with experiment will be impossible.

Of course an ideal theory should not include irrelevant details which introduce unnecessary complexity and detract from understanding. It should rather capture the essence of the problem and nothing else. However, at this stage I do not think that anyone knows what the essence of ion channel operation is. The many contradictory ideas presented in the second (more theoretical) part of Hille's *Ionic Channels of Excitable Membranes* [31] illustrate this point, giving the impression of an unassembled jigsaw puzzle, with pieces missing, and perhaps some extras thrown in: each individual piece makes sense, but the pieces do not fit together. It is to Hille's credit that he does not prematurely attempt to force these ideas into a coherent framework, but simply presents them, so giving a true picture of the state of the field.

The strategy we use in this project is to ignore the quest for elegance to start with, and build the most comprehensive computer simulation of an ion channel that current hardware and the requirement to predict conductance allow. The presence of a modern supercomputer at the ANU and my own background in computer science make this strategy practical. Any theory that works, that successfully predicts conductance from structure, will

produce an increase in our understanding of ion channels, no matter how complex or cumbersome that theory is. This increased understanding can then be used to develop more elegant and usable theories, as our intuition will be strengthened, and the effect of simplifications can be controlled by comparison with the original, complicated theory. This is not, however, a pure brute-force approach. To make the simulations last long enough to predict conductance (several microseconds of simulated time), we are forced to abstract away most of the atomic detail of the system, and use macroscopic electrostatic theory to recover the long range forces.

The rest of this chapter describes ion channels further: their roles in biological systems, the mechanisms they use to perform these roles, and their structures as far as is known. The information is taken for the most part from Refs. [31, 51]. Chapter 2 delves into the physics of ion channel conductance, and discusses some of the existing theories of the same, and their shortcomings. It explains the reasoning behind our choice of simulation method: three-dimensional Brownian dynamics. A consequence of this choice is the need to use continuum electrostatic theory to calculate long range forces between ions in the simulation. Doing so rapidly enough to let the simulation predict conductance was the major technical problem of the project. Chapter 3 describes the problem and an iterative method of solution that works, but is far too slow. Chapter 4 describes an analytical method of solution that is fast enough to allow limited Brownian dynamics simulation, but restricts the shape of the model channel to a torus. Chapter 5 describes the Brownian dynamics algorithm itself, and the first simulation results using the analytical method for the electrostatic calculations. The tracks of ions placed in the channel indicate that there is an energy barrier for ions crossing the channel, which can be removed by the appropriate placement of fixed charges inside the wall of the channel. Chapter 6 describes an algorithm where the electrostatic calculations are done in advance, stored in tables, and looked up rapidly during simulation. This at last renders the simulation fast enough to predict conductance, and at the same time allows the use of the more flexible iterative method of electrostatic calculation (from chapter 2). Chapter 7 describes Brownian dynamics simulations for a catenary channel using this new method. The conductance results are encouraging, being reminiscent of those from real channels. In chapter 8 we use our methods to build a model based on a recently discovered potassium channel structure. The conductance characteristics of the model are recognizably those of a multi-ion channel: the model channel's conductance shows both rectification and saturation. In addition the *way* that the model conducts is interesting, in that it suggests a possible physical basis for the success of reaction rate theory in channels (the usual physical justification for reaction rate theory is doubtful when the theory is applied to channels). Chapter 9 summarizes the strengths and weaknesses of our theory, and discusses the avenues for future research opened up by its application to the

potassium channel, and by the insights about channel conductance that it has yielded.

1.1 The Role of Ion Channels

It is the nature of biological systems that they have a purpose: they play some role in helping the organism that they are part of survive in the world. The roles that ion channel play are varied, and some are yet to be discovered, but one theme appears dominant, and has been extensively studied: that of rapid signalling in animal cells. All ion channels do roughly the same thing, namely transport ions rapidly across a biological membrane. A channel with this property alone would not be very useful (except for killing cells: some antibiotics are simple channels of this type). Channels typically have two other properties: firstly, they are selective about the ions that they transport, secondly, they open and close in response to external stimuli (or rather the stimuli alter the probability with which they open and close).

Different types of ion channel have different characteristics of conductance, gating, and selectivity, and do different jobs in the signalling process. The genetic sequences of many types of channels have been found, forming a family tree which gives clues about their evolutionary origins. The genetic sequence dictates the protein sequence, which dictates the three-dimensional structure of the channel. The structure in turn gives rise to the characteristics of the channel, via the operation of the laws of physics and chemistry. The prediction of three-dimensional structure from protein sequence is one of the great unsolved problems of biology. Channel structure has to be determined by other means, as has been done most recently by x-ray crystallography. The prediction of channel characteristics from channel structure is another unsolved problem, one that this project aims to address, at least in part. On the other hand, the functional characteristics of ion channels can be measured by experiment, and given these, the way in which channels interact with the cell membrane to provide rapid intercellular signalling is now understood, at least in general terms. This section provides a brief summary.

Cells are the smallest self-contained unit of life and are defined by the membrane that surrounds them. This membrane gives a cell an interior volume which concentrates biological molecules, and can be regulated to provide conditions different from the exterior environment. Biological systems without a membrane, such as some viruses, can only reproduce by taking over an existing cell. It seems that cells and membranes are essential for life. As well as dividing the inside of cells from the outside, membranes provide a home for many types of proteins, including those, like ion channels, that transport through the membrane molecules that otherwise could not pass. The simplest cells, the prokaryotes (such as bacteria), have a cell

membrane, a rigid cell wall, and possibly an outer membrane, but their interior is an unstructured biological soup. In contrast eukaryotic cells (virtually all multicellular life, as well as single celled animals and plants) have a complex internal structure, with multiple internal membranes defining organelles which perform specialized functions, and an internal framework, the cytoskeleton, which provides organization and transport.

The cell membrane (and other biological membranes) are made of a double layer of molecules called phospholipids. These molecules have a long oily tail attached to a compact polar or charged head. Their heads are attracted to water (are hydrophilic) while the tails are repelled by it (are hydrophobic), so the phospholipids arrange themselves into a double layer, with the tails in the middle and the heads on the outside. The membrane is like a two-dimensional liquid: hydrophobic forces hold it together, preventing the phospholipids from leaving the plane, but the phospholipids and other molecules can drift around freely within the membrane. Proteins that span the membrane, such as ion channels, have a hydrophobic middle and hydrophilic ends. This anchors them in the plane of the membrane and prevents them from flipping, but does not prevent them from drifting: many such proteins, however, are connected to the cytoskeleton, which does prevent them from drifting. Other proteins emerge from one or other side of the membrane, or are even enclosed by it. Some of these are free to drift and act as messengers or transport within the membrane.

Biological membranes block ions. Other small molecules, such as dissolved gases, steroid hormones, and even individual water molecules, can cross the membrane by dissolving into the lipid layer and drifting across to the other side. There are gaps between the lipid tails, and enough flexibility to let these small molecules pass. But ions have an unbalanced charge, which strongly coordinates the immediately surrounding layer of water molecules (the first hydration shell), and interacts with at least two further layers of water. All of this water has to be stripped off for the ion to enter the lipid layer, which costs a large amount of energy. The non-polar lipids do not interact with the ion, and so do not replace the energy, with the result that the membrane is effectively impermeable to ions. Since ions are the charge carriers in aqueous solutions, this means that biological membranes are insulators, and being very thin, are excellent capacitors. In prokaryotes the cell membrane is used to store and convert energy: glucose is broken down and the energy is stored as an electrical potential across the membrane, then converted to chemical energy by protons moving down the electrical gradient inside specialized proteins. This is why antibiotics that let ions cross the bacterial membrane are so effective: they collapse the membrane potential and starve the cell. In eukaryotes energy generation is done internally by the mitochondria, organelles believed to be descended from bacteria. This leaves the outer membrane free for other tasks.

One such task is intercellular signalling, achieved by waves of depolar-

ization traveling along the cell membrane. The polarization, or electric potential across the membrane, is set up by a combination of ion pumps and potassium channels. Like all ion channels, potassium channels are passive transporters: they let ions cross the membrane but do not impel them. The ions cross if the electric potential or concentration gradient favors it, not otherwise. Ion pumps, in contrast, are active transporters, working against the concentration gradients by spending cellular energy. The ion pumps concentrate potassium ions inside the cell, while ejecting sodium ions into the extra-cellular solution. They transport five ions at once, ejecting three sodium ions for every two potassium ions brought in. Since both sodium and potassium ions have a single positive charge, this creates an electric potential across the membrane, making the inside of the cell more negative than the outside.

Potassium channels regulate this potential. Potassium ions can leave (or enter) the cell through the potassium channels because the electrical and concentration gradients are nearly in balance. They stop flowing when their tendency to leave the cell because of the high concentration inside is matched by their tendency to enter the cell because of the electrical driving force. Thus open potassium channels have a stabilizing effect on the membrane potential. There are a bewildering variety of potassium channels, expressed in different types of cells, and with subtly different gating characteristics. The main theme seems to be stabilization of the membrane potential when needed (during the depolarization cycle of the membrane), but closure at other times, to minimize the flow of ions and conserve energy. Of course, for the sodium ions, concentrated on the outside, the concentration and electrical gradients are pushing in the same direction, into the cell. This is the basis of the depolarization mechanism.

The depolarization wave is started by ligand-gated cation channels. These channels open in response to the presence of a neurotransmitter, a chemical signal outside the cell, and allow sodium ions to enter, locally depolarizing the membrane. After a short time the ligand-gated channels close, either because their triggering chemical has been mopped up, or because they inactivate, closing and becoming insensitive to the triggering chemical until concentrations of it fall and they reset. Before this happens, however, the depolarization is propagated by voltage-gated sodium channels. These open in response to a drop in membrane potential and allow more sodium to enter, amplifying and spreading the signal. Voltage-gated sodium channels also inactivate, shutting down once they have completed their task. At about the time the sodium channels inactivate, extra voltage-gated potassium channels open. These delayed rectifiers are also triggered by a drop in membrane potential, but take longer than the sodium channels to respond to it. They quickly restore the membrane potential, resetting the voltage-gated sodium channels and preparing the membrane for the next pulse. When the depolarization reaches its destination, voltage-gated calcium channels open and

allow calcium to enter the cell, again in response to the drop in membrane potential. Calcium is a divalent cation, concentrated outside the cell by another set of ion pumps. Its presence inside the cell is a signal for the cellular machinery to perform some action, for instance a muscle cell to contract, or a nerve cell to release neurotransmitter and signal to an adjacent cell.

The advantage of this signalling mechanism is speed of operation: nerve cells can fire up to 1000 times per second. Ion channels work far more quickly than ion pumps: a typical ion pump processes 10 ions per second, compared to 10^6-10^7 ions per second for a typical ion channel. However, the number of sodium or potassium ions needed to polarize or depolarize the membrane is small compared to the total number of ions in the cell: the passage of a single wave does not upset the concentration differences much. Thus a small number of ion channels rapidly alter the membrane potential, to achieve high signalling speed, while a large number of ion pumps slowly and continuously move ions to maintain the appropriate concentrations: potassium on the inside, and sodium on the outside.

1.2 Ion Channel Function

The function of ion channels is conductance, modified by selectivity and gating. Conductance is the rapid transport of ions down the free-energy gradient, and ion channels do transport ions rapidly, with individual channels generating a current in the picoampere range by moving millions or tens of millions of ions per second. Selectivity is the preference, or specificity, for particular types of ions. Most ion channels select on valence, transporting for instance only cations, or anions, or divalent cations. Some are much more specific, such as potassium channels, which maintain the membrane potential by transporting potassium ions while blocking sodium ions, despite these both being monovalent cations of similar size. Gating is the ability to open and close in response to external stimuli. All channels open and close at random, and some have sub-conductance states, where they conduct at less then their maximum, but the probabilities of opening and closing, and average times spent open and closed, are influenced by the external stimuli. Averaged over many channels the effect is the same as if the channels were being reliably opened and closed on command.

These channel functions can be, and have been, studied by the patch-clamp technique. This involves attaching a micropipette to the surface of the cell by suction, isolating the solution inside the pipette and the patch of membrane covered by it from the rest of the system. The high resistance and small size of the patch reduces the electrical noise to the level where the current from a single channel can be recorded. Variations on this technique include pulling the patch off the cell to vary the bathing solution on the cytoplasmic side, and increasing the suction to breach the membrane,

then recording current for the whole cell, not just a small patch. Controlled experiments can be done to investigate all aspects of channel function: the conductance and selectivity of a channel under different concentrations of ions and different electrical potentials, and the pattern of opening and closing of individual channels under the influence of various stimuli. This wealth of experimental data should make it easy to test theories of channel mechanism. Knowledge of channel structure is not so well advanced, however, and theories based on the detailed physics of channels have difficulty predicting conductance.

The most striking aspect of channel conductance is the ability of an individual channel to carry picoamperes of current, enough to be individually measured by the patch-clamp apparatus. Other types of transport proteins, and the vast majority of enzymes, operate much more slowly, performing from 10 to 1000 actions (transportations or reactions) per second. These slower proteins use mechanisms of tight binding to their substrates and conformational change. In other words the whole protein reshapes itself while the substrate hops between well defined positions or states. The much higher rate at which ion channels operate (one picoampere is equivalent to around six million monovalent ions per second) strongly suggests that a different mechanism is responsible. The only mechanism known to operate at these speeds is diffusion, drift due to the random thermal motion of molecules. This would explain why all channels are unpowered, relying on electrical and concentration gradients to drive the ions. Diffusion involves many possible positions for an ion crossing the channel, and without an ion binding to a particular location a protein could not assist its transport by a chemically powered conformational change. A diffusive conductance mechanism implies a water filled pore through the channel, to provide the ions with the necessary freedom of motion, and structural studies do show evidence of such pores (hence the name channel). The diffusive mechanism is widely accepted, but some theories still suggest mechanisms involving tight binding to particular locations (binding sites) and hopping between these sites.

Another important aspect of channel conductance is the role of electrostatic interactions between the ion and the channel. It is easy to think of the membrane as a mechanical barrier to ions, and a channel as a hole in the membrane, large enough for the ion to fit through, but this simple picture is not enough to explain channel conductance. The membrane itself is flexible and contains gaps large enough to contain the ion, if it were not for the surrounding coordinated water. For an ion to pass through a channel some of this water must be stripped off. In the less selective channels the pore is wide enough for the ion to keep its first hydration shell, but selectivity between ions of the same valence requires contact between the protein and the ion, implying that at least some of the first shell is removed. The first shell contains most of the coordination energy, but the remainder in the

second and third shells is enough to effectively block transport. If the ion is to pass, this energy must be replaced by interaction with the channel. Energy lost by intruding into the first shell could be replaced by polar groups, such as carbonyl, in contact with the ion. This mechanism is seen in the channel formed by the antibiotic gramicidin, which has a known structure and has been extensively studied. Energy lost by the stripping of the second and third shells could be replaced by longer range interactions with fixed charges or large dipoles in the protein wall. The membrane is an electrostatic barrier to the passage of ions, so a channel must somehow create an electrostatic hole in the barrier.

The mechanism of selectivity depends on the mechanism of conductance. Selectivity can be explained by a binding site which is specific for a particular species of ion, as seen in ion carriers, another type of antibiotic. An ion carrier works by wrapping itself around an ion on one side of the membrane and drifting across to the other side before releasing the ion. Ion carriers are very specific to a particular ion, but they are around ten thousand times slower than a channel. The speed of the channel suggests a diffusive mechanism, which means that selectivity cannot be produced by a binding site. An alternative hypothesis is a selectivity filter, a narrow region of the channel which intrudes into the first hydration shell, replacing some of its water with polar groups. In bulk solution the water molecules in the first shell adjust themselves to the size of the ion, but pieces of protein would be more constrained. They could be arranged to replace all the hydration energy for a particular species of ion, but not for other types of ion of slightly different sizes. So for the preferred ion, the selectivity filter strips off some of the water in the first shell, but replaces the energy by interaction with the polar groups. The filter provides not a binding site, but a continuous path for diffusion, free of sharp energy barriers which would impede the ion, or sharp energy wells which would trap it. For ions other than the preferred one the filter would still remove the water, but would not do as good a job of replacing the energy, producing an energy barrier.

Selectivity between ions of the same valence in diffusive channels is an interesting topic, but not one that can be readily studied by the Brownian dynamics simulations described in this thesis. Molecular dynamics simulations are needed to study the short range interactions involved. In Brownian dynamics these are abstracted into the random force, so any selectivity between ions of the same valence must be built into the simulation method, rather than emerging from the model structure. Ions of different valence, however, have different long range electrostatic effects, which could be involved in selection among them. For example, if fixed charges or large dipoles are used in channels to replace energy from the outer hydration shells, these would be specific to cations or anions. For ions of the opposite polarity the dipoles would add to the energy barrier rather than canceling it, leading to a channel specific to one polarity of ion. This hypothesis could explain the

selectivity of non-specific cation channels, such as most ligand-gated channels, but for other types of channels more complex mechanisms seem to be in operation. Calcium channels are specific for divalent cations, blocking the monovalent sodium ions *unless* there are no divalent cations present, in which case they conduct sodium ions perfectly well. Anion channels are not very selective among anions, and furthermore they allow some cations to pass, but only in the presence of permeant anions. These conductance characteristics can be explained by theories involving multiple interacting ions in a channel with binding sites, but this is inconsistent with the diffusive mechanism needed to explain rapid transport. If these characteristics or selectivity between ions of different valence are due to long range interactions between ions and the protein, then they can certainly be investigated by the methods described here.

Gating, and channel kinetics in general, is another topic that our Brownian dynamics simulations cannot examine directly. The pattern of channel opening and closings seen on a patch clamp recording occurs over a period of tens to thousands of milliseconds, while our current methods can only manage the several microseconds of simulation time needed to predict conductance. Channel gating seems, in most cases, to be accomplished by a conformational change in the protein structure which occludes the aqueous pore, preventing the passage of ions. The view of the channel as a hole in an electrostatic barrier raises the possibility of an electrostatic gating mechanism, where a conformational change would shift fixed charges within the protein so as to reestablish the barrier. It has been suggested that such a mechanism would change a cation channel into an anion channel or vice-versa, but this is not necessarily the case: the membrane barrier shows that electrostatic effects can block ions of both valences. There is, however, no experimental evidence that any channel uses such a mechanism. Other types of channel kinetics, which may not be due to conformational change, are the rapid flickering shown by some types of channel, and the subconductance states (periods of reduced conductance during a long open interval) exhibited by ligand gated anion channels. It is possible that these are caused by interaction between ions in a multi-ion channel: this is suggested by the dependence of some of these effects on the concentration or type of ions in the bathing solution.

1.3 Ion Channel Structure

In order to test if a theory makes accurate predictions from a channel structure, details of that structure need to be known, especially details about the structure of the pore. For a theory based on long range electrostatics, such as the Brownian dynamics simulations described here, the important information is the geometry of the pore and the position and strengths of fixed

charges and large dipoles. The nature of the pore lining is also important, that is whether it is hydrophobic or hydrophilic (covered in small dipoles). For a theory based on short range interactions between molecules, such as molecular dynamics simulations, more information is needed, namely the detailed three dimensional structure of the amino acid residues that make up the protein.

The usual method of determining the three dimensional structure of a protein is x-ray crystallography: the protein is crystallized, then x-ray diffraction patterns are produced from various angles and analyzed to recover the molecular structure. Channels are difficult to crystallize since they are only stable in their usual form when part of a membrane, so until recently other methods such as electron microscopy and hydropathy plots have been used to gain some idea of channel structure. These methods show that the overall structure of a channel is a bundle of four or five protein sub-units which cross the membrane: the pore is formed out of the gap between them. In some channels the sub-units are identical, while others are made of a mixture of slightly different types. The four sub-unit channels are usually voltage gated and highly selective, while the five sub-unit channels are ligand gated and less selective. Gene sequences show that within each type the channels are related. Whether the four and five unit channels are related is not yet known. This section gives a brief description of the structure of two channels: firstly the acetylcholine receptor, a ligand gated channel, and secondly the KcsA channel, a bacterial channel of the four sub-unit type, and one of the very few channels whose structure has been determined by x-ray crystallography [21].

The most studied ligand gated channel is the nicotinic acetylcholine receptor of the electric ray (Torpedo californica), a non-selective cation channel. Electric rays use these channels to power their electric pulse, and so produce them in very large quantities, which has allowed the channels to be separated and purified. Despite their unconventional use, gene sequencing shows that these ACh receptors are very similar to those of other species, which are used to activate muscle contraction. ACh receptors have five sub-units, two each of the type called α and one each of types β, γ, and δ. The α sub-units contain the ligand binding sites: it takes two molecules of acetylcholine to activate an ACh receptor. The overall structure of these channels has been determined [70]. The channels were packed into a two dimensional lattice, and electron micrographs of the lattice were analyzed by crystallographic methods, yielding a low resolution picture. ACh receptors take the form of an hourglass, with large bell-shaped vestibules extending away from the membrane, by 60 Å on the extracellular side, and 20 Å on the cytoplasmic side. Both vestibules are about 12.5 Å in radius at their mouths, and narrow towards the membrane crossing pore. Overall the channel is about 100 Å long. The pore is too narrow to be resolved on the micrographs, but electrophysiology indicates that its minimum radius is around 6 Å, since

this is the radius of the largest organic ion that can be pushed through the channel.

Indirect methods have been used to deduce a rough position for some of the charged protein residues in the ACh receptor [71]. The protein sequences were analyzed using a hydropathy plot: by allocating each residue a hydrophobicity number, indicating whether it would be more likely to be found surround by lipids or by water, four membrane spanning segments were identified. These segments are assumed to form alpha helices, the usual secondary structure in a hydrophobic environment, and under this assumption they are about the right length to cross the membrane. Studies using point mutagenesis have identified one of these, the M2 segment, as providing the lining of the pore. In point mutagenesis, the channel is cloned, but one of its residues is swapped for an alternative by altering the genetic sequence. The function of mutant channels produced by the altered code can then be compared with the function of channels of the wild type. Any changes give information about the role of the modified residue. In the case of the M2 segment several residues were identified that affect the operation of toxins which block the pore by binding to its wall. Other, negatively charged, residues on the segment affect the conductance of the channel. If the M2 segment is assumed to be an alpha helix then all of these residues appear on the same side. Although circumstantial, the evidence is convincing: it seems that the pore of the Ach receptor is formed by the M2 segments of each of the sub-units, in the form of five alpha helices in a bundle. If this interpretation is correct the negative charges form three rings around the pore: one at each end of the trans-membrane section and one just inside the membrane on the cytoplasmic side. Moreover, the point mutagenesis experiments suggest that these rings of charges are necessary for the channel to conduct.

In a recent breakthrough the detailed structure of the KcsA channel has been found by crystallographic methods [21]. This is a bacterial channel, but the protein sequence of its membrane spanning region is very similar to a group of voltage gated potassium channels (K_a channels) found in eukaryotes. The KcsA channel is formed from four identical sub-units, and is about 45 Å long in total. Unlike the ACh receptor it has no vestibules. The eukaryotic K_a channels have much larger sub-units, however, which may include vestibules. The shape of the pore is unexpected. It starts out relatively narrow (around 3 Å radius) on the cytoplasmic side, then expands into an ellipsoidal chamber (around 5 Å in radius and 12 Å long) near the centre of the membrane, which is connected to the extracellular side by a very narrow section (around 1.5 Å radius). The narrow section is lined with polar carbonyl groups. The chamber and lower pore, however, have hydrophobic walls. Short alpha helices within the surrounding protein provide large fixed dipole moments, with negative poles pointing towards the central chamber. There is also evidence of charged residues near the cytoplasmic

and extracellular entrances to the channel. Doyle et. al. [21] suggest that the narrow section is a selectivity filter, while the combination of the water filled chamber and helix dipoles act to stabilize cations in the hydrophobic centre of the membrane.

In summary, while knowledge about the structure of channels is limited, it is enough to begin constructing theories based on channel structure, rather than the fitting of abstract models to experimental data. The information available about the ACh channel, its overall shape and the position of some of the fixed charges, is sufficient to allow construction of a tentative model using Brownian dynamics simulations, as described in chapters 3 through 7. Sansom and co-workers have gone further [65], by using molecular dynamics to deduce a detailed structure for the ACh channel pore, based on the sequence of the M2 helix. The discovery of the crystallographic structure of the KcsA channel is a major advance. The structure revealed can be used as the basis for Brownian dynamics simulations, as described in chapter 8. It is detailed enough for molecular dynamics simulations, allowing investigations of the operation of the selectivity filter. It also raises the hope that more crystallographic structures of channels will be discovered, providing further encouragement for the development of structurally based theories of channel operation.

Chapter 2

Conductance Theories

The existing theories of ion channel conductance have had some success, but they do not provide a coherent picture, nor can they predict conductance from structure. The theories operate on different scales and under different assumptions. Each can explain some aspects of channel conductance, but there is no bridge between the theories, no way to know which aspects are dominant for a particular channel with a defined structure. Some theories propose contradictory mechanisms, for instance reaction rate theory involves a mechanism of kinetic hopping over a small number of energy barriers, while Brownian dynamics and Poisson-Nernst-Planck theory are based on the diffusion of ions. In other cases the links between the different theories have not yet been sufficiently explored. For example molecular dynamics studies can be used to investigate the molecular mechanisms of diffusion and electrostatics in channels, and so check and calibrate the assumptions Brownian Dynamics and Poisson-Nernst-Planck theory, but unambiguous results are yet to emerge from the attempts that have been made along these lines.

This project is an attempt to improve on this unsatisfactory situation: the biological importance of channels, the wealth of experimental data, and the emergence of detailed structures make the need for improved channel theories an acute one. However, the deficiency of progress in ion channel theory compared to that in ion channel experimentation is not due to a lack of effort or imagination on the part of theorists, but rather because of the difficulty of the problem. We therefore first examine the existing theories, identify their strengths and weaknesses, and then develop a new approach which attempts to combine as many strengths and as few weaknesses as possible, with the aim of predicting conductance from structure to allow comparison with experiment. This new approach is by no means perfect: our hope is to improve upon the existing theories, and that the new theory in turn will inspire still further improvements by ourselves or others.

This chapter gives a brief description of three of the most successful

theories of channels, explaining how they work, what aspects of channel behaviour they explain, what their strengths and weaknesses are, and why we believe they cannot predict conductance from structure. Reaction rate theory (RRT) is a simple theory of kinetic hopping between states, developed to explain the rate of chemical reactions, used successfully for enzymes, and later applied to channels [20]. It is popular because of its usability and its ability to explain the operation of multi-ion channels, but its physical assumptions, while appropriate for enzymes, are inappropriate for channels. Molecular dynamics (MD) is a simulation technique that operates fully on a molecular level, with all higher level phenomena emerging from the simulation [4]. It has been used to discover the conductance mechanism in the pores formed by the antibiotic gramicidin. It has the *potential* to predict channel operation from near first principles, but with existing computers it is too slow to predict the conductance of channels. Poisson-Nernst-Planck theory (PNP) is a new method: based on the continuum theories of electrostatics and diffusion it is simple enough to predict conductance using a desktop computer system [23]. It can fit experimental data over a larger range than RRT, but some of the structural and physical predictions it makes seem strange. We believe that one of the simplifying assumptions that makes PNP so usable is flawed, and this leads PNP to make some incorrect predictions.

The chapter goes on to describe our approach to the problem and why we chose it. These are the tactics to implement our strategy of the most comprehensive simulation still capable of predicting conductance. We choose to use three-dimensional Brownian dynamics (BD), a technique where the ions are simulated explicitly, but the water is treated as a continuum. Brownian dynamics has been used before to study channel conductance, but only in one dimension (the axis of the channel). Our approach is based on the concepts of diffusion and electrostatics (as is PNP), but the diffusion is simulated on an ion by ion basis. In three-dimensional BD both shielding by counterions (predicted by PNP), and multiple ion effects (predicted by RRT) should emerge naturally from the simulation. The treatment of water as a continuum and the channel wall as an abstract geometric shape are necessary simplifications to make the simulation fast enough. Even with these simplifications the electrostatic problem must be solved extremely quickly if conductance is to be predicted.

2.1 Reaction Rate Theory

Reaction rate theory is a highly simplified model. The channel is represented as a series of energy wells, or binding sites, separated by energy barriers. The ions are assumed to linger in the wells, moving by rapid hops over the energy barriers. So the channel has states, each consisting of a pattern of

particular types of ions in particular wells (each well is assumed to hold at most one ion). Conductance can be calculated from the transition probabilities between states, or equivalently the reaction rates between states (if the movement of an ion from one energy well to another is thought of as a chemical reaction). For a single ion channel with only one type of permeant ion there is one state per energy well (plus the state for the unoccupied channel), and the reaction rates are simply the probability of the ion moving forwards or backwards when it is in a particular well. These probabilities are affected by the strength of the applied electric field. Multi-ion channels, and channels with more than one type of permeant ion, have more complicated state diagrams, and there are multiple transition probabilities associated with each well, depending not only on the type of ion that occupies that well, but on the occupancy of other wells (that is the state of the whole channel). This abstract model of states and transition probabilities represents all of the interactions between the ions, water, and protein wall.

Reaction rate theory was invented to explain and predict the rates of chemical reactions [25, 7]. The theory is based on the concepts of a reaction pathway and an activated complex. The reaction pathway is a series of configurations that the reactants must pass through to become the products. The activated complex is an unstable combination of the reactants, ready to break into products. Eyring's original formulation of the theory [25] uses statistical mechanics to estimate the proportion of reactants in the form of the activated complex, and then estimates the rate of decay into products from the frequency of vibration of the activated complex. The rate of the reaction is then the product of these two quantities. The use of statistical mechanics relies on the states involved being in near equilibrium, but this is a reasonable assumption for chemical reactions, which typically have large energy barriers and are slow compared to thermal motion. This form of RRT allows reaction rates to be predicted from knowledge of the structure of the reactants and the activated complex, and the potential energy step between them. Unfortunately the structure of the activated complex is often unknown, so there is an alternate form of the theory based on thermodynamics rather than statistical mechanics. This is more of an explanatory tool, allowing the rate of a chemical reaction to be interpreted as a free energy barrier. If the temperature dependence of the reaction rate is also known, the free energy can be split into enthalpy and entropy, with the enthalpy corresponding to the potential energy in the original formulation.

RRT has a history of successful use in chemistry, including biochemistry, where it is used to explain the operation of enzymes. Enzymes are proteins which speed up (often greatly) chemical reactions which could happen spontaneously. They operate by binding tightly to a substrate, and by stabilizing the transition state: reducing the energy cost of the substrate entering a form part way between two stable forms [51]. RRT thus provides an intuitive explanation for the operation of enzymes: with the energy step to

the activated complex reduced, the proportion of reactants in the activated form is greater, and the reaction proceeds more quickly. RRT also provides a framework for the quantitative prediction of reaction rates in enzymes, as the situation in enzymes is close to the original assumptions of tight binding, a single reaction path, and chemical bonds being broken and formed at the transition state. RRT can also be used to describe diffusion [26, 31] by assuming a series of small energy wells which an ion hops between, performing a random walk. If the wells are closely enough spaced RRT predicts a linear relationship between applied field and drift velocity, agreeing with experiment and conventional diffusion theory. This form of RRT has been used successfully to study diffusion in solids, for example to predict deviations from ohms law in glass at large fields [49]. This does not necessarily mean that the diffusion and hopping models are equivalent, however. As pointed out by Jordan [39], diffusion is a poor model if there are sharp changes in energy along the reaction pathway (within a fraction of an ionic radius), while hopping is a poor model if the energy is slowly varying over a large distance (several ionic radii).

The physical assumptions of reaction rate theory are unlikely to be met in channels [20]. The high rate of ion transport in ion channels suggests that diffusion is the main mechanism of transport. Diffusion involves broad, shallow energy wells, a multiplicity of possible paths, and no special activated state where the key step in an ion's transport can be said to happen. These are very different conditions to those which gave rise to RRT. While RRT can be used to describe diffusion, this use demands a series of small energy wells, a few ionic radii across at most, and in any case works best for crystals and solids where the location of the wells is fixed. Analysis of this sort may be useful in the narrowest regions of a channel, where protein is substituting for some of the first hydration shell. In the gramicidin channel, which is very narrow throughout, RRT of this type has been used to relate structure to conductance. However, a more typical use of RRT involves dividing the entire length of the channel (typically 25-80 Å) into at most half a dozen energy wells or binding sites. This is nowhere near enough wells to describe diffusion across the length of the channel by RRT. The wells are sometimes interpreted as describing the situation in the selectivity filter, with the rest of the channel (where the physical basis of RRT is hard to justify) assumed to be unimportant to conductance [31]. In a multi-ion channel this amounts to an assumption that all the ions crowd together in the selectivity filter, within a few angstroms of each other. Even under this assumption, the meaning of the free energy barrier produced by RRT is unclear. Without studies of the temperature dependence of conductance (which are rarely done) the free energy cannot be split into enthalpy and entropy. Moreover, the pre-exponential factor used to estimate the free energy barrier in RRT, derived under the assumption of a chemical reaction taking place, may not be appropriate for describing the transport of ions

in channels [39]. If so this means that the heights of the barriers estimated by the theory are meaningful only in the most abstract sense, and are not useful for comparison with channel structure.

Thus the physical assumptions of RRT are probably violated in channels: nevertheless it continues to be used, because it is simple, provides intuitive explanations for the operation of multi-ion channels, and works reasonably well [20]. In practice, RRT is used by developing an abstract model of states and transition probabilities, and fitting this to the experimental data. After this is done the abstract model is translated into energy wells and barriers using the modified Boltzmann factors of Eyring rate theory. Although the state diagram for a multi-ion channel is complex, it can easily be solved by a desktop computer, making RRT usable in any laboratory. RRT has been successful in explaining many of the peculiar behaviors of multi-ion channels, and does so in an intuitively understandable manner. The RRT parameters fitted for a set of experimental data can predict the conductance of the channel under similar conditions, but very different conditions require a new fit and different parameters [23]. Most practitioners of RRT are aware of its limitations, and do not make claims for great quantitative accuracy or ability to predict structure. Rather they continue to use it because of its many advantages, and because no more realistic theory can do the same job.

The success of RRT indicates not that its physical assumptions are somehow valid, but that the abstract model of states and transition probabilities is a reasonable, if not perfect, match to the mechanisms of channel conductance. It is the abstract model that is fitted to the experimental data, and provides the intuitive explanations. There is no reason to expect that the barrier and well heights predicted by the Eyring rate theory interpretation of the model have any relation to the real forces experienced by an ion traveling through a channel. Other mechanisms can explain the existence of states and transition probabilities: they could be caused by diffusion between broad energy wells, rather than kinetic hopping. This is suggested by our Brownian dynamics results: see chapter 8.

As RRT is generally applied to channels, the quantitative predictions it makes about energy profiles cannot be trusted, and it cannot be used to predict channel conductance form channel structure. This is because the physical assumptions of RRT are inappropriate for channels. Although RRT can make accurate predictions when carefully applied to very narrow channels such as gramicidin, and this approach could be extended to the narrow selectivity filters of other types of channel, this is not how RRT is usually used. Rather it is applied to a small number of energy wells spread over the full length of the channel. Even if the number and depth of such free energy wells were somehow calculated from a channel's structure, Eyring rate theory would not accurately predict conductance in the wider regions of the channel, because the assumption of transition between states by a

single kinetic jump would not apply. Nevertheless the success of RRT, or rather the abstract state models it leads to, cannot be ignored. An improved model of channel conductance should include the parts of RRT that work, by allowing the channel to take up distinct states, and accurately calculating the interactions between ions in these states.

2.2 Molecular Dynamics

Molecular dynamics is a detailed simulation technique, based solely on intermolecular interactions [4, 40]. It works by dividing simulated time into very small steps (typically one or two femtoseconds), calculating the force on each atom at each step, and then moving all the atoms a short distance according to the laws of mechanics. This algorithm assumes that the force on each atom is constant during each timestep: keeping this assumption approximately true is the reason for the very short timesteps. Constraints on the atoms can be incorporated into this scheme, and are often used to represent rigid molecular bonds. Less rigid bonds are represented by a combination of constraints and forces. Each atom interacts pairwise with every other atom, and large scale effects, such as diffusion and induced charges, emerge from this multitude of interactions. The computer keeps track of the position of each atom at every time step, but making sense of this vast amount of information requires either analysis in terms of higher level concepts and theories, or graphical visualization.

The model forces between atoms are determined empirically, by fitting parameters to make the simulations match experimental quantities such as radial distribution functions and diffusion constants [11, 9, 29]. Because these experiments (and the simulations they are used to calibrate) are done for bulk materials, it is possible that model forces may not be correct in the environment within a channel. For example, non-polarizable water models have a larger dipole moment than isolated water molecules (water vapor) to account for the average polarization that occurs in liquid water. This average polarization may not be correct in the first hydration shell of an ion, or in a highly charged part of a channel. Short range forces between atoms are modeled by a Lennard-Jones function, or a similar form, which includes Van der Waals attraction and soft sphere repulsion. Longer range forces are modeled by partial charges on the atoms and are calculated using Coulombs law.

MD studies of a channel are much easier and more reliable if the detailed atomic scale structure is available. If it is, it provides the boundary between water and protein, and any effects depending on the details of interactions between ion, water, and protein will be faithfully reproduced. For instance, an MD simulation based on a real channel structure should be able to predict that channel's selectivity between ions of the same valence. Empirical

constraints would still be needed to hold the channel protein in position: in reality this is done by the membrane, but MD simulations must be kept as small as possible to reduce the computational cost. There would also be a need for reservoirs of water at either end of the channel, and these would have to be provided with some sort of boundary. However, both the boundaries for the reservoirs and the constraints holding the protein would be a fair distance from the critical part of the simulation, namely the channel pore. Boundaries are always a difficult part of an MD simulation, since the simulated volume is small, and effects from an improvised boundary can easily propagate into the centre of the simulation and affect the results. This presents a problem if the detailed structure is *not* available. It is possible to use an abstract geometric boundary, as we do in our BD simulations, but in an MD simulation the atomic level detail of the boundary makes a difference, be it an imaginary hard wall, an array of carbon atoms, or some other scheme. With the results of the simulation perhaps depending on an arbitrary choice of boundary lining, the extra effort of a simulation on the atomic level hardly seems worthwhile. For this reason MD simulations of channels are usually only done for a detailed structure.

At least one detailed structure for a channel is now available, and more may become available in the future, but there is another problem with the use of MD as a theory of channel operation: with existing computers it is too slow to predict channel conductance. The timesteps are very short, and each step requires calculation of all the pairwise interactions between atoms, at a large computational cost which increases with the square of the number of atoms. A typical run of one million steps only yields a nanosecond or two of simulated time. Several microseconds are needed to estimate conductance. For short range forces not all of the pairwise interactions need to be considered: these forces have little effect at distances of more than a few Angstroms, and a cut-off at 6 to 10 Å can be imposed. This reduces the number of interactions, but logic to impose the cut-off must be included in the algorithm, and this may slow the program, especially on a vector processor. Nevertheless, cut-offs are often used, especially for larger systems where their advantage is greatest. Unfortunately, the long range (Coulomb) forces from the partial charge centres cannot be cut off in a channel simulation, as electrostatic effects such as induced charges and shielding are caused by the partial alignment of water dipoles throughout the simulation. Any attempt to cut-off the long range forces would likely prevent these important electrostatic effects from emerging from the simulation, so channel simulations are stuck with calculating all pairwise interactions between partial charge centres.

As an example take a system of 1000 partial charge centres: a small channel and 150 water molecules. This requires 500,000 force calculations per timestep. If each takes 100 floating point operations, and the program achieves 1 gigaflop, each step will take 0.05 seconds. A gigaflop is 10^9 floating

point operations per second, but MD programs typically achieve only 1/3 of the rated maximum speed of a computer. Only supercomputers are this fast at the moment, though no doubt desktop systems will follow shortly. At 20 steps per second, 1,000,000 steps will take 14 hours of CPU time and yield 1 ns of simulated time. To see an ion cross the channel will take a minimum of 10 ns, or a week of CPU time. To measure conductance will take at least 1 μs, or about $1\frac{1}{2}$ years of CPU time. And this is just for one point on one I/V diagram.

The elegance, comprehensiveness, and physical realism of MD make it a very attractive technique, and agree with the strategy of making the minimum number of assumptions, unfortunately its inability to predict conductance prevents direct comparison with experiment, and rules it out as a possible method for this project. This is not a fundamental weakness, however, only a limitation of current computer hardware. If computers continue to increase in speed, estimation of channel conductance by MD will become practical in the future (based on a doubling of computer power every 18 months, I predict 2010 for supercomputers, and 2015 for desktop systems). In the meantime there are plenty of interesting uses for MD, including investigation of the assumptions underlying the continuum theories of channel conductance, PNP and BD.

2.3 Ab Initio Molecular Dynamics

The new ab initio molecular dynamics technique provides a way of removing the doubt about interatomic forces, at the cost of even more computer time than conventional MD [13, 62]. It has not yet been applied to ion channels, but it may be in the future. Car and Parrinello's innovative algorithm combines classical MD with the density functional theory of quantum chemistry. The paths of the atoms are still simulated by classical mechanics, but the forces between atoms are calculated from first principles using density functional theory. Calculation of these forces requires the ground state of the electronic structure to be found, which is a multi-dimensional optimization problem with constraints (the basis functions must be orthonormal). In ab initio MD this optimization problem is solved by simulated annealing, a technique where a multi-dimensional space is explored to locate a global minimum (or near minimum) by some form of pseudo-mechanics. Instead of the usual Monte Carlo algorithm, Car and Parrinello use classical MD as the pseudo-mechanics, with the orthonormality constraints maintained by the SHAKE algorithm (the usual constraint algorithm for classical MD). Thus the same algorithms are being used both to simulate the classical motion of the atomic centres and to calculate the quantum states of the electronic structure. With a small enough timestep the two halves of the calculation can be combined and proceed simultaneously. In practice this technique

works very well, with the pseudo-momentum of the electrons (from the simulated annealing algorithm) tending to keep the electronic state optimized as the atoms move, eliminating the need to re-optimize after every timestep, and greatly speeding up the simulation. Systems of moderate size have been run for picoseconds of simulated time: 128 silicon atoms in a crystal for 6 ps [12], and a beryllium ion hydrated by 31 water molecules for 1 ps [48].

Assessment of the speed of ab initio MD calculations is difficult, as the technique is more complex than classical MD, the methods are still developing rapidly, and the computers used and CPU time taken are rarely reported. Timesteps are typically 1-2 $\times 10^{-16}$ s, around 10 times smaller than for classical MD. The time taken to perform a step depends greatly on the basis functions chosen, which depend on the particular atoms being simulated. Overall, ab initio MD seems to be around three orders of magnitude slower than classical MD, which is consistent with the reported picoseconds of simulated time, rather than the nanoseconds typical for classical MD. As computers become faster, and classical MD is used for larger systems and longer timescales, it is likely that ab initio MD will be used for the sorts of problem currently being tackled using classical MD. It might not be necessary to wait for faster computers, however: it is possible that improved algorithms and better basis functions will provide the speed needed for ab initio MD to be more generally useful. As an example, for certain sorts of basis functions the pseudo-forces can be calculated by fast Fourier transform methods [62]: this reduces the dependence of CPU time on system size from n^2 to $n \log n$ (where n is the size of the system), making the simulation of large systems much more practical. Ab initio MD is a technique worth watching.

2.4 Poisson-Nernst-Planck Theory

PNP is a simplified model of channel conductance which, unlike RRT, is based on physical mechanisms that are likely to apply in channels [23, 24, 14, 15, 16, 54, 53, 41]. It treats both water and ions as continua, describing them by the the Nernst-Planck equation of electrodiffusion theory, and Poisson's equation of macroscopic electrostatics. These simplifications allow a PNP model to be solved quickly on a desktop computer system: in practice many PNP models are solved together as physical and structural parameters are automatically adjusted to fit a set of experimental data. When used in this way PNP can deal with a greater range of experimental conditions than RRT, but it does not offer the same intuitive explanations of the conductance mechanism. In effect PNP is used to make predictions about the structure of the channel (the position and density of charges on the channel wall) and the physical conditions inside it (the diffusion coefficients of the ions). If the shape of a channel, the position of fixed charges, and the diffusion coefficients

were known, then PNP could be used instead to make predictions about a channel's conductance from its structure.

Poisson's equation describes the electric potential in relation to the charge density and dielectric constant. It can be solved to estimate the long range forces on ions in a channel model where water is treated as a continuum. Water and protein are treated as continuous dielectric media, with different dielectric constants. The many atomic and molecular dipoles contained in the water and protein are approximated as a linear polarizableity of the media: in effect this is an assumption of evenly spread, infinitesimal dipoles. This assumption is entirely reasonable at macroscopic scales, but on the scale of ion channels the individual water dipoles that produce most of the dielectric effects are far from infinitesimal. Nevertheless, treating water as a continuum is the key assumption necessary to simulate channel conductance in a reasonable time, and is made by both BD and PNP. The approximate and macroscopic nature of this use of Poisson's equation is due to the concepts of dielectrics and dielectric constants [28]. Without these Poisson's equation is an exact representation of electrostatic forces, and can be used at an atomic level, for instance in the interatomic force calculations of ab initio MD.

In channel models the water-protein interface is represented as a dielectric boundary, and the solution of Poisson's equation depends on the shape of this boundary. Analytical solutions can be found only for particular shapes: PNP is generally used with a solution for a finite cylinder, and in chapter 4 I describe our analytical solution for a torus. If other shapes are needed (and the shape of the pore may well be a factor in channel conductance) then a numerical method of solution must be used. I describe our numerical method in chapter 3, and our method of making it fast in chapter 6. There is no reason in principle why numerical methods cannot be used with PNP: although they are usually much slower than analytical methods, this is more of a problem for BD simulations. The qualitative effects of the dielectrics on an ion are twofold. The high dielectric strength water reduces the effective field of the ion by a large factor as nearby dipoles orient themselves to provide a layer of negative charge around a cation, or positive charge around an anion. Dipoles further out are also oriented, but where the field from the ion crosses a boundary into the much less polarizable protein the layer of dipoles at the boundary creates an induced surface charge of the same polarity as the ion. This induced charge has the effect of repelling the ion from the boundary. This is the same phenomena as repulsion due to the energy cost of removing the hydration shells of the ion, looked at from a different point of view, that of a macroscopic theory. Although the qualitative effects of dielectrics are easy enough to understand, quantitative calculations are highly dependent on the shape of the boundary, as induced charge generates its own field and induces still further charge. Solving Poisson's equation produces a self-consistent set of surface charges, but the calculations are very

complex.

The Nernst-Planck equation describes electrodiffusion: it gives the current in terms of ion concentration and electric potential. By assuming a constant current (which there will be during steady state conductance) it is possible to solve the Nernst-Planck equation to give the concentration profile in terms of the potential profile, or vice-versa [31]. However, in a real channel both of these change to arrive at the steady state. In PNP theory it is assumed that the potential profile can be obtained by solving Poisson's equation for the charge distribution of the average concentration profile [23]. This is the mean field assumption, so called because the superposition principle applies to solutions for different charge distributions (provided they are for the same dielectric boundary), and as a result the mean concentration profile yields the mean field. This assumption allows the Nernst-Planck equation and Poisson's equation to be solved simultaneously by a process of iteration, giving a prediction of potential, concentration, and current for the model channel.

While PNP does a good job of fitting experimental conductance data, some of the predictions it makes in doing so seem strange. PNP predicts diffusion constants an order of magnitude lower than the bulk values for cations, and two orders of magnitude lower than bulk values for anions. The confined space of a channel pore may well reduce the mobility of ions (molecular dynamics studies are needed to confirm this), but a factor of 10 or 100 seems excessive, and the large difference between cation and anion mobility has not been explained. Also, PNP predicts that the electrostatic barrier presented to ions by the membrane is completely removed by shielding by counterions. PNP is designed to be electrostatically self-consistent, and the electrostatic effects of the membrane and the channel protein are included in the model, and do indeed present a barrier to individual ions. This barrier can be turned off without affecting the results of the simulation, however. As long as concentrations of cations and anions are approximately equal the negative charges induced by the cations and the positive charges induced by the anions cancel out, and produce no net repulsive force. Since biological membranes prevent ions from crossing by means of an electrostatic barrier, and a channel's main purpose is to allow ions to cross, the complete insensitivity of PNP to barriers of this type is very worrying.

On the small scale of channels the Nernst-Planck equation has to be interpreted in an unusual way: while it remains valid under this interpretation, the same may not be true of the mean field assumption. In the confined space of a channel pore the concentrations appearing in the Nernst-Planck equation must be interpreted as probability densities. For example a section of pore 3 Å in radius and 6 Å long has a volume of 170 cubic Å, and contains 0.015 ions at a typical physiological concentration of 150 mM: in other words there is a 1.5% chance of the section containing an ion. The Nernst-Planck equation links two different causes of average ion motion, of drift superim-

posed on random diffusion. The first is average motion due to concentration differences. This is a statistical effect that places no real force on any ion. Rather, if there are more ions on one side of an imaginary line, random motion will tend to even them out, creating a net drift. This source of motion is unaffected by the probability density interpretation: a greater probability of an ion being on one side of the line leads to a greater probability that an ion will cross from that side to the other. The second cause of motion is the average drift velocity due to the electric field acting on the ions. This is a real force acting on real ions, not a statistical effect. It produces an average drift velocity rather than straight line motion due to the water molecules which surround the ions: these produce both friction and a superimposed random motion. The drift velocity is proportional to the applied force, and takes around a picosecond to build up. Again, this source of motion makes sense under the probability density interpretation, *provided* that the electric field experienced by each ion is calculated correctly.

This is where the mean field assumption falls down: it is likely that some of the predictions of PNP are incorrect, and that the mean field assumption is responsible. The mean field is averaged over a period of microseconds, the timescale of the steady state current, while changes in the electric field and resulting ion motion occur on a timescale of picoseconds as individual ions move through the channel. To give a concrete example, consider again the small section of pore, 3 Å in radius and 6 Å long, and imagine that it is near one end of the channel. If the section contains a cation (a 1.5% chance) then positive charges are induced on the walls of the pore, and these repel the ion, tending to expel it. If instead the section contains an anion (again a 1.5% chance) then negative charges are induced, but the force is still repulsive, since the anion is also negatively charged. From the microscopic point of view either polarity of ion is progressively having its hydration shells stripped off as it moves into the channel, and this increasing energy cost produces a repulsive force. Finally, if there is no ion present in the section (a 97% chance), then the electric field in the section has no relevance to ion conductance, as it cannot produce a drift velocity without an ion to act on. The electric field in the section is very different in these three cases, and changes on a picosecond time scale as ions move in and out. Under the mean field assumption, however, the electric field from all of the cases is averaged, weighted by their probabilities: 1.5% chance of a field repelling cations, 1.5% chance of a field repelling anions, and 97% chance of a field produced by distant ions that has no relevance to the drift velocity in this section. It is no surprise that this average field is very close to zero, and as a result PNP predicts that charges induced on the boundary by the ions have no effect on conductance. Presumably if a PNP simulation of a biological membrane was set up, with appropriate calculation of the electrostatic barrier, and values for ion mobility in lipids used for the interior, then the mean fields from cations and anions would cancel out, and PNP would predict a large ion

flow through the membrane.

The error in applying the mean field assumption to channels is a statistical one: the states of the system are being weighted by total probability, when conditional probabilities are required. Because the electric mobility term of the Nernst-Planck equation is based on drift velocity, it carries an implicit assumption that there is at least one ion at the position of interest. In a macroscopic system this is not a problem (at 150mM a drop of water contains around 10^{20} ions). On the microscopic scale of solid state electronics this assumption is still valid, and approaches similar to PNP have been successful in modeling transistors. However, on the atomic scale of a channel the chance of a small section of pore containing an ion are quite low. To be consistent with the Nernst-Planck equation, the mean field must be calculated *given* that there is an ion at the position of interest: the possible states of the channel must be weighted by their conditional probability under this assumption to arrive at the average field. This approach would calculate different electric fields for cations and anions approaching the membrane, and so predict that both would be repelled. Unfortunately the concentrations yielded by solving the Nernst-Planck equation give no indication of what these conditional probabilities are, so the problem with using the mean field cannot easily be corrected.

2.5 Brownian Dynamics

Brownian dynamics is a simulation technique that treats ions explicitly, moving them step by step in the same manner as an MD algorithm, but treats water as a continuum, as PNP does [4]. BD is based on the Langevin equation, which breaks up the forces on an ion into three components: random force, frictional force, and systematic force. The random and frictional forces represent the effect of the ion colliding with the surrounding water molecules. The distribution of the random force is a three dimensional Gaussian, while the frictional force opposes the direction of motion of the ion, and is proportional to its velocity. The magnitude of both depend on a frictional coefficient which is derived from the diffusion coefficient for the ion in water. The systematic force is the sum of forces not caused by the surrounding water. In the case of an ion this is mainly the electrostatic force due to the other ions and the water and protein throughout the system. This force can be calculated by solving Poisson's equation for each step, many more times than it needs to be solved for PNP.

BD can be done on two different timescales [35, 72]. In the diffusive regime each step is around 100 fs long and represents a small amount of diffusion for each of the ions. Over this long timestep the Langevin equation has to be integrated, and produces a random motion of each ion, not correlated with its previous velocity. The systematic force produces a drift

velocity. In the kinetic regime each step is 1 or 2 fs long and represents thermal motion by the ion, including contributions from collisions (the random and frictional forces), and from the systematic force. The ion's velocity in each step is highly correlated with that in the last step. The Langevin equation is integrated by the repeated action of the motion algorithm, in the same way that an MD algorithm integrates Newton's equations. The advantage of using the long timestep is speed of simulation: simulated time passes 100 times faster, ions move a significant distance in each step (an rms displacement of 0.34 Å for a potassium ion in a 100 fs step), and prediction of conductance becomes a possibility. The advantage of the short timestep is accurate integration of motion near sharp energy barriers, such as the repulsive forces that act between atoms at close ranges. In a timestep of 1 fs a potassium ion moves an average of 0.004 Å, and can respond to a sharp repulsive force, as velocity is built up over several steps. In the diffusive regime the systematic force only has an indirect effect by producing a drift velocity that will bias the motion over many steps, but the ion can pass over a sharp barrier (1 or 2 Å in width) in only a few steps, before the repulsive force has time to act. This is the penalty for viewing ion motion on the longer timescale: small scale forces cannot be accurately represented. In our simulations we use the long timestep most of the time, representing ions as hard spheres and the protein boundary as a hard surface to avoid the problem with repulsive forces. In some simulations we define short timestep regions in critical parts of the channel, and use the appropriate number of short timesteps instead of a long timestep for ions in these regions. This allows us to use more accurate forces where we need them without sacrificing the overall speed of the simulation.

Brownian dynamics makes prediction of conductance possible: it is much faster than MD while making fewer assumptions than either PNP or RRT. The change from thousands of charge centres in MD to a few dozen ions in BD greatly reduces the number of interactions that have to be considered at each step, since the number of interactions is proportional to the square of the number of charge centres. In addition it is possible to use a much larger timestep for BD, one of 100 fs instead of the 1 or 2 fs typical of MD. Despite these advantages a simulation which predicts conductance requires very many steps: 10 million for a simulated time of 1 μs. Poisson's equation needs to be solved for each of these steps, many more times than it needs to be solved in a PNP simulation. The key to using BD to simulate a channel is solving Poisson's equation quickly. Previous simulations of channels using BD have been done in one dimension (to make the solution of Poisson's equation simple) and with only a few ions, but this assumes that there is no shielding of the electrostatic forces by counterions, an assumption that should not be made given the results from PNP. While we think that this shielding is an artefact of the mean field assumption of PNP, we should test this hypothesis, not assume it. Our simulations are done in three dimen-

sions, with reservoirs of ions and counterions available for any shielding, which should emerge naturally from the motion of the ions under the BD algorithm. Another advantage of BD is that it allows the multi-ion channel states suggested by RRT. While RRT is based on non-physical assumptions (for channels) its success in explaining the operation of multi-ion channels suggests that its abstract model of states and transition probabilities may have a basis in reality. While PNP averages the concentration profile of the channel over many individual ion passages, BD simulates each individual passage, and so samples the state space of the channel, and includes any multi-ion effects.

The limitations of BD come from the assumptions it makes: that water and protein can be treated as a continuum. This means that selectivity between ions of the same valence cannot be expected to emerge from the simulation, since this must be dependent on the detailed interactions between an ion, its first hydration shell, and the channel's selectivity filter. The macroscopic electrostatics used to estimate the long range effects of the water and protein cannot be entirely accurate in the confined space of a channel pore. The success of the Born energy approximation for the hydration energy of ions indicates that macroscopic electrostatics can be useful at these small scales, but the errors due to using it inside a channel have not been quantified. Other sources of uncertainty are the diffusion coefficient and dielectric constant. While these are known for bulk conditions they may have different values inside a channel. In particular the use of the same dielectric constant for water throughout the simulation is a simplification that may not be appropriate for channels. See section 3.1.4 in the following chapter. Molecular dynamics has the potential to resolve these questions and so put BD simulations on firmer foundations. MD could also be used to investigate selectivity in channels where the detailed structure is known.

Despite these uncertainties, BD is the technique that best meets our strategy. PNP and RRT make too many simplifications, while MD is too slow to predict conductance. Although these theories are inadequate for our purpose, they give clues to what is important, suggesting what cannot be simplified. RRT tells us that states formed of a few ions may be important, requiring explicit simulations of the ions. PNP tells us that shielding by counterions should be allowed, requiring simulation in three dimensions. We accept the abstraction of water and protein as necessary to enable conductance to be predicted, in the knowledge that MD simulations have the potential to investigate the effects of this simplification. Having decided on a technique, the problem is to get it to work: the major challenge here is to solve Poisson's equation rapidly for a channel shaped boundary. The description of how this problem was solved begins in the next chapter.

Chapter 3

Iterative Method

The decision to use Brownian dynamics creates the need to calculate the electric field and potential inside a channel without explicitly considering the water molecules. Water molecules have permanent dipole moments. Within the structure of liquid water they have some freedom to rotate, and align themselves with an applied electric field. The combined effects of all the water dipoles are a major component of the force acting on an ion within a channel, and must be included in any realistic simulation. We need a way of summarizing and accurately predicting these effects. The macroscopic theory of electrostatics provides the answer. This theory represents substances as regions of constant polarizability and uses a three dimensional differential equation, Poisson's equation, along with boundary conditions where the polarizability changes, to describe the electric potential [28]. The parts of this theory relevant to our simulations are summarized in section 3.1 below.

There are two ways to solve such a system of differential equation and boundary conditions. The traditional way, and the only practical way before the invention of computers, is to produce a solution by mathematical analysis of the problem [52]. Such a solution for a toroidal boundary is described in chapter 4. The power of modern computers provides a second approach. Differential equations describe relationships between the rate of change of various quantities, and can be solved by imposing these relationships on a system and iterating: repeatedly recalculating the state of the system until a solution is reached. This approach has been used to analyze the electrostatic barriers in the gramicidin channel [56, 43, 44, 36, 37, 38], and the work described here continues this tradition, using the improved performance of a vector supercomputer to calculate solutions for larger channels with more complicated shapes.

The first step in constructing such a numerical algorithm is to divide the problem into finite pieces. Poisson's equation describes the electric potential in three dimensions, and can be solved by discretizing space, dividing it into a Cartesian grid, for example. In the case of an ion channel, however, the

boundary is the interesting part of the system, and as shown below, it is sufficient to find the surface charge on the boundary. So we discretize the channel boundary, dividing it into sectors which tile the surface. The advantage of this approach is that the boundary is represented more accurately, since the sectors are defined to follow the surface, rather than the surface being approximated in a Cartesian grid. The disadvantage is an inability to represent variations in dielectric constant away from the channel boundary: see section 3.1.4 for a description of why this would be useful.

There are three stages to our iterative solution. The first stage is to generate a geometric outline of the channel, which can be rotated to form the three-dimensional boundary. This is described in section 3.2. The second stage is to divide the boundary into sectors. To make the algorithm practical the sectors have to be concentrated in the constricted regions of the channel, so the sector spacing has to vary. This is described in section 3.3. The third stage is the iterative algorithm itself. This is the stage that takes up all the computer time. It is described in section 3.4. Section 3.5 describes a method of increasing the accuracy of the algorithm by compensating for the curvature of the sectors. Section 3.6 describes the testing of the iterative solution and discusses its performance.

3.1 Macroscopic Theory of Electrostatics

3.1.1 Poisson's Equation

Poisson's equation is the fundamental equation of electrostatics. It relates the electric potential φ throughout space to the charge distribution ρ:

$$\nabla^2\varphi = \frac{-\rho}{\epsilon_0}. \tag{3.1}$$

The electric potential is defined by its relationship to the electric field

$$\mathbf{E} = -\nabla\varphi. \tag{3.2}$$

The existence of the scalar potential φ is guaranteed by one of Maxwell's equations for electrostatics

$$\nabla \times \mathbf{E} = 0 \tag{3.3}$$

(it is a theorem of vector calculus that any vector field with a curl of zero is a gradient of a scalar field [28]). Poisson's equation can be obtained by substituting the definition of φ into another of Maxwell's equations

$$\nabla \cdot \mathbf{E} = \frac{\rho}{\epsilon_0}. \tag{3.4}$$

Solving Poisson's equation gives the electric potential throughout space, and the gradient of this potential is the electric field.

This is fine as long as the positions of all charges are known, but in macroscopic electrostatics this is not the case. The charges we know about are surrounded by insulators (or dielectrics) made up of many atoms, and these atoms have charges in them that may move in response to an electric field. In our case the main concern is with the water molecules, not simulated explicitly, each of which has a permanent dipole and is capable of rotating to align with the electric field. To take account of these non-explicit charges and incorporate them into the electrostatic theory we make two assumptions. The first is that a dielectric polarizes linearly in response to an electric field

$$\mathbf{P} = (\epsilon - 1)\epsilon_0 \mathbf{E}, \tag{3.5}$$

where $\mathbf{P}$ is the polarization, the dipole moment per unit volume, and ϵ is the dielectric constant. The dielectric constant is defined so that $\epsilon = 1$ for vacuum, hence the -1 in the equation: vacuum does not polarize.

This polarization implies a surface charge density on the surface of a dielectric

$$\sigma_{\text{pol}} = \mathbf{P} \cdot \hat{\mathbf{n}}, \tag{3.6}$$

(where $\hat{\mathbf{n}}$ is the normal pointing outwards from the dielectric), as well as a volume charge density within the dielectric

$$\rho_{\text{pol}} = -\nabla \cdot \mathbf{P}. \tag{3.7}$$

Substituting the volume charge density into Eq. 3.4 gives

$$\begin{aligned} \nabla \cdot \mathbf{E} &= \frac{\rho_{\text{exp}} + \rho_{\text{pol}}}{\epsilon_0} && (3.8)\\ &= \frac{\rho_{\text{exp}} - \nabla \cdot \mathbf{P}}{\epsilon_0} && (3.9)\\ &= \frac{\rho_{\text{exp}}}{\epsilon_0} - \nabla \cdot [(\epsilon - 1)\mathbf{E}], && (3.10) \end{aligned}$$

where ρ_{exp} is the explicit charge density, and the last line comes from the assumption of linear polarization (Eq. 3.5). This result can be summarized as

$$\nabla \cdot (\epsilon \mathbf{E}) = \frac{\rho_{\text{exp}}}{\epsilon_0}. \tag{3.11}$$

We now make a second assumption: that space is divided into regions where ϵ is constant. This means that

$$\nabla \cdot \mathbf{E} = \frac{\rho_{\text{exp}}}{\epsilon \epsilon_0}, \tag{3.12}$$

and so

$$\nabla^2 \varphi_i = \frac{-\rho_i}{\epsilon_i \epsilon_0}, \tag{3.13}$$

where i indexes the regions, and ρ_i is the explicit charge in region i. This is a simple modification to Poisson's equation, and can be solved using the

same methods. However, the assumptions mean that this is no longer a fundamental equation, but rather a macroscopic approximation. Examining the equation shows two things. First, the potential from charges is reduced by a factor of $1/\epsilon$. Second, the potential is otherwise unaffected: Laplace's equation $\nabla^2\varphi = 0$ still holds where there are no explicit charges.

This modified Poisson's equation describes what happens within a region of uniform dielectric constant, but not what happens at the boundaries between regions. To find the electric potential throughout space in a system with regions of different polarizability we need to know how the potential changes at the boundaries, or equivalently what the surface charge density is at the boundaries. Consider a small segment of boundary. Polarization creates a surface charge density

$$\sigma = (\epsilon_2 - 1)\epsilon_0 \mathbf{E}_2 \cdot \hat{\mathbf{n}} - (\epsilon_1 - 1)\epsilon_0 \mathbf{E}_1 \cdot \hat{\mathbf{n}}, \tag{3.14}$$

which is the sum of σ_{pol} from the two regions (see Eq. 3.6). $\mathbf{E}_1$ and ϵ_1 are the electric field and dielectric constant in region 1, $\mathbf{E}_2$ and ϵ_2 those in region 2. The normal to the surface $\hat{\mathbf{n}}$ points out from region 2 into region 1, hence the negative sign for the surface charge contribution from region 1. By convention we use region 1 (and ϵ_1) for water and region 2 (and ϵ_2) for protein, so the normal points outward form the protein boundary, into the water.

This is all very well, but $\mathbf{E}_1$ and $\mathbf{E}_2$, the electric fields on either side of the boundary, are affected by the surface charge density σ. We can introduce a new component of the electric field: $\mathbf{E}_{\text{ex}}$, the external electric field from charges outside the segment. By defining a Gaussian pillbox around our segment, and by assuming that it is sufficiently small, it is possible to show that

$$\begin{aligned} \mathbf{E}_1 &= \mathbf{E}_{\text{ex}} + \frac{\sigma}{2\epsilon_0}\hat{\mathbf{n}} \\ \mathbf{E}_2 &= \mathbf{E}_{\text{ex}} - \frac{\sigma}{2\epsilon_0}\hat{\mathbf{n}}, \end{aligned} \tag{3.15}$$

and so

$$\mathbf{E}_1 - \mathbf{E}_2 = \frac{\sigma}{\epsilon_0}\hat{\mathbf{n}}. \tag{3.16}$$

Combining this with Eq. 3.14 and rearranging gives

$$\epsilon_1 \mathbf{E}_1 \cdot \hat{\mathbf{n}} = \epsilon_2 \mathbf{E}_2 \cdot \hat{\mathbf{n}}, \tag{3.17}$$

which is the boundary condition for the component of $\mathbf{E}$ perpendicular to the boundary. The components of $\mathbf{E}$ parallel to the boundary are continuous across it (as can be seen by examining Eq. 3.16). In terms of the potential, these boundary conditions become

$$\epsilon_1 \nabla\varphi_1 \cdot \hat{\mathbf{n}} = \epsilon_2 \nabla\varphi_2 \cdot \hat{\mathbf{n}}, \tag{3.18}$$

and

$$\varphi_1 = \varphi_2. \tag{3.19}$$

Along with the modified Poisson's equation (Eq. 3.13) these are sufficient to allow an analytical solution to be attempted. Our iterative solution works by calculating the surface charge density, however. This can be obtained by substituting Eq. 3.15 into Eq. 3.14 and rearranging:

$$\sigma = P_B \mathbf{E}_{\text{ex}} \cdot \hat{\mathbf{n}}, \tag{3.20}$$

where

$$P_B = 2\epsilon_0 \frac{\epsilon_2 - \epsilon_1}{\epsilon_2 + \epsilon_1} \tag{3.21}$$

is a constant which describes the polarizability of the boundary. Eq. 3.20 gives the surface charge at the boundary in terms of the external field: that part of the electric field not from the charges on the local segment.

3.1.2 Born Energy

The simple model of a uniformly polarizable medium containing point charges ignores the finite radii of ions and water molecules: in reality polarization cannot continue all the way to the centre of an ion. This effect can be approximated by assuming a spherical region around the ion that cannot be polarized. This is called Born theory. The spherical boundary around the ion acquires a surface charge density, as described above, which is evenly distributed and reduces the field from the ion by a factor of $1/\epsilon$, just as for a point charge. So an ion with charge +1 is surrounded by a sphere with a total charge of $-(1-1/\epsilon)$ which shields it and reduces its effective charge at long range. In reality the polarizability of the water will vary continuously from the bulk value as an ion is approached, so the shielding charge will not form a sharply defined sphere.

The spherical dielectric boundary is a simplified model, but it does allow the interaction energy between an ion and the surrounding medium to be estimated. The Born energy incurred by moving an ion from a medium of dielectric constant ϵ_1 to one of dielectric constant ϵ_2 is

$$E_B = \frac{q^2}{8\pi\epsilon_0 r}\left(\frac{1}{\epsilon_2} - \frac{1}{\epsilon_1}\right). \tag{3.22}$$

This is from the electrostatic energy between an ion and the charge on the surrounding dielectric boundary. There is a factor of 1/2 because the induced charge is caused by the presence of the charge on the ion, and builds up gradually if the charge on the ion is brought in from infinity in small packets. As an example, consider a potassium ion surrounded by water. Let $r = 1.33$ Å (the crystal radius), $q = 1.6\times10^{-19}$ C, $\epsilon_2 = 80$, and $\epsilon_1 = 1$. Then E_B is -8.6×10^{-19} J or $-208\ \text{kT}_\text{r}$. The enthalpy of hydration for a potassium

ion is estimated to be -5.9×10^{-19} J or $-143\ \mathrm{kT_r}$. The enthalpy of hydration can be measured experimentally for a salt, but assigning this between the cation and anion requires some educated guesswork [10]. Nevertheless, the resulting uncertainty is not enough to explain the discrepancy between the prediction of Born theory and the experimentally derived value.

Rather, the discrepancy is due to the assumption of a sharp dielectric sphere, and the use of macroscopic electrostatic theory at the atomic scale. Under these circumstances 50% error is not too bad. It is usual to assign cations a larger effective radius for the purpose of Born energy calculations, however. Bockris and Reddy [10] suggest adding 0.85 Å to the crystal radius (giving 2.08 Å for potassium), Rashin and Honig [60] suggest using the covalent radius instead of the crystal radius (giving 2.06 Å), while for this project we derive an effective radius by substituting the estimated enthalpy of hydration into the Born energy equation and solving for the radius (giving 1.93 Å). Thus all of these methods give a similar result, and the differences between them are not worth worrying about given the larger uncertainties involved in applying macroscopic electrostatic theory at such a small scale, and the limited use made of Born energy estimates in our simulations (we use them only to provide compensation for the difference between the dielectric constant in the reservoirs and pore when the dielectric constant has been reduced from the bulk value, see section 8.1.4). This increased radius can be thought of as accounting for the finite radius of the water molecules, but as already indicated, the situation is in reality more complex. For example, using the ionic radius of anions in the Born energy equation provides a reasonable estimate of the enthalpy: their effective radius does not need to be adjusted. This is because there are differences between the hydration of a cation and an anion at the atomic scale.

3.1.3 Induced Surface Charge

The concept of induced surface charge provides an intuitive picture of the effect of dielectrics and dielectric boundaries on the electric field. An ion in water is surrounded by a sphere of induced charge of the opposite polarity, which partially shields the charge on the ion, reducing the electric field. If the ion approaches a dielectric boundary with protein ($\epsilon = 2$ compared to $\epsilon = 80$ for water), then charge of the same polarity is induced, tending to repel the ion from the boundary. Viewed from a distance in the medium of lower dielectric constant, the ion has a much larger effective charge than it has in water. The charge on the boundary must undo much of the shielding of the ion: it must be of the same polarity as the ion.

Lowering the dielectric constant used for the water increases the repulsion, which is surprising because the repulsion must disappear where water and protein have the same dielectric constant. Examining Eq. 3.20 shows that the induced surface charge is proportional to the strength of the field,

and also proportional to a coefficient depending on the the dielectric constants, $(\epsilon_2 - \epsilon_1)/(\epsilon_2 + \epsilon_1)$. If the dielectric constant for water is dropped from 80 to 40, while that for protein remains 2, the coefficient drops from 0.95 to 0.90. The field due to an ion doubles, however, its effective charge increased by the reduced shielding ability of the water. Only when ϵ_1 and ϵ_2 are nearly equal does the induced surface charge tail off.

3.1.4 Limitations of Macroscopic Electrostatics

In using macroscopic electrostatic theory the effects of induced and rotating dipoles in water and protein are summarized by the dielectric constant and the modified Poisson's equation (Eq. 3.13). The concern in applying this theory to channels is that the concept of a dielectric constant may be completely invalid on such a small scale. After all, the dipoles that are creating the fields have dimensions that are a reasonable fraction of the scale of the system, while macroscopic electrostatic theory considers them to be infinitesimal. There are reasons for thinking that the theory is still useful, however, even on such small scales. One reason is the success of Born theory in explaining the hydration energy of ions. Although the errors in prediction of energy can be large ($> 50\%$), the theory remains a useful way of estimating the energy, and can be modified to provide more accurate answers. Another reason is that macroscopic electrostatic theory gives qualitatively similar results to microscopic simulations, even in confined spaces. For example the observation from MD studies that an ion in a narrow channel aligns the water into chains is similar to electrostatic calculations which show that a channel concentrates the electric field along its axis. In a macroscopic electrostatic calculation the field from an ion in a narrow pore would be unable to escape into the surrounding low dielectric strength medium, and would therefore remain nearly constant until the pore widened out, rather than decaying with the inverse square of the distance as it would in bulk water. In microscopic terms the dipoles would tend to align along the axis of the pore, which is the observation from MD. In summary we believe that macroscopic electrostatic theory is a useful way of estimating the electrostatic forces on ions in a channel, although the errors may be large in the regions of the pore where the radius is smallest.

Where the theory cannot be of any help is in calculating the detailed interactions where an ion is forced into close contact with the protein. An example of this is the selectivity between ions produced by a selectivity filter. The different energy barriers experienced by different species of ion (of the same valence) are lumped together by the large errors in electrostatic calculation in the narrowest regions. Macroscopic electrostatic theory still provides an estimate of the energy barrier height, and we belive a useful one for the purpose of studying conductance throughout the channel, but the subtleties that produce selectivity are lost.

If macroscopic electrostatic theory is a valid approach, but subject to large errors, the obvious question is how could these errors be reduced? The answer is by relaxing the assumptions made above (section 3.1.1) of constant dielectric strength and linear dielectric response. The dielectric strength of water in a channel may be quite different from that in bulk, but our present approach does not allow it to be varied, except at dielectric boundaries. Hence we either have to use the bulk dielectric constant throughout the simulation, or introduce a smaller effective dielectric constant for the channel. Using an effective dielectric constant means that the dielectric strength in the reservoirs is wrong. In chapter 8 we compensate for this by introducing an ad hoc Born energy barrier at the mouths of the channel (section 8.1.4), but this is not a very satisfactory solution. Although an effective dielectric constant is a useful concept for a pore of constant radius [57] our simulations include reservoirs and channels with complex shapes. If the dielectric strength changes between bulk water and water in a narrow pore it would seem to be a function of pore radius, and in our context would need to vary throughout the length of the pore. And if dielectric strength is allowed to vary in space then the assumption of linear polarizability also should be relaxed. The details of the shielding of an ion by dipoles would need to be calculated explicitly, instead of by the use of an effective charge as with our present approach. However, close to an ion the field strength is large enough to completely align the water dipoles. In macroscopic terms the polarizability is no longer linear, but is subject to saturation. Indeed Partenskii and Jordan [57] point out that if the pore is narrow enough this dipole alignment and high field strength is propagated throughout the channel.

The challenge then is to invent a way of solving the electrostatic equations for a system where the polarizability varies in space and is subject to saturation. An iterative solution to such a system would be possible, but would have to be done in the full three dimensions, since polarization charges would not be confined to the boundaries. Important considerations would be the ability to deal with smooth channel boundaries and the ability to concentrate computational effort where most needed, that is in the narrow regions of the channel and close to the ions. Another concern would be the effect on the lookup table method of speeding up the simulations (described in chapter 6), since this depends on superposition of solutions for individual ions, which in turn depends on linear dielectric response.

Although producing such an improved iterative solution would be a challenge, a greater challenge would be its calibration: there is no point in allowing for variable polarizability unless it is known how it varies. This calibration would involve an extensive series of MD simulations for a model channel as similar as possible to the BD model. There are various ways of estimating the dielectric constant in an MD simulation. The important issue here, however, is not the rotational mobility of the ions as such, but rather the forces on the ions, which are needed for the BD simulations. The

safest procedure would be to calculate the potential energy profile for an ion traversing the channel, and then define an effective dielectric strength function which causes the iterative electrostatic profile to match that from the MD simulations. Saturation of polarizability could be investigated by varying the charge on the ion. With dielectric strength and saturation established, the new electrostatic model would be able to cope with multiple ions in the channel, assuming the basic concept of dielectric strength is valid in channels. This could be checked by further MD simulations with multiple ions.

Unfortunately calculating such energy profile using MD is tricky. Care has to be taken to properly define the macroscopic concept of electrostatic potential energy in terms of the microscopic quantities available from the MD simulation, and drift in temperature and pressure may affect the result unless prevented or compensated for. Another difficulty is the long runs needed to reduce the statistical uncertainty in points on the energy profile. The macroscopic potential energy of an ion is, from the point of view of an MD simulation, a long timescale average of rapidly fluctuating quantities. Reducing uncertainty in the potential energy to $\pm 1\,\mathrm{kT}$ would require very long runs, but might be necessary to provide an energy profile smooth enough to be used for BD. The BD simulations described here show that sharp energy barriers as small as 3-4 kT can greatly reduce the conductance of a channel. An energy profile with points subject to random variations of $\pm 2\,\mathrm{kT}$ could easily produce a spurious barrier of this size. The profile could be smoothed, but this would also remove any genuine sharp barriers along with the artefacts. Such a procedure would remove much of the attraction of doing the MD calculation in the first place.

A more sophisticated electrostatic model is desirable then, but beyond the scope of this project, its construction and calibration being a large project in its own right. For the time being we are stuck with the simplified electrostatic model described here. Despite the inevitable errors involved, the use of this model does not prevent our simulations from producing useful results. We can explore aspects of channel conductance usually not considered in simulation, namely the effect on conductance of the overall shape and charge distribution of the channel, as well as long range interactions between multiple ions. We can make predictions about conductance which can be compared with experiment, expecting, in light of the above discussion, that these predictions will be correct to the extent that overall channel shape, long range electrostatics, and diffusion processes are responsible for channel conductance, and incorrect to the extent that detailed interactions between water, protein, and ions are responsible for conductance. Simplifying the electrostatics model to make the prediction of conductance possible is consistent with the project's strategy. The effects of this simplification on the validity of the method, although not fully known as yet, are at least capable of being identified by checks against experiment and microscopic simula-

tion, and if necessary reduced by the use of more sophisticated techniques of electrostatics.

For the current project the use of simplified electrostatics has implications for the way we build model channels and interpret results. Model channels should reflect, as far as it is know, the overall shape and charge distribution of the real channel. Exact replication of the real channel, especially small details, is unnecessary and potentially misleading, as our simplified electrostatics is incapable of faithfully reflecting the effect of such small details on the potential energy of ions traversing the channel, and the resulting effects on conductance. In a similar vein, we should not yet expect to reproduce from a model channel the exact conductance of the real channel on which it is based. Rather, we should hope that the model channel's conductance will show the general characteristics of the real channel's conductance. These expectations may seem modest, after all the effort needed to make our BD method work, and compared to the ability of other theories such as PNP and RRT to produce an exact quantitative match to channel conductance by adjusting parameters. However, we believe it is important to build a theory to predict conductance from channel structure, rather than relying on adjustable parameters, now that computer technology makes this possible, and we do not pretend that this project is more than another step in this direction.

3.2 Outline Generation

To represent a channel using the macroscopic theory of electrostatics, we need a sharp boundary between water and protein, a boundary described in three dimensions. We assume that channel boundaries are cylindrically symmetric, which simplifies the problem: we describe the outline of a channel as a curve in two dimensions, and then rotate the outline around the channel axis to produce a three dimensional surface. Note that only the boundary is cylindrically symmetric. Ions and fixed charges in the protein are represented as point charges in three dimensional space, so the total system of ions, fixed charges, and boundary will not have cylindrical symmetry. Examples of channel outlines are shown in Fig. 3.1.

The channel outlines are built up piece by piece from sections of line, arc, and catenary. Each section has its own parametric equations, expressed in local coordinate t, and these need to be assembled to form parametric equations for the complete outline, expressed in global coordinate s. Both t and s coordinates are scaled to be path lengths: they measure distance along the curve. The s coordinate is defined to be 0 at the minimum r value of those points with the minimum z value, that is the lower left corner of the outline. It increases as the curve proceeds clockwise around the outline.

Each section is described by its type, and the following attributes:

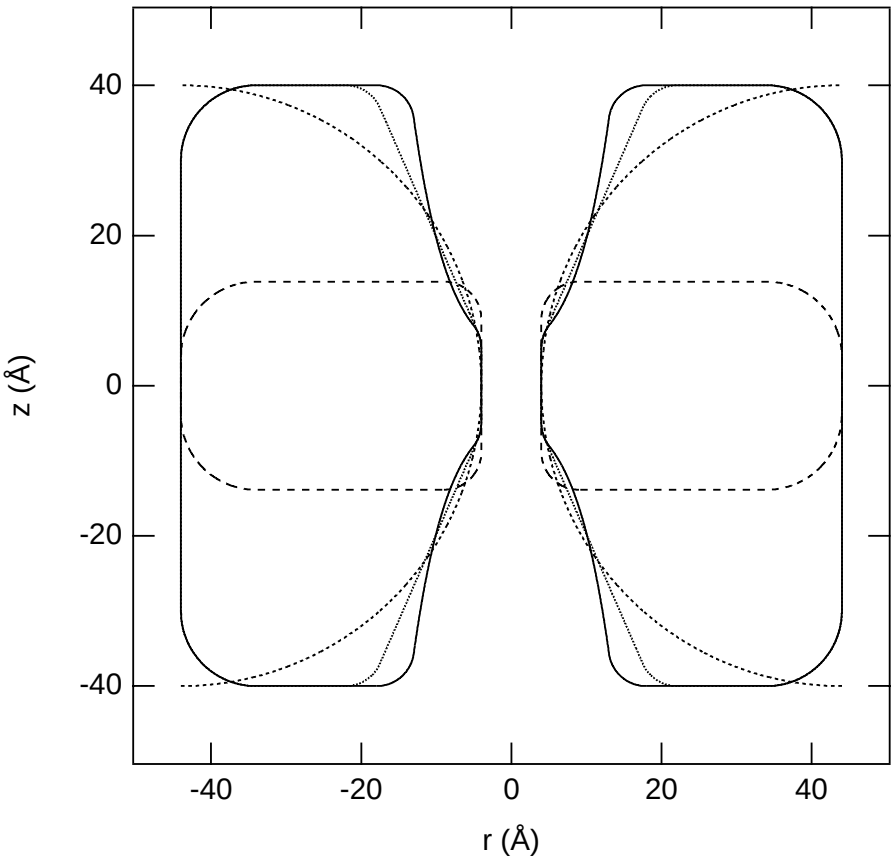

Figure 3.1: Example channel outlines for catenary, biconical, toroidal, and cylindrical channels. The outlines have been reflected about the z axis to better show the shape of the pore. The outline of the toroidal channel has been truncated at $r = 44$ Å: it continues in a full circle out to $r = 84$ Å. For all channels the minimum pore radius ($r_{\rm neck}$) is 4 Å. The catenary and biconical channels have a neck length ($h_{\rm neck}$) of 35 Å, for a total length of 80 Å. The catenary channel has mouth radii ($r_{\rm vtop}$, $r_{\rm vbot}$) of 13 Å, while those of the biconical channel are 17.5 Å. The cylindrical channel has a neck length ($h_{\rm neck}$) of 17.7 Å, plus two corners of radius 5 Å, for a total length of 27.7 Å. All channels except for the torus have an outer radius ($r_{\rm chan}$) of 44 Å. The mouth radii of the catenary and biconical channels, and the length of the cylindrical channel have been adjusted so that all four channels present a potential energy barrier of the same height.

R_j, Z_j	offset in (r, z) coordinates,
a_j	scale factor, or slope for a line,
u_j, v_j	start and end of the section in t coordinate.

The types of sections, and their parametric equations, are as follows.

Line A straight line in the direction of angle a_j passing through point (R_j, Z_j). This is the point where $t = 0$, and t ranges from $-\infty$ to ∞.

$$\begin{aligned} r_j(t) &= R_j + t\cos(a_j) \\ z_j(t) &= Z_j + t\sin(a_j) \\ \theta_j(t) &= a_j. \end{aligned} \tag{3.23}$$

Arc 1 A semi-circle centred on point (R_j, Z_j) with radius a_j. The arc sweeps clockwise from $-\pi/2$ to $\pi/2$ as t runs from 0 to πa_j.

$$\begin{aligned} r_j(t) &= R_j - a_j\sin(t/a_j) \\ z_j(t) &= Z_j - a_j\cos(t/a_j) \\ \theta_j(t) &= \pi - t/a_j. \end{aligned} \tag{3.24}$$

Arc 2 A semi-circle centred on point (R_j, Z_j) with radius a_j. The arc sweeps clockwise from $\pi/2$ to $-\pi/2$ as t runs from 0 to πa_j.

$$\begin{aligned} r_j(t) &= R_j + a_j\sin(t/a_j) \\ z_j(t) &= Z_j + a_j\cos(t/a_j) \\ \theta_j(t) &= -t/a_j. \end{aligned} \tag{3.25}$$

Catenary 1 Half of the positive branch of a catenary, with the origin at (R_j, Z_j) and with scale factor a_j. The curve starts at $(R_j, Z_j + a_j)$, where t is 0, and t runs from 0 to ∞.

$$\begin{aligned} r_j(t) &= R_j + a_j\sinh^{-1}(t/a_j) \\ z_j(t) &= Z_j + \sqrt{t^2 + a_j^2} \\ \theta_j(t) &= \tan^{-1}(t/a_j). \end{aligned} \tag{3.26}$$

Catenary 2 Half of the negative branch of a catenary, with the origin at (R_j, Z_j) and with scale factor a_j. The curve ends at $(R_j, Z_j - a_j)$, where t is 0, and t runs from $-\infty$ to 0.

$$\begin{aligned} r_j(t) &= R_j + a_j\sinh^{-1}(-t/a_j) \\ z_j(t) &= Z_j - \sqrt{t^2 + a_j^2} \\ \theta_j(t) &= \pi + \tan^{-1}(t/a_j). \end{aligned} \tag{3.27}$$

The sections are assembled into a single curve by defining w_j to be the end of each section in the global coordinate s:

$$\begin{aligned} w_0 &= 0 \\ w_j &= w_{j-1} + (v_j - u_j). \end{aligned} \tag{3.28}$$

Then the global parametric equations are

$$\begin{aligned} r(s) &= r_j(s - w_{j-1}), \qquad j : w_{j-1} \le s < w_j \\ z(z) &= z_j(s - w_{j-q}), \qquad j : w_{j-1} \le s < w_j. \end{aligned} \tag{3.29}$$

To form a continuous outline, without any sharp corners, the sectors must satisfy

$$\begin{aligned} z_j(u_j) &= z_{j-1}(v_{j-1}) \\ r_j(u_j) &= r_{j-1}(v_{j-1}) \\ \theta_j(u_j) &= \theta_{j-1}(v_{j-1}), \end{aligned} \tag{3.30}$$

where $j = 0$ is considered equivalent to $j = n$, n being the number of sectors: the start of the first sector ($j = 1$) must match the end of the last sector ($j = n$ equivalent to $j = 0$).

Although this piecewise method of describing the channel shape allows great flexibility, choosing section attributes so that the outline is continuous and smooth can be difficult. We compromise by defining channel types, each of which has a fixed number of sectors and a fixed overall shape, but has channel parameters which control its dimensions. The section attributes are generated automatically from the parameters, with the aid of a root finding algorithm where necessary. The parameters for toroidal and cylindrical channels are shown in Fig. 3.2. The parameters for catenary and biconical channels are shown in Fig. 3.3. The effect of changing the channel parameters for a catenary channel is illustrated in Fig. 3.4. Fig. 3.4 A shows the effect of variation in the r_{neck} and r_{chan} parameters. Fig. 3.4 B shows the effect of variation in the h_{vtop} and r_{vbot} parameters: note that the shapes of the vestibules can be adjusted independently. Fig. 3.4 C shows the effect of variation in the h_{neck} parameter: note that this changes the total height of the channel as well as the height of the neck. Fig. 3.4 D shows the effect of variation in the r_{cnr} parameter.

3.3 Tiling the Boundary

Having generated the outline, the next step is to generate the surface charge sectors which tile the boundary. This is done by slicing the outline into rings, so called because when the outline is rotated they become rings of surface charge sectors. The rings are not evenly spaced around the outline.

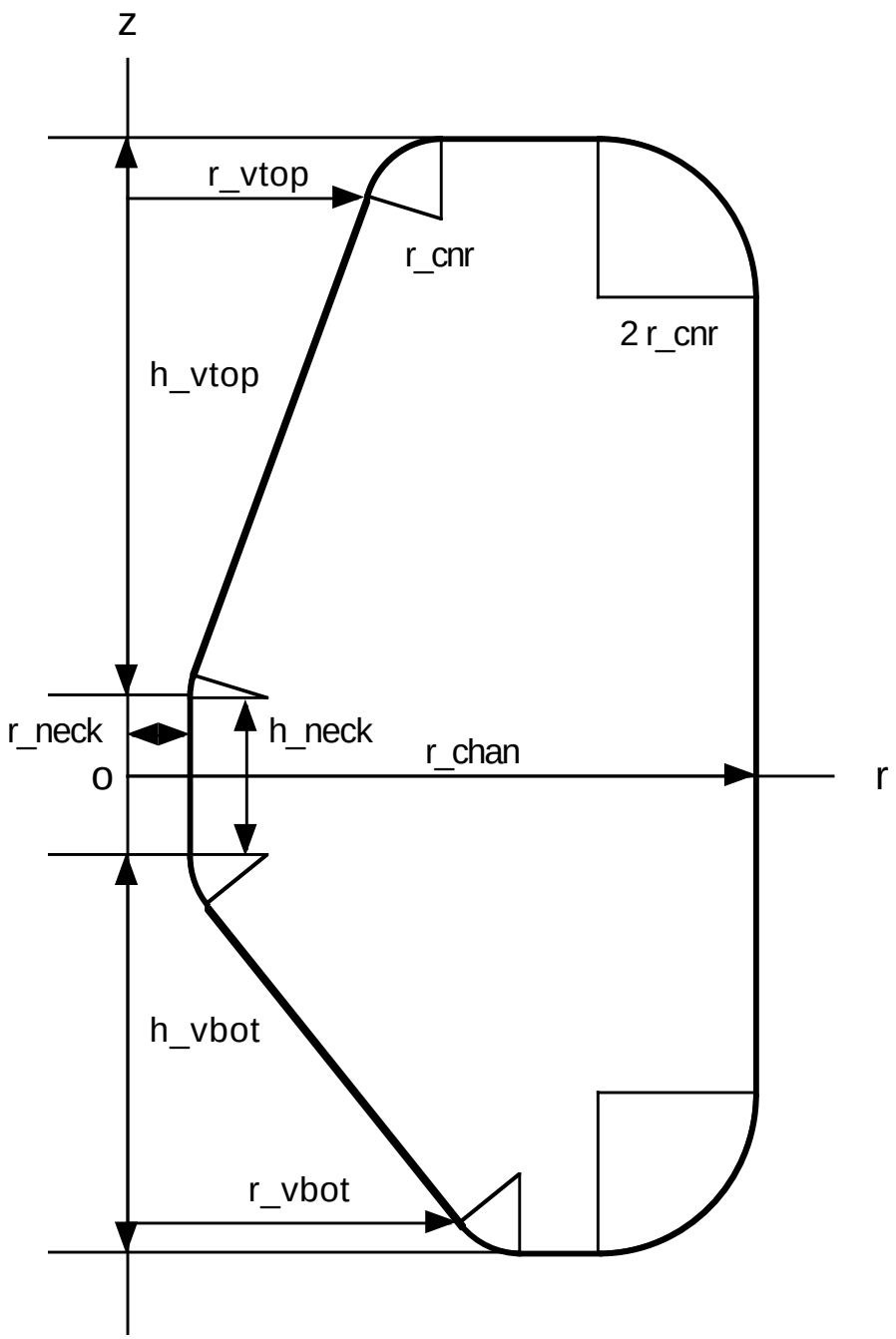

Figure 3.2: Catenary and bicone parameters

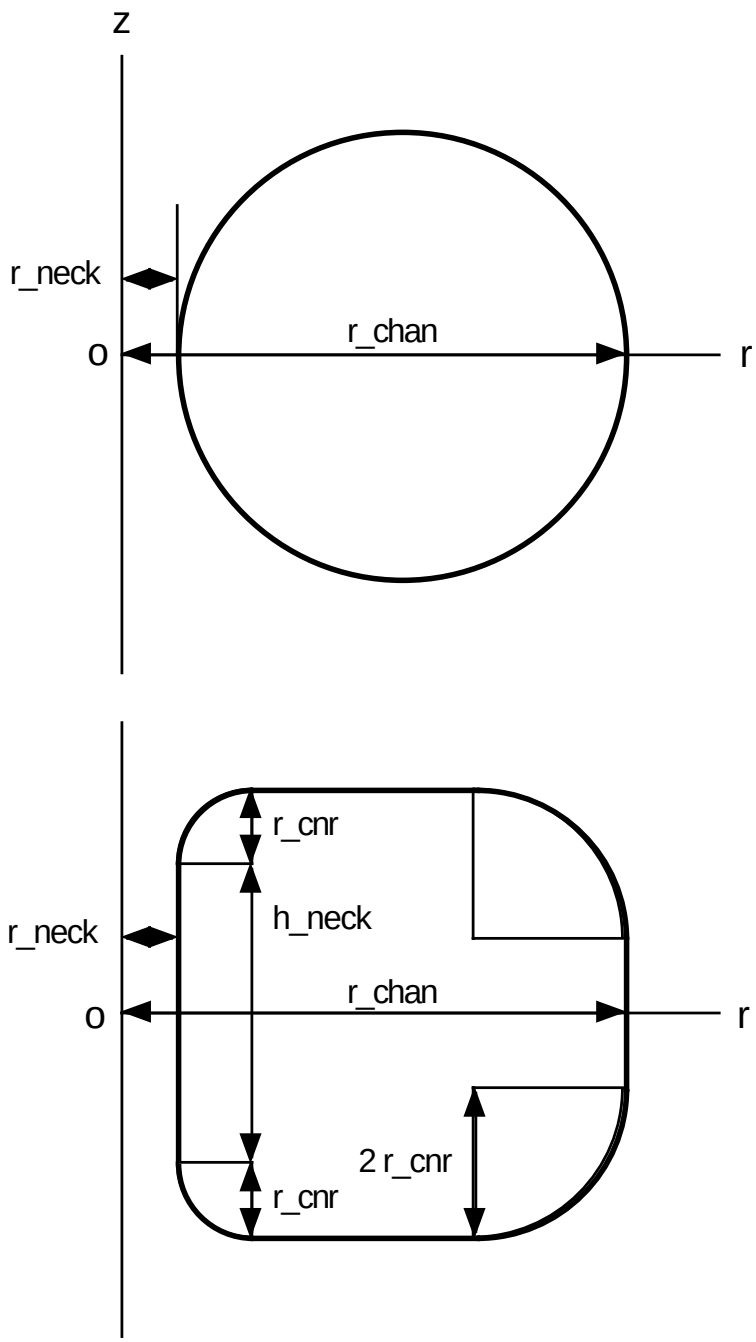

Figure 3.3: Torus and cylinder parameters

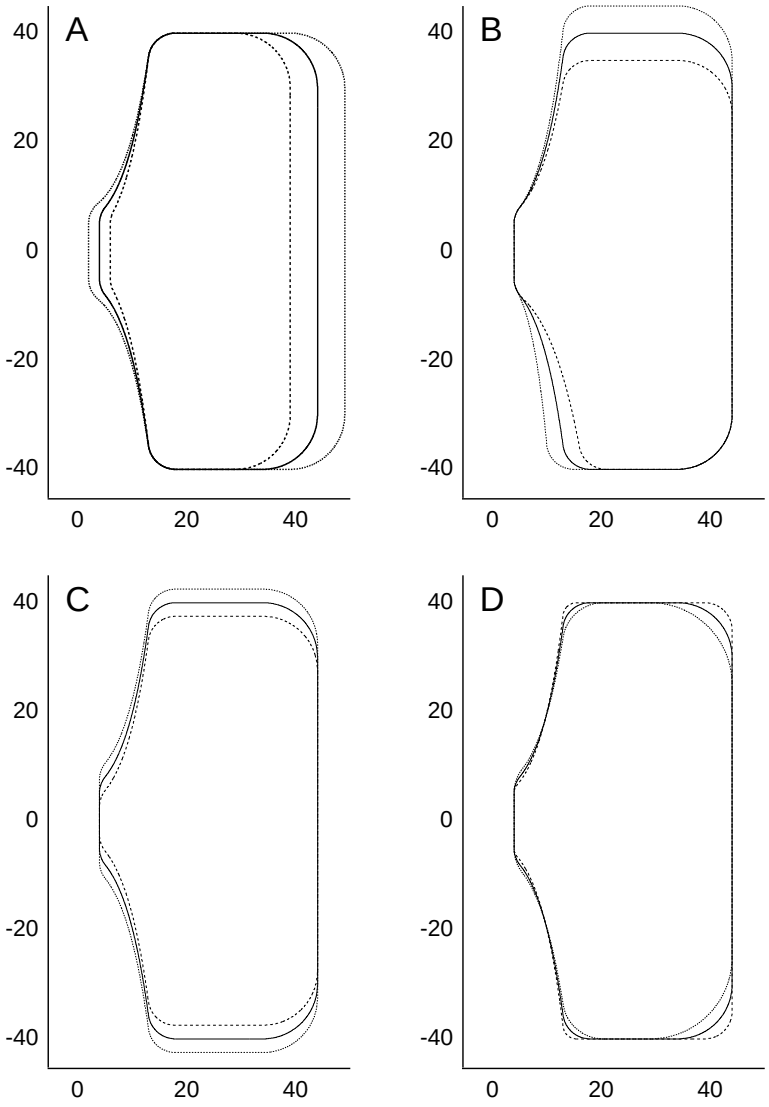

Figure 3.4: Effect of changing channel parameters. The vertical axes are for z, the horizontal axes are for r. The axes are labeled in Å. In A, r_{neck} changes from 2 to 4 to 6 Å, while r_{chan} changes from 39 to 44 to 49 Å. In B, h_{vtop} changes from 30 to 35 to 40 Å, while r_{vbot} changes from 10 to 13 to 16 Å. In C, h_{neck} changes from 5 to 10 to 15 Å. In D, r_{cnr} changes from 2.5 to 5 to 7.5 Å.

The accuracy of the iterative method depends on the spacing of the sectors. in particular it cannot be expected to give accurate results for points closer to the boundary than the sector spacing (see section 3.6). The computer resources required, however, are proportional to the inverse fourth power of the sector spacing. This places a practical limit on the number of sectors that can be used (10 to 15 thousand sectors on the VPP). To make the best use of the available resources it is important to vary the spacing between sectors, reducing it in areas where ions come close to the boundary, and increasing it in areas where they do not.

3.3.1 Sector Spacing

We do this by defining three regions of the boundary. The first is the neck region, the constricted part of the channel where ions are forced into close proximity to the boundary. The second is the vestibule region, the vestibules and top and bottom surfaces of the channel, where ions will occasionally approach the boundary closely. The third is the outer region, the outer corners and outside surface of the channel. In our BD simulations the ions are restricted to cylindrical reservoirs with radii smaller than the radius of the outer edge of the channel, located above and below the channel. The ions therefore do not approach the outer region. The sector spacing can be much larger here, as the errors in the iterative method are small when then point of interest is far from the boundary compared to the sector spacing.

The neck region is defined by vertical limits

$$-h_{\text{ns\_bot}} \leq z \leq h_{\text{ns\_top}}, \tag{3.31}$$

the vestibule region by horizontal limits

$$r \leq \begin{cases} r_{\text{vs\_top}}; & z \geq 0 \\ r_{\text{vs\_bot}}; & z < 0, \end{cases} \tag{3.32}$$

and the outer region is the rest of the outline. The nominal spacings for the regions are Δs_{neck} , Δs_{vest} , and Δs_{out} , usually set to 0.5 Å, 1 Å, and 10 Å respectively. These spacings are scaled by the ring generation algorithm to keep the number of sectors under a specified limit: this makes the memory use of the program predictable. The scale factor is called λ and is usually between 1.2 and 1.5, so the real spacings are larger than the nominal spacings by this factor.

Although the sector spacing needs to vary, it should not jump suddenly, as nearby sectors need to be spaced reasonably evenly for the iterative algorithm to work. To achieve this we define a ramp function which increases the spacing linearly from the smaller to the larger, for 50% beyond the smaller

region's limit. The function is

$$F_{\text{ramp}}(x, x_{\text{lim}}, \Delta s_1, \Delta s_2) = \begin{cases} \Delta s_2; & x > 1.5x_{\text{lim}} \\ \Delta s_1 + 2\left(\frac{x - x_{\text{lim}}}{x_{\text{lim}}}\right)(\Delta s_2 - \Delta s_1); & x_{\text{lim}} < x \leq 1.5x_{\text{lim}} \\ \Delta s_2; & x \leq x_{\text{lim}}, \end{cases} \tag{3.33}$$

and so the nominal spacing is given by

$$\Delta s(r, z) = \begin{cases} F_{\text{ramp}}(r, r_{\text{vs\_top}}, \\ \quad F_{\text{ramp}}(z, h_{\text{ns\_top}}, \Delta s_{\text{neck}}, \Delta s_{\text{vest}}), \\ \quad\quad \Delta s_{\text{out}}); & z \geq 0 \\ F_{\text{ramp}}(r, r_{\text{vs\_bot}}, \\ \quad F_{\text{ramp}}(-z, h_{\text{ns\_bot}}, \Delta s_{\text{neck}}, \Delta s_{\text{vest}}), \\ \quad\quad \Delta s_{\text{out}}); & z < 0. \end{cases} \tag{3.34}$$

The regions are defined in terms of the outline parameters for the various types of outline. For a toroidal channel

$$\begin{array}{rclcl} h_{\text{ns\_top}} & = & h_{\text{ns\_bot}} & = & \frac{1}{4} r_{\text{tor}} \\ r_{\text{vs\_top}} & = & r_{\text{vs\_bot}} & = & r_{\text{neck}} + \frac{3}{4} r_{\text{tor}}, \end{array} \tag{3.35}$$

where $r_{\text{tor}} = (r_{\text{chan}} - r_{\text{neck}})/2$ is the radius of the torus. For a cylindrical channel

$$\begin{array}{rclcl} h_{\text{ns\_top}} & = & h_{\text{ns\_bot}} & = & \frac{2}{3}(\frac{1}{2} h_{\text{neck}} + r_{\text{cnr}}) \\ r_{\text{vs\_top}} & = & r_{\text{vs\_bot}} & = & r_{\text{chan}} - 2r_{\text{cnr}}, \end{array} \tag{3.36}$$

and for a biconical or catenary channel

$$\begin{array}{rclcl} h_{\text{ns\_top}} & = & h_{\text{ns\_bot}} & = & \frac{1}{2} h_{\text{neck}} + r_{\text{cnr}} \\ r_{\text{vs\_top}} & = & r_{\text{vs\_bot}} & = & r_{\text{chan}} - 2r_{\text{cnr}}. \end{array} \tag{3.37}$$

All of the neck limits leave enough space for the vestibule spacing to be reached by the top and bottom of the channel, hence the factor of $\frac{2}{3}$ in the cylinder limits. However, except for the toroidal channel the vestibule limits usually do not allow the full outer spacing to be reached.

3.3.2 Ring Generation

The ring generation algorithm seeks to divide the outline into rings, based on the parametric equations for the outline, $r(t)$ and $z(t)$, and the sector spacing $\Delta s(t) = \Delta s(r(t), z(t))$. The algorithm begins by calculating three new functions

$$\begin{aligned} A(t) &= \int_0^t 2\pi r(t')\, dt' \\ M(t) &= \int_0^t \frac{1}{\Delta s(t')}\, dt' \\ N(t) &= \int_0^t \frac{2\pi r(t')}{\Delta s(t')}\, dt, \end{aligned} \tag{3.38}$$

these being the cumulative totals of the boundary area, the number of rings at nominal spacing, and the number of sectors at nominal spacing, respectively.

The scaling factor λ and the number of rings m are determined as follows. The minimum scaling factor, $\lambda_{\min}$, depends on the limit on the total number of sectors, $n_{\lim}$:

$$\lambda_{\min} = \sqrt{N(t_{\max})/n_{\lim}}, \tag{3.39}$$

where $t_{\max}$ is the path length of the outline. The number of rings is then

$$m = \lfloor M(t_{\max})/\lambda_{\min} \rfloor, \tag{3.40}$$

and the final value for λ is

$$\lambda = M(t_{\max})/m. \tag{3.41}$$

The rings can now be described in the t coordinate:

$$\begin{aligned} t_0 &= 0 \\ t_i &= \max\, t : M(t)/\lambda \leq i,\ i = 1 \ldots n, \end{aligned} \tag{3.42}$$

and

$$T_i = \frac{t_i - t_{i-1}}{2}, \tag{3.43}$$

so that t_{i-1}, t_i, and T_i are the beginning, end, and centre of ring i, respectively. Additional ring attributes are

$$A_i = A(t_i) - A(t_{i-1}), \tag{3.44}$$

the total area of ring i,

$$\Delta s_i = \lambda \Delta s(T_i), \tag{3.45}$$

the target spacing for ring i, and

$$\Delta t_i = t_i - t_{i-1}, \tag{3.46}$$

the thickness of the ring. Note that Δs_i is the target spacing used for breaking the ring into sectors, while Δt_i is the actual path length across the ring, used for calculating its normals and polarizability.

The centres of the rings for a catenary channel are shown in Fig. 3.5. This figure shows that sectors are concentrated in the neck region of the channel, and very sparse in the outer region, where they are far from the ions in a simulation. It also shows that the variation in spacing is done smoothly.

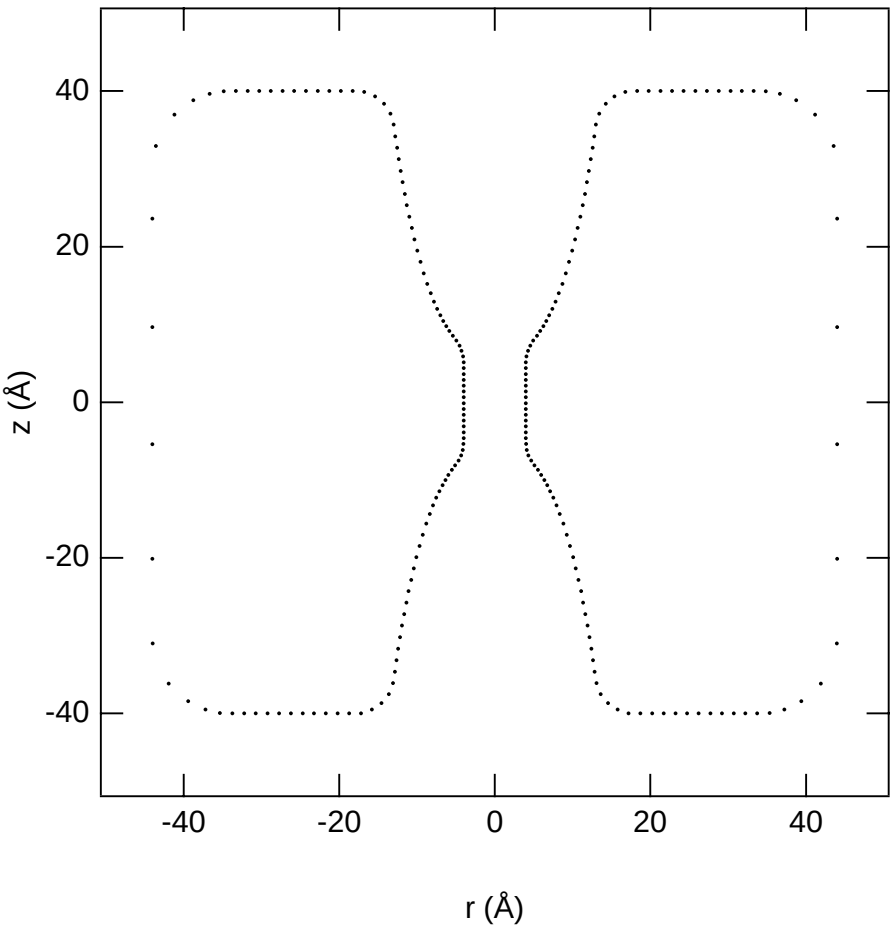

Figure 3.5: Sector spacing for a catenary channel. Δs_{neck} is 0.5 Å, Δs_{vest} is 1 Å, and Δs_{out} is 10 Å. The channel parameters are $h_{\text{neck}} = 10$ Å, $r_{\text{chan}} = 44$ Å, and $r_{\text{cnr}} = 5$ Å, so $h_{\text{ns\_top}}$ and $h_{\text{ns\_bot}}$ are 10 Å, and $r_{\text{vs\_top}}$ and $r_{\text{vs\_bot}}$ are 34 Å.

3.3.3 Sector Generation

The final step, now that the outline has been divided into rings, is to generate sectors by rotating each ring around the z axis. First we need the values and derivatives of r and z at the centre of each ring:

$$\begin{aligned} r_i &= r(T_i) \\ r'_i &= \frac{r(t_i) - r(t_{i-1})}{\Delta t_i} \approx r'(T_i), \end{aligned} \tag{3.47}$$

and

$$\begin{aligned} z_i &= z(T_i) \\ z'_i &= \frac{z(t_i) - z(t_{i-1})}{\Delta t_i} \approx z'(T_i). \end{aligned} \tag{3.48}$$

Then the normal to the ring at its centre $(\hat{r}_i, \hat{z}_i)$ is given by

$$\begin{aligned} \hat{r}_i &= -z'_i/\gamma_i \\ \hat{z}_i &= r'_i/\gamma_i, \end{aligned} \tag{3.49}$$

where

$$\gamma_i = \sqrt{r'^2_i + z'^2_i}. \tag{3.50}$$

The outline goes clockwise with increasing t, so this normal points out from the channel boundary, towards the water.

3.4 Iterative Algorithm

3.4.1 Basic Algorithm

The first step in the iterative algorithm is to calculate the electric field due to the permanent charges at each of the surface charge sectors. The normal for each sector is taken at its centre point, and along with the external electric field this allows the surface charge of the sector to be calculated from Eq. 3.20. Of course this is only an initial estimate of the surface charge, since the electric field from the rest of the surface has been ignored. However, this estimated surface charge is now converted into charge at the surface charge centres, and the process is repeated, with the electric field at each sector calculated not only from the permanent charges, but also from the last estimate of the induced charges. This yields a better estimate of the surface charge, which is again fed into the electric field calculation, and the iterations continue until the system converges, that is the surface charge estimates stop changing.

Symbols

N Number of permanent charges (ions and dipoles).

$\mathbf{R}_i$ Position of permanent charges.

Q_i Effective charge of permanent charges (charge divided local ϵ).

m Number of surface charge centres.

$\mathbf{r}_i$ Position of surface centres.

ΔS_i Area of surface charge sectors.

$\hat{\mathbf{n}}_i$ Normal to surface at $\mathbf{r}_i$.

$\mathbf{E}_i^{(k)}$ External electric field at sector i after algorithm step k.

$\sigma_i^{(k)}$ Surface charge density of sector i after step k.

$q_i^{(k)}$ Charge on surface charge centre i after step k.

$\delta_i^{(k)}$ Normalized absolute change in charge centre i during step k.

Δ Tolerance for convergence (scaled absolute error).

Algorithm

1. Calculate the field at the centre of the sectors from the permanent charges:

$$\mathbf{E}_i^{(0)} = \sum_{j=1,N} \frac{Q_j}{4\pi\epsilon_0} \frac{(\mathbf{r}_i - \mathbf{R}_j)}{|\mathbf{r}_i - \mathbf{R}_j|^3}. \tag{3.51}$$

   Set k to 1.

2. Allocate new charges to the sectors based on the electric field:

$$\sigma_i^{(k)} = P_B \mathbf{E}_i^{(k-1)} \cdot \hat{\mathbf{n}}_i \tag{3.52}$$

$$q_i^{(k)} = \sigma_i^{(k)} \Delta S_i. \tag{3.53}$$

3. Recalculate the electric field at the surface charge centres:

$$\mathbf{E}_i^{(k)} = \mathbf{E}_i^{(0)} + \sum_{j=1,m;\, j\neq i} \frac{q_j^{(k)}}{4\pi\epsilon_0} \frac{(\mathbf{r}_i - \mathbf{r}_j)}{|\mathbf{r}_i - \mathbf{r}_j|^3}. \tag{3.54}$$

4. Check for convergence:

$$\delta_i^{(k)} = \left| \frac{q_i^{(k)} - q_i^{(k-1)}}{q_{\max}^{(k)}} \right|, \tag{3.55}$$

where $q_{\max} = \max(|q_i|)$. If $\delta_i^{(k)} < \Delta \ \forall i$ and $k \geq 10$ then finish, otherwise set k to $k+1$ and go to 2.

3.4.2 Convergence

The algorithm needs to test for convergence of the system in order to decide when to stop, and this is done by estimating the error in the solution from the change in surface charge values from step to step. The system is assumed to have converged sufficiently when the maximum error is less than some specified value. We at first tried estimating the fractional error

$$\delta_i^{(k)} = \left| \frac{q_i^{(k)} - q_i^{(k-1)}}{q_i^{(k-1)}} \right|, \tag{3.56}$$

with a tolerance δ_i of 0.01. The intent was to reduce the error in the potential due to convergence to under 1%. However, this resulted in variations in the number of steps taken and the accuracy of the solution depending on the starting conditions. The problem is that by using fractional errors detection of convergence may be controlled by small errors in surface charge centres far from the ion, which have little effect on the solution. The larger surface charges close to the ion are far more important and this should be reflected in the convergence condition. We switched to using absolute errors scaled by the largest surface charge in the system

$$\delta_i^{(k)} = \left| \frac{q_i^{(k)} - q_i^{(k-1)}}{q_{\max}^{(k)}} \right|. \tag{3.57}$$

With $\Delta = 0.0001$ this method produced satisfactory results without the instability of using fractional errors.

3.4.3 Pre-Calculation of Interactions

The basic algorithm recalculates the interactions between all the surface charge centres at each step. Since the position of the sectors is known and fixed once the boundary has been divided up, much of this work is redundant. The distance and direction between surface charge centres does not change between steps, or even if the algorithm is re-run for a new set of permanent charges, provided the boundary stays the same. This observation provides a means of speeding up the algorithm, at the expense of a larger requirement for memory. The interaction between each pair of surface charge

centres can be pre-calculated and summarized as a single number, part of a square matrix with dimensions equal to the number of surface charge centres, an m by m matrix. Then the new surface charges at each step can be calculated quickly by multiplying the vector of old surface charges by the matrix, and adding the surface charge due to permanent charges. This optimization can result in a large speedup, provided enough memory to hold the matrix is available, and the matrix can be rapidly read into the processor (or processors). These conditions apply in the case of the vector architecture machine we use, and are likely hold for other high-performance architectures. For a desktop machine, however, the basic algorithm may be better.

The formula for the interaction matrix B_{ij} is derived as follows. Let

$$\mathbf{A}_{ij} = \frac{1}{4\pi\epsilon_0} \frac{(\mathbf{r}_i - \mathbf{r}_j)}{|\mathbf{r}_i - \mathbf{r}_j|^3}. \tag{3.58}$$

By substituting $k-1$ for k, Eq. 3.54 becomes

$$\mathbf{E}_i^{(k-1)} = \mathbf{E}_i^{(0)} + \sum_{j=1,m;\, j\neq i} \mathbf{A}_{ij} q_j^{(k-1)}, \tag{3.59}$$

and this can be substituted into Eq. 3.52

$$\begin{aligned} \sigma_i^{(k)} &= P_B \mathbf{E}_i^{(k-1)} \cdot \hat{\mathbf{n}}_i \\ &= P_B \mathbf{E}_i^{(0)} \cdot \hat{\mathbf{n}}_i + \sum_{j=1,m;\, j\neq i} P_B (\mathbf{A}_{ij} \cdot \hat{\mathbf{n}}_i) q_j^{(k-1)}. \end{aligned} \tag{3.60}$$

Finally, the equation for the new charge values, Eq. 3.53, becomes

$$\begin{aligned} q_i^{(k)} &= \sigma_i^{(k)} \Delta S_i \\ &= P_B \Delta S_i \mathbf{E}_i^{(0)} \cdot \hat{\mathbf{n}}_i + \sum_{j=1,m;\, j\neq i} P_B \Delta S_i (\mathbf{A}_{ij} \cdot \hat{\mathbf{n}}_i) q_j^{(k-1)} \\ &= q_i^{(0)} + \sum_{j=1,m;\, j\neq i} B_{ij} q_j^{(k-1)}, \end{aligned} \tag{3.61}$$

where

$$B_{ij} = P_B \Delta S_i (\mathbf{A}_{ij} \cdot \hat{\mathbf{n}}_i). \tag{3.62}$$

B_{ij} is the matrix of interaction values, and Eq. 3.61 is the calculation of new charge values from the old with a matrix multiplication and a vector addition, as promised.

3.5 Curvature Compensation

The iterative algorithm relies on the assumption the the surface charge sectors are flat, and therefore the surface charge on a sector does not affect

that sector's own polarization. This can be seen from Eq. 3.20. While the derivation of this equation is strictly only valid for infinitesimal areas of surface, the electric field from the surface charge on a finite but *flat* sector would be perpendicular to the normal all over the sector, the term $\mathbf{E}_{\text{ex}} \cdot \hat{\mathbf{n}}$ would be zero, and there would be no contribution to surface charge density due to surface charge elsewhere on the sector.

Unfortunately the finite sectors that tile the boundary are not flat. They are curved where the boundary is curved, and this must inevitably result in inaccuracy in the calculations. The smaller the sectors, the better they approximate the ideal of flat and infinitesimal areas of surface. It should be possible to reduce the error to any desired level simply by making the sectors small enough. However, the time taken by the iterative algorithm is proportional to the square of the number of sectors, as is the memory required if pre-calculation is used. The number of sectors is proportional to the inverse square of the sector dimensions, so the computer resources required to run the algorithm depend on the inverse fourth power of the sector dimensions. Halving the spacing between sectors results in a sixteen-fold increase in the resources required. Obviously there is a practical limit to the reduction of errors by making the sectors smaller.

We use a method of compensating for curved sectors by incorporating an estimate of self interaction into the polarizability of each sector. We assume that the charge density σ is constant across the sector, and that the electric field $\mathbf{E}$ and normal $\hat{\mathbf{n}}$ at the center of the sector are representative of the whole sector. Including the self interaction, Eq. 3.20 can be written as

$$\begin{aligned} \sigma &= P_B(\mathbf{E}_{\text{ex}} + \mathbf{E}_{\text{self}}) \cdot \hat{\mathbf{n}}, \\ &= \sigma_{\text{ex}} + \sigma_{\text{self}}, \end{aligned} \tag{3.63}$$

where $\mathbf{E}_{\text{ex}}$ is the external electric field due to other sectors and fixed charges, and $\mathbf{E}_{\text{self}}$ arises from the self interaction of other points within the sector. The charge densities σ_{ex} and σ_{self} are associated with the external field and self interaction, respectively. Since we assume that the charge density is constant across the sector, σ_{self} is directly proportional to σ, that is

$$\sigma_{\text{self}} = Q\sigma, \tag{3.64}$$

where the constant of proportionality Q depends only on the shape and size of the sector and the polarizability of the boundary, but not on the external field. Using this relation in Eq. 3.63, we obtain for the corrected charge density

$$\begin{aligned} \sigma &= \sigma_{\text{ex}} + Q\sigma, \\ &= \frac{1}{1-Q}\sigma_{\text{ex}}, \\ &= \frac{P_B}{1-Q}\mathbf{E}_{\text{ex}} \cdot \hat{\mathbf{n}}. \end{aligned} \tag{3.65}$$

By pre-calculating Q and using Eq. 3.65 in place of (3.20) in the iterations, we can compensate for curved sectors without modifying the iterative algorithm.

Towards this end, we first express Q in terms of $\mathbf{E}_{\text{self}}$ using Eqs. 3.63 and 3.64

$$Q = \frac{P_B \mathbf{E}_{\text{self}} \cdot \hat{\mathbf{n}}}{\sigma} \,. \tag{3.66}$$

With the assumption of constant charge density σ in the sector, $\mathbf{E}_{\text{self}}$ depends only on the geometry of the sector and is given by the surface integral

$$\mathbf{E}_{\text{self}} = \frac{\sigma}{4\pi\epsilon_0} \int_S \frac{\delta\mathbf{R}}{|\delta\mathbf{R}|^3}\, dA, \tag{3.67}$$

where $\delta\mathbf{R}$ is a vector from the center of the sector to an arbitrary point on the sector, and the surface area covers the whole sector. Substituting Eq. 3.67 into 3.66, we obtain the desired expression for Q

$$Q = \frac{P_B}{4\pi\epsilon_0} \int_S \frac{\delta\mathbf{R} \cdot \hat{\mathbf{n}}}{|\delta\mathbf{R}|^3}\, dA. \tag{3.68}$$

To make further progress, we describe the sector as a parametric surface in variables (t, u) with the center at $\mathbf{R}_0 = \mathbf{R}(t_0, u_0)$ and the distance from the center given by $\delta\mathbf{R} = \mathbf{R}(t, u) - \mathbf{R}_0$. Since the surface dimensions are small, we can Taylor expand $\delta\mathbf{R}$ around $\mathbf{R}_0$ as

$$\delta\mathbf{R} = \mathbf{R}_{t,0}\, \delta t + \mathbf{R}_{u,0}\, \delta u + \frac{1}{2}\mathbf{R}_{tt,0}\, \delta t^2 + \frac{1}{2}\mathbf{R}_{uu,0}\, \delta u^2 + \mathbf{R}_{tu,0}\, \delta t\, \delta u + \ldots \tag{3.69}$$

where $\delta t = t - t_0$, $\delta u = u - u_0$ and the subscripts denote derivatives of $\mathbf{R}(t, u)$ at (t_0, u_0), that is

$$\mathbf{R}_{t,0} = \left.\frac{\partial\mathbf{R}}{\partial t}\right|_{t_0,u_0}, \quad \mathbf{R}_{tt,0} = \left.\frac{\partial^2\mathbf{R}}{\partial t^2}\right|_{t_0,u_0}, \quad \mathbf{R}_{tu,0} = \left.\frac{\partial^2\mathbf{R}}{\partial t \partial u}\right|_{t_0,u_0}, \quad \text{etc.} \tag{3.70}$$

Noting that $\hat{\mathbf{n}} \propto \mathbf{R}_{t,0} \times \mathbf{R}_{u,0}$, we obtain for the length and projection of $\delta\mathbf{R}$ to lowest order

$$\begin{aligned} |\delta\mathbf{R}|^2 &= |\mathbf{R}_{t,0}|^2\, \delta t^2 + |\mathbf{R}_{u,0}|^2\, \delta\theta^2 + \mathbf{R}_{t,0} \cdot \mathbf{R}_{u,0}\, \delta t\, \delta u \\ \delta\mathbf{R} \cdot \hat{\mathbf{n}} &= \frac{1}{2}\mathbf{R}_{tt,0} \cdot \hat{\mathbf{n}}\, \delta t^2 + \frac{1}{2}\mathbf{R}_{uu,0} \cdot \hat{\mathbf{n}}\, \delta u^2 + \mathbf{R}_{tu,0} \cdot \hat{\mathbf{n}}\, \delta t \delta u. \end{aligned} \tag{3.71}$$

There are no first order terms in $\delta\mathbf{R} \cdot \hat{\mathbf{n}}$, indicating absence of self-interaction when the sector is flat. The second order terms take into account deviation from a flat surface with constant curvatures in the t and u directions.

Our boundaries are all cylindrically symmetric, so we use cylindrical coordinates $r(t)$, $z(t)$, and θ to parameterize the surface. Then the sector becomes part of a generalized cylinder

$$\mathbf{R}(t, \theta) = r(t) \cos\theta\, \mathbf{i} + r(t) \sin\theta\, \mathbf{j} + z(t)\, \mathbf{k} \,. \tag{3.72}$$

Using a cylindrically symmetric dielectric boundary does not restrict the whole system to cylindrical symmetry; permanent charges such as ions can be arranged arbitrarily in three dimensional space. This approach can also be used for boundaries that are not cylindrically symmetric, although the formulas will be different and more complex. The partial derivatives of $\mathbf{R}(t,\theta)$ defined in Eq. 3.70 are given by

$$\begin{aligned}
\mathbf{R}_{t,0} &= r_0' \cos\theta_0\,\mathbf{i} + r_0' \sin\theta_0\,\mathbf{j} + z_0'\,\mathbf{k},\\
\mathbf{R}_{\theta,0} &= -r_0 \sin\theta_0\,\mathbf{i} + r_0 \cos\theta_0\,\mathbf{j},\\
\mathbf{R}_{tt,0} &= r_0'' \cos\theta_0\,\mathbf{i} + r_0'' \sin\theta_0\,\mathbf{j} + z_0''\,\mathbf{k},\\
\mathbf{R}_{\theta\theta,0} &= -r_0 \cos\theta_0\,\mathbf{i} - r_0 \sin\theta_0\,\mathbf{j},\\
\mathbf{R}_{t\theta,0} &= -r_0' \sin\theta_0\,\mathbf{i} + r_0' \cos\theta_0\,\mathbf{j}.
\end{aligned} \tag{3.73}$$

where $r_0 = r(t_0)$, $z_0 = z(t_0)$, and primes indicate derivative with respect to t. The normal $\hat{\mathbf{n}}$ at $\mathbf{R}_0$ can be found by taking the cross product of the unit tangents

$$\begin{aligned}
\hat{\mathbf{n}} &= \frac{\mathbf{R}_{t,0}}{|\mathbf{R}_{t,0}|} \times \frac{\mathbf{R}_{\theta,0}}{|\mathbf{R}_{\theta,0}|},\\
&= \frac{1}{\gamma_0}(r_0' \cos\theta_0\,\mathbf{i} + r_0' \cos\theta_0\,\mathbf{j} + z_0'\,\mathbf{k}) \times (-\sin\theta_0\,\mathbf{i} + \cos\theta_0\,\mathbf{j}),\\
&= \frac{1}{\gamma_0}(-z_0' \cos\theta_0\,\mathbf{i} - z_0' \sin\theta_0\,\mathbf{j} + r_0'\,\mathbf{k}),
\end{aligned} \tag{3.74}$$

where

$$\gamma_0 = \sqrt{r_0'^2 + z_0'^2}. \tag{3.75}$$

Substituting Eqs. 3.73 and 3.74 into (3.71) gives

$$\begin{aligned}
|\delta\mathbf{R}|^2 &= \gamma_0^2\,\delta t^2 + r_0^2\,\delta\theta^2,\\
\delta\mathbf{R}\cdot\hat{\mathbf{n}} &= \frac{1}{2\gamma_0}\left[(r_0' z_0'' - r_0'' z_0')\,\delta t^2 + r_0 z_0'\,\delta\theta^2\right].
\end{aligned} \tag{3.76}$$

The differential area dA is the product of the differential path lengths in the t and θ directions given by

$$\begin{aligned}
dA &= |\mathbf{R}_{t,0}||\mathbf{R}_{\theta,0}|\,dt\,d\theta,\\
&= \gamma_0 r_0\,dt\,d\theta.
\end{aligned} \tag{3.77}$$

Substituting Eqs. 3.76 and (3.77) into the integral (3.68) gives

$$Q = \frac{P_B}{4\pi\epsilon_0}\frac{1}{2\gamma_0}\int_{\theta_0-\Delta\theta}^{\theta_0+\Delta\theta}\int_{t_0-\Delta t}^{t_0+\Delta t}\frac{(r_0' z_0'' - r_0'' z_0')\,\delta t^2 + r_0 z_0'\,\delta\theta^2}{(\gamma_0^2\delta t^2 + r_0^2\delta\theta^2)^{3/2}}\gamma_0 r_0\,dt\,d\theta\ . \tag{3.78}$$

By making the substitutions $t \to t + t_0$ and $\theta \to \theta + \theta_0$, this becomes

$$Q = \frac{P_B r_0}{8\pi\epsilon_0}\int_{-\Delta\theta}^{\Delta\theta}\int_{-\Delta t}^{\Delta t}\frac{(r_0' z_0'' - r_0'' z_0')\,t^2 + r_0 z_0'\,\theta^2}{(\gamma_0^2 t^2 + r_0^2\theta^2)^{3/2}}\,dt\,d\theta, \tag{3.79}$$

which can be integrated to yield

$$Q = \frac{P_B}{2\pi\epsilon_0}\left[\frac{r_0}{\gamma_0^3}(r_0' z_0'' - r_0'' z_0')\Delta\theta \sinh^{-1}\left(\frac{\gamma_0\Delta t}{r_0\Delta\theta}\right) + \frac{z_0'}{r_0}\Delta t \sinh^{-1}\left(\frac{r_0\Delta\theta}{\gamma_0\Delta t}\right)\right]. \tag{3.80}$$

3.6 Testing and Performance

Our main way of verifying both the iterative and analytical methods is by comparing the two solutions for the same boundary. Since these two methods use completely different algorithms their close agreement is good evidence that both are working correctly. This testing is described in the following chapter, after the description of the analytical method. There are, however, some tests that can be done using the iterative method alone, and they are described here. The tests are performed for a catenary channel, as shown in Fig 3.1. They are done for three different sector spacings: high resolution (15500 sectors, $\lambda = 1.0$), medium resolution (6900 sectors, $\lambda = 1.5$), and low resolution (3900 sectors, $\lambda = 2.0$). The convergence of the solution as the number of sectors increases gives an indication of the accuracy of the calculations.

The first set of tests is for an ion passing through the centre of the channel. This is the most critical area of the solution. Conductance largely depends on the energy barriers and wells in the constricted part of the channel, and repulsion from induced charges tends to keep the ions away from the protein walls. The tests are for a line through the centre of the channel, from $z = -50$ Å to $z = 50$ Å with 1 Å intervals between positions. They are done at low, medium, and high resolution, first with curvature compensation turned off, then with it on. Fig. 3.6A shows the potential energy profiles. The profiles produced without curvature compensation can be seen converging towards the profile produced with curvature compensation. Only the medium resolution profile is shown with curvature compensation on, since the traces overlap. Fig. 3.6B shows the potential energy at $z = 0$ for the six tests, and extrapolates to allow estimation of the potential energy as sector spacing goes towards zero. The improvement in accuracy due to the curvature compensation algorithm is evident from this figure: the error at $\lambda = 1.5$ can be estimated at 9% without curvature compensation, but only 1% with. The slow convergence of the method without curvature compensation means that λ would have to be reduced to something like 0.1 to produce accuracy similar to that with curvature compensation. This would require an impractical number of sectors: curvature compensation is necessary to make the algorithm sufficiently accurate with a realistic number of sectors.

The second set of tests is for an ion close to the protein wall in the neck region of the channel. This is the region where an ion is most likely

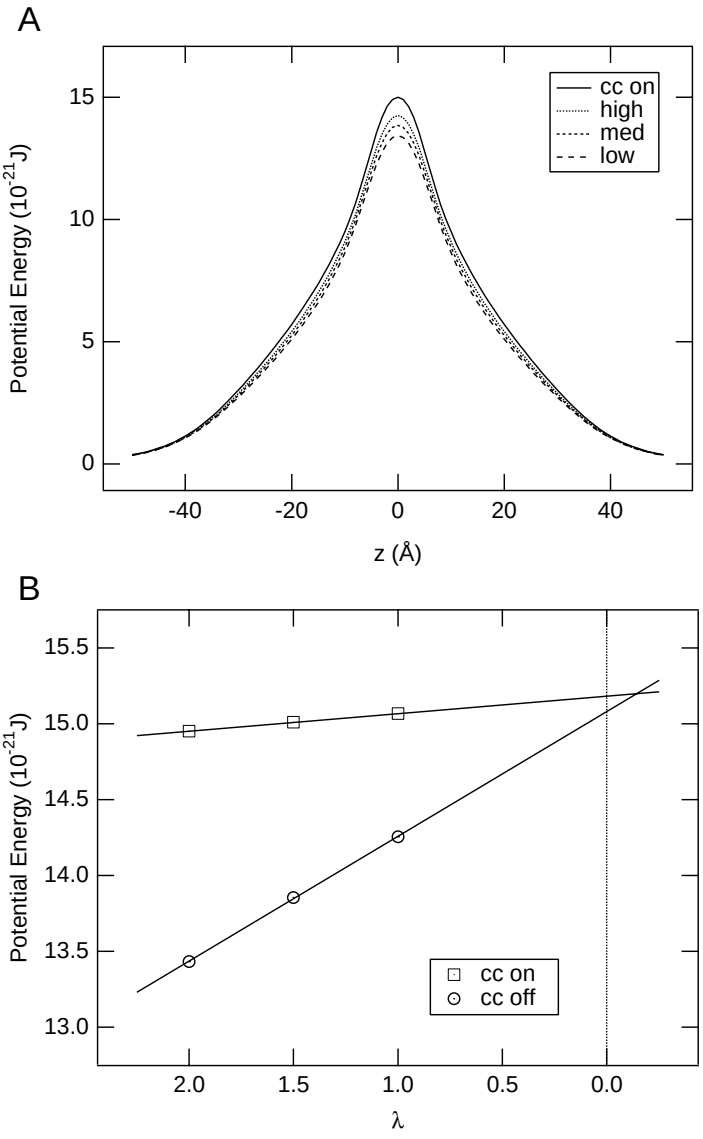

Figure 3.6: Centreline potential energy profiles. Graph A shows the potential profiles for ions traversing the centreline of the channel, at low, medium, and high resolution with curvature compensation off, and at medium resolution with curvature compensation on. For clarity only one profile is show with curvature compensation on, since the traces overlap. Graph B show the convergence of the calculated potential energy as λ is reduced towards zero. The points were calculated on the centreline with $z = 0$.

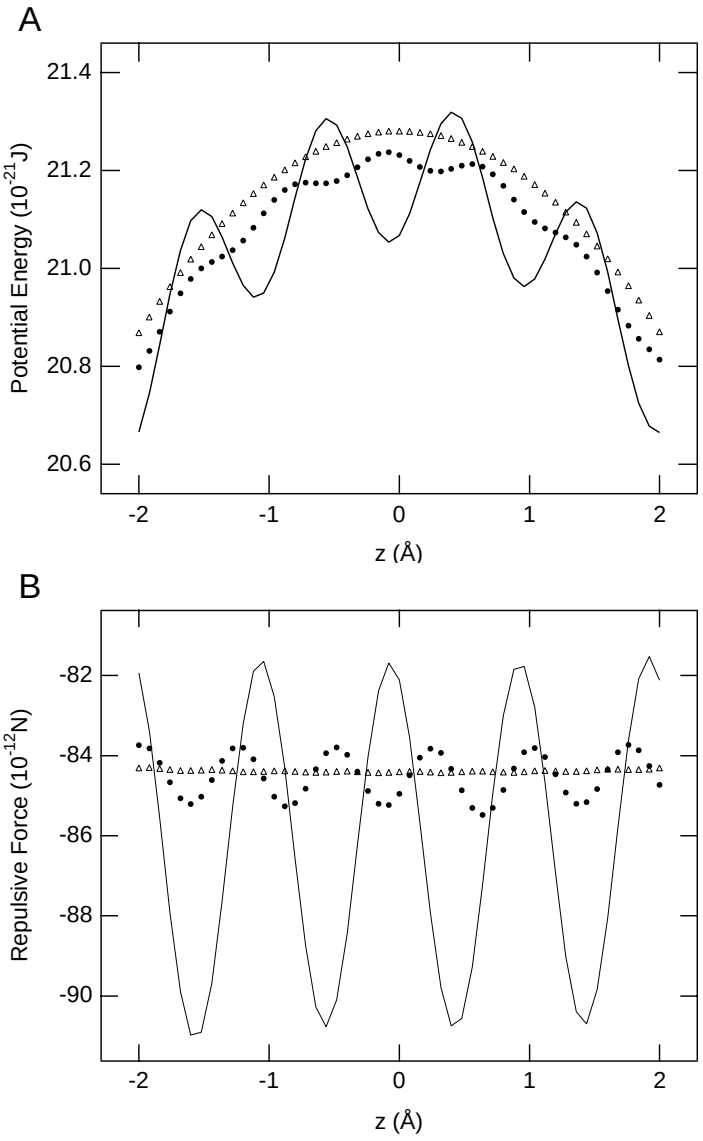

Figure 3.7: Offset potential energy and force profiles. These graphs are for an ion track in the neck region of the channel ($z = -2$ to 2 Å), offset from the centreline by 3 Å and so only 1 Å from the boundary. Graph A shows the potential energy profile at low (solid line), medium (filled circles), and high (open triangles) resolution. The finite spacing of the boundary sectors creates bumps in the traces, especially at low resolution. The fractional errors are, however, quite small: note the expanded vertical scale. Graph B show the force profile at low (solid line), medium (filled circles), and high (open triangles) resolution. This is the force in the x direction: the graph shows the repulsive force from the nearby boundary. The vertical scale is again expanded, but the errors are larger (around 10% at low resolution). The text explains why such errors in the repulsive force are acceptable in the vestibules. This figure shows that in the neck region the error is reasonable ($< 2\%$) at medium resolution.

Pre-Calculation	Sectors	Memory	Number of Iterations	Time per Iteration	Time per Position
OFF	3900	24 MB	26	1.7 s	44 s
OFF	6900	24 MB	24	5.5 s	132 s
OFF	15500	24 MB	36	29.3 s	1055 s
ON	3900	80 MB	26	28 ms	0.7 s
ON	6900	200 MB	24	89 ms	2.1 s
ON	15500	920 MB	36	444 ms	16.0 s

Table 3.1: Performance of the Iterative Method

to approach the wall. Curvature compensation is turned on for this set of tests, but errors occur because the distance from the ion to the boundary is comparable to the sector spacing. The tests are for a line from $z = -2$ Å to $z = 2$ Å, but offset 3 Å from the centreline in the x direction, and so only 1 Å from the boundary. This is effectively in contact with the wall, since inorganic cations have radii of around 1 Å. Fig. 3.7A shows the potential energy profiles at low, medium, and high resolutions. The sector spacing in the neck is 0.5 Å for high resolution, 0.75 Å for medium, and 1.0 Å for low. The effect of this finite sector spacing can be seen in the figure. When the ion is 2× the sector spacing from the boundary (high resolution) the profile is reasonably smooth, but at 1.33× spacing the profile gets bumpy, and the amount of variation increases at 1× spacing. The bumps in the profiles make it impossible to extrapolate to zero spacing, but the maximum variation of the medium resolution profile from the high resolution profile is less than 0.5% of the potential energy (note the expanded vertical scale of the graph). Fig. 3.7B shows the force in the x direction: the repulsive force away from the wall. The variations in this force are again quite reasonable, at around 1% at medium resolution. At the vestibule wall, where the sector spacing is larger, the variation is more like that of the low resolution profile, and errors in the repulsive force can be around 10%. These errors in the force are acceptable, however, for two reasons. Firstly, ions tend not to approach the protein walls this closely, because of the very repulsive force whose accuracy is in doubt. Secondly, repulsion from the walls at such close ranges depends on detailed interaction with the ion's first hydration shell, which is not accurately modeled by the macroscopic theory of electrostatics. There is little point in going to great effort to calculate to 1% or 2% accuracy where simplifications in the theory might be leading to an much larger error.

The performance of the iterative method on the VPP is outlined in table 3.1. With the pre-calculation algorithm turned off the memory use is a constant 24 MB. In fact there is a memory use proportional to the number

of sectors, but it is insignificant compared to the approximately 20 MB overhead of running any program on this machine: the VPP allocates memory in 8 MB blocks, so the gradually increasing memory use does not appear in the table. Memory use with pre-calculation turned on is proportional to the square of the number of sectors. The constant of proportionality is 4 bytes, for one single precision real number per matrix element. The time taken per iteration is also proportional to the square of the number of sectors, but with pre-calculation turned on the algorithm is 60 times faster. The iterative method achieves 99% vectorization with or without pre-calculation, so this speedup is due to reducing the number of calculations, and is not a reflection of the VPP's poor scalar performance. However, the speedup may not be as large on machines with less efficient memory architectures, and if the algorithm is to run efficiently there has to be enough real memory to hold the pre-calculation matrix. The number of iterations taken for the algorithm to converge varies with the spacing of the points and the positions of ions and fixed charges: it is generally around 30. The results in the table are for a single ion in the neck region of a catenary channel. Even with pre-calculation it takes 2.1 s for a single solution at medium resolution. This is fast enough to calculate energy profiles, but it is far too slow for a BD simulation. A typical run of 1,000,000 steps would take over 500 h of CPU time, more than one run would be needed for an accurate conductance result, and this is only for one point on a graph. A faster algorithm is needed.

Chapter 4

Analytical Method

As mentioned in the introduction to chapter 3, there are two approaches to solving Poisson's equation for a channel boundary: mathematical analysis or an iterative algorithm. An analytical solution is usually preferred, if available, because it is a more compact and elegant representation, and can act as an aid to intuition. However, analytical solutions to Poisson's equation are only possible for a limited set of boundary geometries, only one of which can be used to represent a channel: the toroidal boundary described in this chapter. This chapter describes our analytical solution to Poisson's equation for a toroidal boundary, followed by the algorithm we use to calculate this solution rapidly on a vector architecture machine.

4.1 Analytical Solution

4.1.1 Toroidal Coordinates

The system of toroidal coordinates (μ, η, ϕ) is illustrated in Fig. 4.1. The coordinate μ is defined as $\log(PL'/PL)$, where L and L' are the limiting points of a set of coaxial circles. The constant $\mu = \mu_1$ defines the surface of a torus. When circles of progressively increasing radii are drawn (dotted lines in Fig. 4.1), their centers move out on the x-axis towards infinity. Thus, as μ decreases progressively from ∞ to 0, the circles grow from the point at L (zero radius) to the z axis (infinite radius with center at infinity). The coordinate η is defined by the angle LPL' and has the range $[0, 2\pi]$. For a given μ, η traces a circle of a fixed radius as it changes from 0 to 2π, as indicated in Fig. 4.1. Finally, ϕ is the usual azimuthal angle about the symmetry axis z with the range $[0, 2\pi]$. As a circle is revolved around the z-axis by $360^{\,o}$ counter-clockwise, a toroidal shape is generated. A point anywhere inside and outside of the torus, as well as on its surface, can be represented by μ, η and ϕ.

The toroidal coordinates are related to the Cartesian ones through the

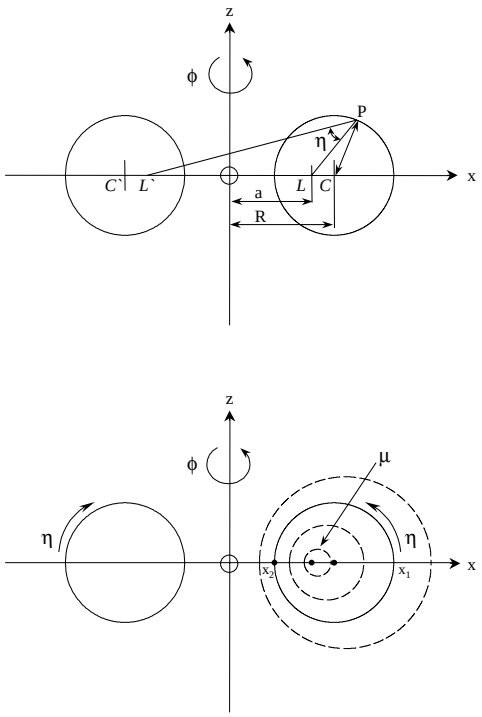

Figure 4.1: Toroidal coordinate system. A torus is generated by rotating the two circles shown in the upper panel by 180^o along the z-axis. A point P anywhere in space can be defined by (μ, η, ϕ). The coordinate μ describes a ring of circles. The radius of the circle decreases progressively and its center moves in from ∞ to point L on the x-axis as μ increases from 0 to ∞. For a given μ, η traces a circle of fixed radius as it goes from 0 to 2π, with $\eta = 0$ furthest from the z-axis, and $\eta = \pi$ nearest. The coordinate ϕ is the azimuthal angle about the z-axis.

following set of equations [52]:

$$x = \frac{a \sinh\mu \cos\phi}{\cosh\mu - \cos\eta}, \quad y = \frac{a \sinh\mu \sin\phi}{\cosh\mu - \cos\eta}, \quad z = \frac{a \sin\eta}{\cosh\mu - \cos\eta}. \tag{4.1}$$

The inverse relations, which are needed to transform the positions of the charges and field points from Cartesian to toroidal coordinates, are given by

$$\mu = \tanh^{-1} \frac{2a\sqrt{x^2+y^2}}{x^2+y^2+z^2+a^2} \tag{4.2}$$

$$\eta = \tan^{-1} \frac{2az}{x^2+y^2+z^2-a^2} \tag{4.3}$$

$$\phi = \tan^{-1} \frac{y}{x}. \tag{4.4}$$

In the x-z plane, the circle describing the toroidal surface will intersect the positive x-axis twice, x_1 at $\eta = 0$ and x_2 at $\eta = \pi$. Thus, the radius r of the torus is related to the toroidal coordinates by the expression

$$\begin{aligned} r &= \frac{1}{2}(x_1 - x_2) \\ &= \frac{1}{2}\left(\frac{a \sinh\mu_1}{\cosh\mu_1 - 1} - \frac{a \sinh\mu_1}{\cosh\mu_1 + 1}\right) \\ &= \frac{a \sinh\mu_1}{\cosh^2\mu_1 - 1} \\ &= \frac{a}{\sinh\mu_1}. \end{aligned} \tag{4.5}$$

Similarly, the distance from the origin to the centre of the torus R can be expressed in terms of the toroidal coordinates as

$$\begin{aligned} R &= x_2 + \frac{x_1 - x_2}{2} \\ &= a\left(\frac{\sinh\mu_1}{\cosh\mu_1 + 1} + \frac{1}{\sinh\mu_1}\right) \\ &= a\left(\frac{\cosh\mu_1}{\sinh\mu_1}\right) \\ &= a \coth\mu_1. \end{aligned} \tag{4.6}$$

The inverse relations are

$$\begin{aligned} a &= \sqrt{R^2 - r^2} \\ \mu_1 &= \cosh^{-1}\frac{R}{r}. \end{aligned} \tag{4.7}$$

Thus, as η changes from 0 to 2π, constant μ_1 follows a circle of the minor radius, $r = a/\sinh\mu_1$, centered at the major radius $R = a\coth\mu_1$. By

rotating the two circles around the perpendicular z-axis, the full toroidal boundary is generated.

We note that the ratio between the minor and major radii, $r/R = 1/\cosh\mu_1$ is independent of a and determines the diameter of the constricted region of the model channel. For $\mu = 0$, both r and R are infinite and the circle becomes the z-axis. In the opposite limit, $\mu = \infty$, the major and minor radii coincide, i.e. $R = a$ and $r = 0$, and the toroid becomes a ring of radius a around the z-axis.

4.1.2 Solutions of Laplace's and Poisson's Equations

Solution of Laplace's equation in toroidal coordinates is given in terms of the trigonometric functions for η and ϕ, and the toroidal harmonics (Legendre functions of half-order) $P^m_{n-1/2}(\cosh\mu)$, $Q^m_{n-1/2}(\cosh\mu)$. The most general solution can be written as

$$\varphi = f(\mu,\eta)\sum_{n=0}^{\infty}\sum_{m=0}^{\infty}\Big[A_{nm}Q^m_{n-1/2}(\cosh\mu) + B_{nm}P^m_{n-1/2}(\cosh\mu)\Big] \times \cos n(\eta-\eta_{nm})\cos m(\phi-\phi_{nm}), \tag{4.8}$$

where

$$f(\mu,\eta) = \sqrt{\cosh\mu - \cos\eta} \tag{4.9}$$

and the coefficients $A_{nm}, B_{nm}, \eta_{nm}, \phi_{nm}$ are to be determined from boundary conditions.

The potential due to a point charge q at $\mathbf{r}_0 = (\mu_0,\eta_0,\phi_0)$ is given in reference [52] as:

$$\begin{aligned}\frac{q}{|\mathbf{r}-\mathbf{r}_0|} &= \frac{q}{\pi a}f(\mu,\eta)f(\mu_0,\eta_0)\sum_{n=0}^{\infty}\sum_{m=0}^{\infty}(2-\delta_{n0})(2-\delta_{m0})\frac{\Gamma(n-m+1/2)}{\Gamma(n+m+1/2)} \\ &\quad\times\cos n(\eta-\eta_0)\cos m(\phi-\phi_0) \\ &\quad\times\begin{cases} P^m_{n-1/2}(\cosh\mu)Q^m_{n-1/2}(\cosh\mu_0), & \mu<\mu_0, \\ Q^m_{n-1/2}(\cosh\mu)P^m_{n-1/2}(\cosh\mu_0), & \mu>\mu_0. \end{cases}\end{aligned} \tag{4.10}$$

The change in the μ solutions reflects the fact that $P^m_{n-1/2}$ diverges as $\mu\to\infty$ and $Q^m_{n-1/2}$ diverges as $\mu\to 0$. Solution of Poisson's equation for the system of a point charge outside the toroidal boundary $\mu = \mu_1 > \mu_0$, with dielectric constants ε_1 outside and ε_2 inside the torus, can be found by superposing the potentials in Eqs. 4.8 and 4.10. As usual in such boundary value problems, the ϕ solutions are decoupled, and the phases ϕ_{nm} in Eq. 4.8 must be coherent with ϕ_0, so that $\phi_{nm} = \phi_0$ for all n, m. The same argument, however, does not hold for the η solutions. Due to the square root factors f (Eq. 4.9), there is coupling between different coefficients, and the phase factors η_{nm} are not necessarily coherent with η_0. This is a distinctive feature of the toroidal coordinates, and complicates solutions of electrostatic

problems in comparison with other coordinate systems. With these caveats, the superposed potential can be written as

$$\begin{aligned}
\varphi_{in} &= f(\mu,\eta)\sum_{n=-\infty}^{\infty}\sum_{m=0}^{\infty} A_{nm}Q^m_{n-1/2}(\cosh\mu)\exp[in(\eta-\eta'_{nm})]\cos m(\phi-\phi_0),\\
\varphi_{out} &= f(\mu,\eta)\sum_{n=-\infty}^{\infty}\sum_{m=0}^{\infty}\Big[B_{nm}P^m_{n-1/2}(\cosh\mu)\exp[in(\eta-\eta''_{nm})]\\
&\qquad + C_{nm}Q^m_{n-1/2}(\cosh\mu)\exp[in(\eta-\eta_0)]\Big]\cos m(\phi-\phi_0), \quad (4.11)
\end{aligned}$$

where

$$C_{nm} = \frac{1}{4\pi\varepsilon_0\varepsilon_1}\frac{q}{\pi a}f(\mu_0,\eta_0)(2-\delta_{m0})\frac{\Gamma(n-m+1/2)}{\Gamma(n+m+1/2)}P^m_{n-1/2}(\cosh\mu_0), \quad (4.12)$$

are constant coefficients. In Eq. 4.11, we used $\mu > \mu_0$ solution for the point charge (Eq. 4.10) as it is the appropriate one for the boundary at $\mu = \mu_1$. Also, we replaced the cosines with exponentials for the η solutions because it simplifies the boundary matching.

Applying the usual boundary conditions at $\mu = \mu_1$

$$\varphi_{in} = \varphi_{out}, \quad \varepsilon_2\frac{\partial\varphi_{in}}{\partial(\cosh\mu)} = \varepsilon_1\frac{\partial\varphi_{out}}{\partial(\cosh\mu)} \quad (4.13)$$

we obtain the following equations for every m:

$$\begin{aligned}
&\sum_{n=-\infty}^{\infty} A_{nm}Q\exp[in(\eta-\eta'_{nm})]\\
&\qquad = \sum_{n=-\infty}^{\infty}\Big[B_{nm}P\exp[in(\eta-\eta''_{nm})]\\
&\qquad\qquad + C_{nm}Q\exp[in(\eta-\eta_0)]\Big], \quad (4.14)
\end{aligned}$$

and

$$\begin{aligned}
&\varepsilon_2\sum_{n=-\infty}^{\infty} A_{nm}(fQ'+f'Q)\exp[in(\eta-\eta'_{nm})]\\
&\qquad = \varepsilon_1\sum_{n=-\infty}^{\infty}\Big[B_{nm}(fP'+f'P)\exp[in(\eta-\eta''_{nm})]\\
&\qquad\qquad + C_{nm}(fQ'+f'Q)\exp[in(\eta-\eta_0)]\Big]. \quad (4.15)
\end{aligned}$$

Here we have introduced the compact notation for the constants, $P = P^m_{n-1/2}(\cosh\mu_1)$, $Q = Q^m_{n-1/2}(\cosh\mu_1)$ and $f = f(\mu_1,\eta)$. Similarly, the primes over P, Q and f denote derivatives with respect to $\cosh\mu$ evaluated

at $\mu = \mu_1$. These equations can be further simplified by introducing the complex coefficients:

$$\begin{aligned} A'_{nm} &= A_{nm}\exp[-in\eta'_{nm}], \\ B'_{nm} &= B_{nm}\exp[-in\eta''_{nm}], \\ C'_{nm} &= C_{nm}\exp[-in\eta_0]. \end{aligned} \tag{4.16}$$

Substituting the above coefficients in Eqs. 4.14 and 4.15, we obtain

$$\sum_{n=-\infty}^{\infty} A'_{nm}Q\exp[in\eta] = \sum_{n=-\infty}^{\infty}\Big[B'_{nm}P + C'_{nm}Q\Big]\exp[in\eta], \tag{4.17}$$

and

$$\begin{aligned} \varepsilon_2 \sum_{n=-\infty}^{\infty} & A'_{nm}(fQ' + f'Q)\exp[in\eta] \\ &= \varepsilon_1 \sum_{n=-\infty}^{\infty}\Big[B'_{nm}(fP' + f'P)\exp[in\eta] \\ &\qquad + C'_{nm}(fQ' + f'Q)\exp[in\eta]\Big]. \end{aligned} \tag{4.18}$$

Eq. 4.17 now holds for each n, and hence we can solve for B'_{nm} in terms of A'_{nm}

$$B'_{nm} = (A'_{nm} - C'_{nm})Q/P. \tag{4.19}$$

Substituting B'_{nm} in Eq. 4.18 and collecting similar terms gives

$$\begin{aligned} \sum_{n=-\infty}^{\infty} & A'_{nm}\Big[\varepsilon_2(fQ' + f'Q) - \varepsilon_1(fP' + f'P)Q/P\Big]\exp[in\eta] \\ &= \varepsilon_1 \sum_{n=-\infty}^{\infty} C'_{nm}f(Q' - P'Q/P)\exp[in\eta]. \end{aligned} \tag{4.20}$$

Using $f' = 1/2f$ and substituting back $f^2 = \cosh\mu_1 - \cos\eta$, Eq. 4.20 can be put in the form

$$\begin{aligned} 2(\cosh\mu_1 - \cos\eta) \sum_{n=-\infty}^{\infty} & A'_{nm}(\varepsilon_2 Q' - \varepsilon_1 P'Q/P)\exp[in\eta] \\ &\qquad + (\varepsilon_2 - \varepsilon_1)\sum_{n=-\infty}^{\infty} A'_{nm}Q\exp[in\eta] \\ = 2\varepsilon_1(\cosh\mu_1 - \cos\eta) &\sum_{n=-\infty}^{\infty} C'_{nm}(Q' - P'Q/P)\exp[in\eta]. \end{aligned} \tag{4.21}$$

Notice that the $\cos\eta$ factors in the front leads to coupling of neighbouring coefficients, so that Eq. 4.21 cannot be solved trivially as typically encountered

in boundary value problems involving spherical or cylindrical coordinate systems. Fourier analysis of the series in Eq. 4.21 in η, (i.e. multiplying by either $\sin n'\eta$ or $\cos n'\eta$ and integrating from $0 - 2\pi$), gives

$$\sum_{n=-\infty}^{\infty} \Big[\Big(2\cosh\mu_1(\varepsilon_2 Q' - \varepsilon_1 P'Q/P) + (\varepsilon_2 - \varepsilon_1)Q \Big)\delta_{n',n} - (\varepsilon_2 Q' - \varepsilon_1 P'Q/P)(\delta_{n',n+1} + \delta_{n',n-1}) \Big] A'_{nm} = \varepsilon_1 \sum_{n=-\infty}^{\infty} C'_{nm}(Q' - P'Q/P) \Big[2\cosh\mu_1 \delta_{n',n} - (\delta_{n',n+1} + \delta_{n',n-1}) \Big]. \quad (4.22)$$

Introducing further

$$\begin{aligned} E_n^m &= (\varepsilon_2 Q' - \varepsilon_1 P'Q/P) A'_{nm}, \\ q_n^m &= 2\cosh\mu_1 + \frac{(\varepsilon_2 - \varepsilon_1)Q}{\varepsilon_2 Q' - \varepsilon_1 P'Q/P}, \\ \lambda_n^m &= \varepsilon_1 (Q' - P'Q/P) C'_{nm}, \end{aligned} \quad (4.23)$$

we obtain the following second order difference equation for the coefficients E_n^m

$$E_{n+1}^m - q_n^m E_n^m + E_{n-1}^m = \lambda_{n+1}^m - 2\cosh\mu_1 \lambda_n^m + \lambda_{n-1}^m. \quad (4.24)$$

The real and imaginary parts of this equation must be satisfied separately leading to two difference equations which, through Eqs. 4.16 and 4.23, determine both the amplitude A_{nm} and the phase η'_{nm}. Eq. 4.24 also arises in the problem of a dielectric torus in a uniform electric field [46], and can be solved using techniques of the Green function.

4.1.3 Solution of the Difference Equation

Here we sketch the solution of the second order difference equation (Eq. 4.24). For convenience, we will suppress the superscript m, but the same equation, with different coefficients q_n^m and λ_n^m, has to be solved for each value of m. The Green function corresponding to Eq. 4.24 satisfies (see [46])

$$G_{n+1,N} - q_n G_{n,N} + G_{n-1,N} = \delta_{n,N+1} - 2\cosh\mu_1 \delta_{n,N} + \delta_{n,N-1}, \quad (4.25)$$

for each value of N. Here $\delta_{n,N}$ denotes Kronecker delta. Solutions of (Eq. 4.24) are then given by

$$E_n = \sum_{N=-\infty}^{\infty} G_{n,N} \lambda_N, \quad (4.26)$$

as can be verified by substituting Eq. 4.26 in Eq. 4.24 and using Eq. 4.25.

Construction of the Green function in Eq. 4.25 is conceptually similar to the familiar cases in electrostatics. One first finds the solutions of the homogeneous equation

$$G_{n+1,N} - q_n G_{n,N} + G_{n-1,N} = 0, \tag{4.27}$$

and then implements the "boundary conditions" implied in Eq. 4.25. The two independent solutions of Eq. 4.27 can be found from a study of its asymptotic form as $|n| \to \infty$. In that limit, $q \to 2\cosh\mu_1$, and the ratios $G_{n+1,N}/G_{n,N}$ for the solutions tend to $\exp(\pm\mu_1)$. The solutions of Eq. 4.27 with the correct asymptotics are given in terms of the continued fractions as (see, for details, [50])

$$\begin{aligned}
\frac{G_{n+1,N}}{G_{n,N}} &= \cfrac{1}{q_{n+1} - \cfrac{1}{q_{n+2} - \cfrac{1}{q_{n+3} - \cdots}}} \equiv \alpha_{n+1}, \\
\frac{G_{n-1,N}}{G_{n,N}} &= \cfrac{1}{q_{n-1} - \cfrac{1}{q_{n-2} - \cfrac{1}{q_{n-3} - \cdots}}} \equiv \beta_{n-1}.
\end{aligned} \tag{4.28}$$

Eq. 4.28 can be written as recursion relations among α_n and β_n

$$\alpha_n = \frac{1}{q_n - \alpha_{n+1}}, \quad \beta_n = \frac{1}{q_n - \beta_{n-1}}, \tag{4.29}$$

which provide a simple method for their calculation by iteration. From the symmetry properties of $P^m_{n-1/2}$, $Q^m_{n-1/2}$ and their derivatives (they remain invariant under $n \to -n$), it follows that $q_{-n} = q_n$ in Eq. 4.23. Using this fact in Eq. 4.29, it is seen that $\alpha_n = \beta_{-n}$, and therefore only one set of coefficients need to be calculated. Rewriting Eq. 4.28 as

$$\begin{aligned}
G_{n+1,N} &= \alpha_{n+1} G_{n,N}, \quad n \geq N+1, \\
G_{n-1,N} &= \beta_{n-1} G_{n,N}, \quad n \leq N-1,
\end{aligned} \tag{4.30}$$

$G_{n,N}$ can be determined from Eq. 4.30 recursively, once $G_{N+1,N}$ and $G_{N-1,N}$ are specified. To calculate these two quantities, we use the "boundary conditions" on Eq. 4.25 at $n = N-1, N, N+1$, which gives the following equations

$$\begin{aligned}
&(\beta_{N-2} - q_{N-1}) G_{N-1,N} + G_{N,N} = 1, \\
&G_{N-1,N} - q_N G_{N,N} + G_{N+1,N} = -2\cosh\mu_1, \\
&G_{N,N} + (\alpha_{N+2} - q_{N+1}) G_{N+1,N} = 1,
\end{aligned} \tag{4.31}$$

where we have substituted $G_{N-2,N} = \beta_{N-2} G_{N-1,N}$ and $G_{N+2,N} = \alpha_{N+2} G_{N+1,N}$ from Eq. 4.30. These equations can be further simplified by using $\beta_{N-2} - q_{N-1} = -1/\beta_{N-1}$ and $\alpha_{N+2} - q_{N+1} = -1/\alpha_{N+1}$, which follow from Eq. 4.29. Solution of the set of linear equations in Eq. 4.31 yields

$$\begin{aligned} G_{N-1,N} &= \frac{(2\cosh\mu_1 - q_N)\beta_{N-1}}{q_N - \alpha_{N+1} - \beta_{N-1}}, \\ G_{N,N} &= \frac{(2\cosh\mu_1 - \alpha_{N+1} - \beta_{N-1})}{q_N - \alpha_{N+1} - \beta_{N-1}}, \\ G_{N+1,N} &= \frac{(2\cosh\mu_1 - q_N)\alpha_{N+1}}{q_N - \alpha_{N+1} - \beta_{N-1}}. \end{aligned} \tag{4.32}$$

Substituting Eqs. 4.30 and 4.32 in Eq. 4.26, we finally obtain for the coefficients E_n

$$\begin{aligned} E_n = \sum_{N=-\infty}^{\infty} \frac{\lambda_N}{(q_N - \alpha_{N+1} - \beta_{N-1})} \Bigg\{ & (2\cosh\mu_1 - \alpha_{N+1} - \beta_{N-1})\delta_{n,N} \\ & + (2\cosh\mu_1 - q_N)\Big[\theta(n-N)\prod_{k=N+1}^{n}\alpha_k + \theta(N-n)\prod_{k=n}^{N-1}\beta_k\Big]\Bigg\} \end{aligned} \tag{4.33}$$

where $\theta(x)$ is the step function, *i.e.*, $\theta(x) = 1$ if $x > 0$ and 0 otherwise.

4.1.4 Application of External Electric Field

The solution for a uniform electric field $\mathcal{E}_0$, applied along the symmetry axis of the torus, follows the same lines as above but is much simpler [46]. Due to the axial symmetry, the potential is independent of the coordinate ϕ. Hence, the m-sums in Eq. 4.11 are suppressed. Further, there are no phase differences in the η solutions, *i.e.*, they are given by $\exp[in\eta]$ everywhere. The potential for a uniform field in toroidal coordinates is given by

$$\begin{aligned} \varphi_{ap} &= \mathcal{E}_0 z \\ &= \mathcal{E}_0 \frac{\sqrt{8}a}{i\pi} f(\mu,\eta) \sum_{n=-\infty}^{\infty} n Q_{n-1/2}(\cosh\mu)\exp[in\eta]. \end{aligned} \tag{4.34}$$

Superposing φ_{ap} with the free fields in Eq. 4.8, and applying the boundary conditions, one obtains again a second order difference equation as in Eq. 4.24 but without the m indices. The coefficients E_n and q_n are the same as in Eq. 4.23 and λ_n is modified to

$$\lambda_n = \varepsilon_1 (Q' - P'Q/P)\mathcal{E}_0 \frac{\sqrt{8}a}{\pi} n. \tag{4.35}$$

4.1.5 Calculation of Force and Potential Energy

The electric potential and field from multiple ions and an applied electric field are built up using the principle of superposition. Since we assume the dielectrics are linear, any number of permanent charges, as well as the applied field, can be included simply by adding together their solutions for the same dielectric boundary. The electric field and potential at the position of an ion is therefore the sum of that due to the other ions, the applied field, the surface charges induced by these, and the surface charges induced by that particular ion.

The force on the ion is simply the total field multiplied by the charge on the ion, but there is a subtlety in the calculation of the ion's potential energy. The potential energy due to the other ions, the applied field, and the charges they induce is the electric potential times the ion's charge. However, the potential energy due to the surface charges induced by the ion itself is only half the electric potential times the charge. This can be seen by using a Born charging process [10, 30]: that is by imagining the charge Q on the ion being built up as infinitesimal charges dq being brought in from infinity. While the electric potential due to the other ions remain the same throughout, that induced by the ion increases from zero to its full value Q as the charge is built up. This involves integrating $q\ dq$ from 0 to Q, hence the factor of one half. Our program takes account of this by calculating the total field and potential at the position of an ion, as well as the potential due only to the ion's interaction with the boundary. It then subtracts half of this self-potential from the total for the purpose of calculating the potential energy.

Fixed charges in the protein wall are included in the same way as ions. The only change is that they require a slightly different analytical solution, since they are inside the toroidal boundary, not outside. The form of Eq. 4.10 with $\mu = \mu_1 < \mu_0$ needs to be used, and corresponding changes need to be made for the rest of the solution.

4.2 Algorithm

The situation then, is that we have a toroidal boundary between media of different dielectric strengths, as well as a number of point charges, and we want to know the electric field and potential at a number of points of interest. This previous section describes the analytical solution to this problem. The resulting expression is a complicated hierarchy of infinite series, continued fractions, and associated Legendre functions. The question of how to implement the solution efficiently as a computer program remains. This section describes the algorithm.

The expression is evaluated from the bottom up, using a fixed number of terms for all of the series and continued fractions. The intermediate results

are stored in arrays as they are generated, and kept for possible reuse. The calculation is divided into three pieces: the boundary, the charges, and the potentials. Thus the calculations for the boundary do not have to be redone if the positions of the charges change, and the calculations for the charges do not have to be redone for each point of interest. Due to the fixed number of terms, the calculations for each charge and each potential are the same, and the algorithm can be easily vectorized.

The alternative top down approach is conceptually simpler, and allows better control of precision, as each potential can be summed until the desired accuracy has been reached and no further. It is hopelessly inefficient if implemented naively, however, as many quantities are repeatedly recalculated, and some of the recurrence relations do not run in the same direction as the algorithm. We attempted to overcome these problems by storing intermediate results and reusing them when available, but the top down algorithm does not generate intermediate results in a predictable order, and keeping track of them severely complicated the code, resulting in a slow and unreliable program. In addition, because each calculation was treated differently, the program was not vectorizable. The bottom up algorithm described here is far superior.

4.2.1 Legendre Functions

The Legendre Functions are calculated using the recurrence relations [1]

$$P^m_{n-\frac{1}{2}}(z) = \frac{1}{n-m-\frac{1}{2}} \times \left[(2n-2)zP^m_{n-1\frac{1}{2}}(z) - (n+m-1\frac{1}{2})P^m_{n-2\frac{1}{2}}(z)\right], \tag{4.36}$$

$$Q^m_{n-\frac{1}{2}}(z) = \frac{1}{n+m+\frac{1}{2}} \times \left[(2n+2)zQ^m_{n+\frac{1}{2}}(z) - (n-m+1\frac{1}{2})Q^m_{n+1\frac{1}{2}}(z)\right]. \tag{4.37}$$

Note that P is calculated for successively increasing values of n, while Q is calculated for decreasing values. This is necessary for the recurrences to be stable.

The key values used to start the recurrences are given by [55]

$$P^m_{n-\frac{1}{2}}(z) = \frac{\Gamma(n+m+\frac{1}{2})}{\Gamma(n-m+\frac{1}{2})}\frac{(z^2-1)^{\frac{1}{2}m}z^{n-m-\frac{1}{2}}}{2^m m!} \times F\left(\frac{1}{2}(m-n+\frac{1}{2}), \frac{1}{2}(m-n+1\frac{1}{2}); m+1; \frac{z^2-1}{z^2}\right) \tag{4.38}$$

$$Q^m_{n-\frac{1}{2}}(z) = \frac{\Gamma(\frac{1}{2})\Gamma(n+m+\frac{1}{2})}{\Gamma(n+1)}\frac{(-1)^m}{\sqrt{2}(z^2-1)^{\frac{1}{4}}(z+\sqrt{z^2-1})^n}$$

$$\times F\left(\frac{1}{2}+m, \frac{1}{2}-m; n+1; -t\right), \tag{4.39}$$

where

$$t = \frac{z-\sqrt{z^2-1}}{2\sqrt{z^2-1}}, \tag{4.40}$$

Γ is the gamma function, and F is the hypergeometric function. For information on how to calculate Γ and F see [1, 58]. Recurrences for increasing and decreasing m are unstable, so new key values are needed for each value of m.

The derivatives of the Legendre functions P and Q are given by [55]

$$\begin{aligned} U'^m_{n-\frac{1}{2}}(z) &= \frac{1}{z^2-1} \\ &\times \left[(n-\frac{1}{2})zU^m_{n-\frac{1}{2}}(z) - (n+m-\frac{1}{2})U^m_{n-1\frac{1}{2}}(z)\right] \end{aligned} \tag{4.41}$$

$$\begin{aligned} U'^m_{n-\frac{1}{2}}(z) &= \frac{1}{z^2-1} \\ &\times \left[-(n+\frac{1}{2})zU^m_{n-\frac{1}{2}}(z) + (n-m+\frac{1}{2})U^m_{n+\frac{1}{2}}(z)\right], \end{aligned} \tag{4.42}$$

where U can be either P or Q.

4.2.2 Boundary

This section describes the calculation of quantities that depend only on the boundary, that is the internal and external radii of the torus, r and R, and the dielectric constants inside and outside the torus ε_2 and ε_1. The torus scale factor a and boundary mu coordinate μ_1 are given by

$$a = \sqrt{R^2-r^2} \tag{4.43}$$

$$\mu_1 = \cosh^{-1}\frac{R}{r}. \tag{4.44}$$

The values of and q^m_n are calculated using Eq. 4.23. Then the values of α^m_n and β^m_n are calculated from q^m_n via the continued fractions, Eq. 4.28.

Values of $G^m_{n,N}$ are calculated using the recurrence relations, Eq. 4.30, with key values given by Eqs. 4.32. The next stage of calculation requires values of $G^m_{n,N}$ with N varying between $n-l_{max}$ and $n+l_{max}$. These are stored in an array indexed by m, n, and l, with $N = n+l$, so that as l goes between $-l_{max}$ and l_{max}, N goes between $n-l_{max}$ and $n+l_{max}$, as required.

The recurrence relations generate values of $G^m_{n,N}$ for fixed N and increasing and decreasing n, whereas what is needed are values for fixed n and increasing and decreasing N. The recurrence series run diagonally across the array (indexed by n and l), so care must be taken to generate all required values, and some key values outside the table have to be generated. Values of $G^m_{n,N}$ for negative values of N can be generated by observing that $q^m_{-n} = q^m_n$, $\alpha^m_{-n} = \beta^m_n$, and $\beta^m_{-n} = \alpha^m_n$.

4.2.3 Charges

This section describes the calculation of quantities that depend only on the boundary and the positions of the charges. There are i_{max} charges with magnitude q_{0i} and coordinates $(\mu_{0i}, \eta_{0i}, \phi_{0i})$.

The expansion coefficients E_{nm} in the potential, involve the Green function and λ_N^m, Eq. 4.23. In numerical evaluations, it is easier to deal with real numbers, therefore we separate the real and imaginary parts of the quantities in Eq. 4.26 using

$$\Re(\lambda_N^m) = |\lambda_N^m| \cos n\eta_0, \quad \Im(\lambda_N^m) = |\lambda_N^m| \sin n\eta_0, \tag{4.45}$$

and similar relations for E_{nm}. The real part of Eq. 4.26 then becomes

$$\Re(E_{nm}) = \sum_{N=n-l_{\max}}^{n+l_{\max}} \Re(\lambda_N^m) G_{n,N}^m. \tag{4.46}$$

An identical equation follows for the imaginary part. Here we have truncated the infinite sum to appropriately chosen minimum and maximum values. For negative values of N, note that $\lambda_{-N}^m(R) = \lambda_N^m(R)$ and $\lambda_{-N}^m(I) = -\lambda_N^m(I)$. In the same vein, we introduce the following quantities in place of the complex A'_{nm} and B'_{nm} in the potentials, Eq. 4.11

$$\begin{aligned} \Re(A_{nm}) &= A_{nm} \cos n\eta'_{nm}, \quad \Im(A_{nm}) = A_{nm} \sin n\eta'_{nm}, \\ \Re(B_{nm}) &= B_{nm} \cos n\eta''_{nm}, \quad \Im(B_{nm}) = B_{nm} \sin n\eta''_{nm}. \end{aligned} \tag{4.47}$$

Once E_{nm} is known the values of A_{nm} and C_{nm} are obtained from Eq. 4.23, and the values of B_{nm} then follow from Eq. 4.19. Terms in the sums for the potentials can then be calculated using the relations

$$\begin{aligned} A_{nm} \cos n(\eta - \eta'_{nm}) &= \Re(A_{nm}) \cos n\eta + \Im(A_{nm}) \sin n\eta, \\ B_{nm} \cos n(\eta - \eta'_{nm}) &= \Re(B_{nm}) \cos n\eta + \Im(B_{nm}) \sin n\eta. \end{aligned} \tag{4.48}$$

The effect of all charges on a single point can be evaluated with a single sum by pre-calculating sums involving the B_{nm} for the different charges. This process is described in the next section, but since they depend only on the boundary and the positions of the charges, the sums are defined here. They are

$$\begin{aligned} \mathcal{R}_{nm} &= \sum_{i=1}^{i_{max}} \Re(B_{nmi}) \cos m\phi_{0i} \\ \mathcal{S}_{nm} &= \sum_{i=1}^{i_{max}} \Im(B_{nmi}) \cos m\phi_{0i} \\ \mathcal{T}_{nm} &= \sum_{i=1}^{i_{max}} \Re(B_{nmi}) \sin m\phi_{0i} \\ \mathcal{U}_{nm} &= \sum_{i=1}^{i_{max}} \Im(B_{nmi}) \sin m\phi_{0i} \end{aligned} \tag{4.49}$$

where the index i ranges over all the charges.

4.2.4 Potentials

This section describes the calculation of the electric potential at j_{max} points of interest with coordinates (μ_j, η_j, ϕ_j).

The electric potential at point j due to charge i is

$$\psi_{ij} = f(\mu_j, \eta_j) \sum_{m=0}^{m_{max}} (2 - \delta_{0m}) \cos m(\phi_j - \phi_{0i}) \times \sum_{n=0}^{n_{max}} (2 - \delta_{0n})[\Re(B_{nmi}) \cos n\eta_j + \Im(B_{nmi}) \sin n\eta_j] P^m_{n-\frac{1}{2}}(\cosh \mu_j). \quad (4.50)$$

This is only the potential due to the effect of the charge on the boundary. It excludes the direct effect of the charge, which is calculated using Coulomb's law.

The potential at point j due to *all* charges is

$$\psi_j = \sum_{i=1}^{i_{max}} \psi_{ij}, \quad (4.51)$$

which, by expanding $\cos m(\phi_j - \phi_{0i})$, is

$$\psi_j = f(\mu_j, \eta_j) \sum_{i=1}^{i_{max}} \sum_{m=0}^{m_{max}} (2 - \delta_{0m})[\cos m\phi_j \cos m\phi_{0i} + \sin m\phi_j \sin m\phi_{0i}] \times \sum_{n=0}^{n_{max}} (2 - \delta_{0n})[\Re(B_{nmi}) \cos n\eta_j + \Im(B_{nmi}) \sin n\eta_j] P^m_{n-\frac{1}{2}}(\cosh \mu_j). \quad (4.52)$$

By expanding and rearranging this becomes

$$\psi_j = f(\mu_j, \eta_j) \sum_{m=0}^{m_{max}} \sum_{n=0}^{n_{max}} (2 - \delta_{0m})(2 - \delta_{0n}) \times [(\mathcal{R}_{nm} \cos n\eta_j + \mathcal{S}_{nm} \sin n\eta_j) \cos m\phi_j + (\mathcal{T}_{nm} \cos n\eta_j + \mathcal{U}_{nm} \sin n\eta_j) \sin m\phi_j] P^m_{n-\frac{1}{2}}(\cosh \mu_j). \quad (4.53)$$

Hence potentials at j_{max} points due to i_{max} charges can be calculated in $O(i_{max}) + O(j_{max})$ operations, rather than the $O(i_{max} \times j_{max})$ operations that would be required if equation 4.51 was used naively.

The partial derivatives of the potentials (needed to calculate the electric field) can be found by differentiating equation 4.53. Note that $\frac{\partial \psi}{\partial \mu}$ has a singularity at $\mu = 0$. This reflects the inability of the toroidal coordinate system to describe the $X - Y$ direction of the field for a point on the Z axis. We solve this problem by moving any point on the Z axis a distance of $a \times 10^{-6}$ off the axis for the purpose of calculation.

4.2.5 Conversion of Derivatives

To find the electric field in Cartesian coordinates, the partial derivatives with respect to the toroidal coordinates have to be converted to partial derivatives with respect to cartesian coordinates. This is done using the relations

$$\begin{aligned}\frac{\partial\psi}{\partial x} &= \left(\alpha\frac{\partial\psi}{\partial\mu}+\beta\frac{\partial\psi}{\partial\eta}\right)\cos\phi-\gamma\frac{\partial\psi}{\partial\phi}\sin\phi\\ \frac{\partial\psi}{\partial y} &= \left(\alpha\frac{\partial\psi}{\partial\mu}+\beta\frac{\partial\psi}{\partial\eta}\right)\sin\phi+\gamma\frac{\partial\psi}{\partial\phi}\cos\phi\\ \frac{\partial\psi}{\partial z} &= \beta\frac{\partial\psi}{\partial\mu}-\alpha\frac{\partial\psi}{\partial\eta}\end{aligned} \tag{4.54}$$

where

$$\begin{aligned}\alpha &= \frac{1}{a}(1-\cosh\mu\cos\eta)\\ \beta &= -\frac{1}{a}\sinh\mu\sin\eta\\ \gamma &= \frac{1}{a}\left(\frac{\cosh\mu-\cos\eta}{\sinh\mu}\right).\end{aligned} \tag{4.55}$$

4.2.6 Charges Inside the Boundary

The description so far has been for both points and charges outside the toroidal boundary. For charges inside the boundary (with points still all outside) some modifications need to be made to the formulas. First, exchange P with Q and ε_1 with ε_2 when calculating q_n^m and C_{nm}. Second, omit the factor P/Q when calculating B_{nm}, that is

$$\begin{aligned}\Re(B_{nm}) &= (\Re(A_{nm})-C_{nm}\cos n\eta_0)\\ \Im(B_{nm}) &= (\Im(A_{nm})-C_{nm}\sin n\eta_0).\end{aligned} \tag{4.56}$$

The factor $P^m_{n-\frac{1}{2}}(\cosh\mu_j)$ in the formula for potential is unchanged.

4.3 Testing

To test the precision of the analytical method we place an ion at points on a grid which covers the neck and vestibule of a toroidal channel. Errors are estimated by comparison with a grid calculated using the analytical method with a large number of terms: $m_{max} = 90$, $n_{max} = 180$, and $l_{max} = 20$. The channel has an internal radius of 40 Å and an external radius of 44 Å. The grid runs from $x = 0$, $z = 0$ to $x = 30$ Å, $z = 60$ Å in the $y = 0$ plane. It has a spacing of 1 Å. Points inside the boundary are excluded, as are points outside the boundary but within 1 Å of it. This is the critical region

m_{max}	30		45		60	
n_{max}						
30	18.8	46.0				
45	10.5	32.0				
60	6.6	23.4	4.8	17.4		
75	4.7	18.3	2.7	11.6		
90	3.8	15.3	1.7	8.1	1.2	5.9
105			1.2	6.1	0.7	3.8
120			0.9	4.9	0.4	2.5
135					0.3	1.8
150					0.2	1.3

Table 4.1: Convergence of the analytical method. The numbers in the table are the maximum fractional error (in percent) for the grid of points described in the text. The first number in each column is the error in the potential energy, the second is the error in the force.

for the Brownian dynamics simulations described in the following chapter: the influence of the boundary is small for $z > 60$ Å, and the region where $r > 30$ Å is outside the reservoirs, and so not used in the simulations.

The precision of the analytical solution depends on the number of terms included in the sums. We investigate its convergence characteristics by comparing the maximum fractional errors in the grid for different numbers of terms. The results of varying m_{max} and n_{max} are summarized in Table 4.1: the first number in each column is the error in potential energy, the second is the error in the force. It can be seen that increasing m_{max} does not significantly reduce the error unless n_{max} is also increased. The best precision for a given amount of computational effort occurs when n_{max} is roughly twice m_{max}. For the BD simulations that follow we use $m_{max} = 45$ and $n_{max} = 90$. Figure 4.2 shows the points on the grid where the errors are larger than 1% and 5% for this number of terms. The maximum errors reported in Tab. 4.1 occur only for points very close to the boundary.

We also compare the iterative method with the analytical method. Figure 4.3 shows the point on the grid where the errors are larger than 1% and 5% for the iterative method at medium resolution ($\lambda = 1.5$). The cluster of points at the top right of Fig 4.3 A represent only small absolute errors, since the potential energy is small in this region. Similarly the point at the origin of Fig 4.3 B is at the centre of the channel, where the force is analytically zero (since the channel is symmetric around this point, and no driving force is applied). However, round off and truncation errors in both the iterative and analytical method produce calculated values very close to, but not quite, zero at this point. The fractional difference between these values is greater than 5%, but the absolute error is negligible. Other than

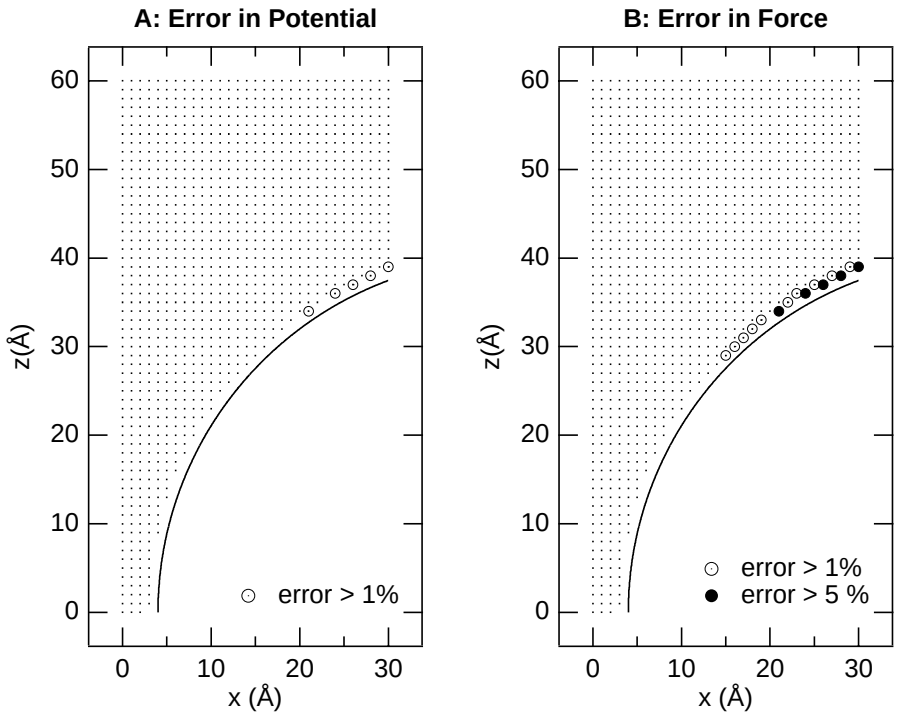

Figure 4.2: Accuracy of the analytical method. Points on the grid where the fractional error in the potential energy (A) and force (B) are greater than 1% and 5%. The number of terms used is $m_{max} = 45$, $n_{max} = 90$, and $l_{max} = 10$. The comparison is with the analytical method using a large number of terms as described in the text.

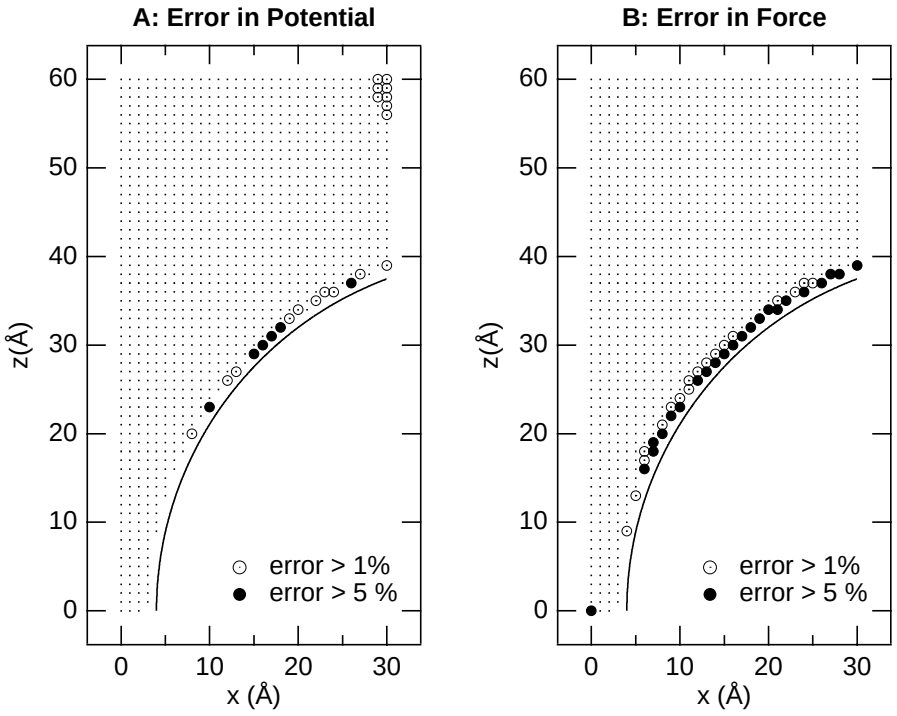

Figure 4.3: Accuracy of the iterative method. Points on the grid where the fractional error in the potential energy (A) and force (B) are greater than 1% and 5%. The iterative method uses 6700 sectors, yielding $\lambda = 1.5$. The sectors are spaced more closely in the neck region. The comparison is with the analytical method using a large number of terms as described in the text. Although there are fractional errors $> 1\%$ to the top right of (A) and $> 5\%$ at the origin of (B), the potential and force respectively are very small here, and the absolute errors are negligible (see text).

this the errors $> 1\%$ are restricted to points close to the boundary, as was the case for the analytical method, although the errors are more widespread for the less accurate iterative method. Note that the errors occur mostly in the vestibule of the channel, not the neck region. This is the effect of the variable sector spacing described in section 3.3.1.

We have performed similar tests on grids on the $z = 32$ Å plane, as well as tests involving multiple ions placed at random locations within the channel. These tests all produce similar results to the ones described here: the errors in the top quadrant of the $y = 0$ plane are representative of those throughout the channel, and are not a special case. In general the fractional errors in force and potential energy are less than 1%, except for ions placed very close to the boundary (< 2 Å) in the vestibule. As explained in section 3.6, these errors are not of great concern, since ions tend to stay away from the walls of the vestibule, and in any case the results of macroscopic electrostatics are

doubtful this close to the boundary (and extra numerical precision will not solve this theoretical problem).

Chapter 5

Brownian Dynamics

This chapter describes our first Brownian dynamics simulations, of a toroidal channel, using the analytical method described in the previous chapter and a Brownian dynamics algorithm due to van Gunsteren and Berendsen [72]. It provides a description of the theory and methods we use in performing BD simulations. The analytical method is around 5 times faster than the iterative method, but this is not yet fast enough to predict conductance. However, it is fast enough to allow the tracks of individual ions to be studied, and doing so yields a surprising amount of qualitative information about the operation of the model channel. Thus the chapter also serves as an intuitive introduction to the behaviour of our model channels, which is examined in more detail in the following chapters.

5.1 Model

5.1.1 Shape of the Channel

The channel boundary is a toroid with a minor radius of 40 Å and a major radius of 44 Å. The narrowest segment of this toroidal channel has the radius of 4 Å, and two vestibules extend 40 Å from the midline. The radius we selected for the constricted segment corresponds that of the potassium ion with its first hydration shell. The shape of the ACh channel determined by Toyoshima and Unwin [70] is better approximated by an hourglass than a toroid, but analytical solutions for Poisson's equation for such a dielectric boundary are not available.

Our model is only of the channel, and does not explicitly include the surrounding lipid membrane. The analytical solution is strictly for a toroidal dielectric boundary, and cannot be extended to include an infinite slab as well, as would be needed to represent the membrane. The model does have, however, a large outside radius (84 Å) compared to that of the ACh channel ($\sim$ 25 Å), and the exterior surface of the channel could be considered to include part of the surrounding membrane. We have ascertained that the

omission of the membrane makes virtually no difference to the potential in the pore. It is the inside boundary of the channel, between the water in the pore and the protein wall, that contributes the majority of the potential. To demonstrate the limited effect of the outside boundary, we reduced the outside radius of a catenary channel (similar to the one in Fig. 3.1) from 43 Å to 28 Å, while keeping all other dimensions constant. The potential barrier height was reduced only by 2 %. Similarly, when we increased the catenary channel's outside radius from 43 Å to 73 Å, the barrier height increased by less than 1 %.

5.1.2 Water as a Continuum

We treat the water as a continuum and the ions as individual entities. Individual ions are assumed to move under the influence of electrostatic forces emanating from other ions, fixed charges, the applied electric field and the dielectric boundary. In the Brownian dynamics simulations, the effects of solvation and the structure of water are taken into account by frictional and random forces. In applying the theory of macroscopic electrostatics to describe long range interactions between particles, we use the bulk dielectric constant. See section 3.1.4 for a discussion of the implications of using macroscopic electrostatic theory and the bulk dielectric constant.

5.1.3 Smooth Water-Protein Interface

We model the water-protein interface as a single, sharp and rigid boundary between dielectrics. In reality, however, the channel wall is not made of a structureless dielectric material. Instead, its surface is likely to be lined with hydrophilic and polar side-chains, although their type, orientation and density remain to be determined. Owing to the presence of these polar groups on the protein wall, there will be a gradual change in the orientation of the water molecules, those water molecules located nearer to the water-protein interface tending to be more ordered than those further away from it. The polar groups and the ordered water near the interface are not explicitly included in our model, being represented by the dielectric boundary. It is possible to treat the interface more accurately by assuming that there is a thin boundary layer with a dielectric constant intermediate between those of protein and water. We have shown elsewhere that the magnitude of error introduced by ignoring the intermediate dielectric layer is negligible [33]. Moreover, we show in the section 5.4.4 that ions in the vestibules tend to be near the central axis, away from the channel wall.

As with the treatment of water as a continuum, these simplified walls subsume the detailed molecular structure of the real protein. This is necessary to make the simulation work, but it risks error if the conductance of the channel depends on the detail of short range interactions between ions

and the protein walls.

5.1.4 Dipole Rings

We investigate how the permeation of ions across the channel is influenced by the presence and absence of dipoles on the protein wall. We assume that these charged moieties are located near the constricted region of the channel, as suggested by structural studies (*e.g.*, Ref. [71]), and represent them as a ring of 4 dipoles at each side of the membrane segment, oriented perpendicular to the central channel axis. These fixed charges represent the charged side chains thought to form a ring around the entrance of the constricted region, and their nearby counter charges. For convenience we adjust the amount of charge rather than the number or positions of the charges, but in reality their side chains would have one electron charge each. Polar groups located in the constricted segment of the channel that may rotate in and out to form temporary hydrogen bonds with an ion navigating across it, as found in gramicidin A pores, are not explicitly modeled in our toroidal channel.

5.1.5 Applied Electric Field

There are two ways of providing the driving force that can move the ion across the channel: a potential difference or a concentration gradient between the two faces of the channel. On a macroscopic level these two are equivalent, being coupled by the Nernst-Planck equation, and concentration differences are often expressed as an equivalent potential. On a microscopic level, however, the physical processes are very different. An electric potential gradient applies a force to every ion, causing it to acquire an average drift velocity. A concentration gradient causes no forces on the ions and no average drift velocity, but their random Brownian motion carries the ions down the concentration gradient. To mimic the real situation, the potential gradient should be generated by a diffuse cloud of unpaired positive ions, representing a surface charge density, in one reservoir and a cloud of unpaired negative ions in the other. The number of unpaired ions must be, to be consistent with the situation in real biological membranes, a small fraction of the total number of the ionic species present. Thus, the clouds of surface charges cannot be represented explicitly within the simulation unless the size of the simulation is expanded by a factor of 100. It is impractical to generate a potential difference with clouds of the ionic atmosphere, although this method is self-consistent and theoretically correct.

We therefore provide the driving force by applying an external electric field, which represents the average effect of the ionic clouds. From a number of current-voltage relationships obtained with a different number of ions in two reservoirs, we have ascertained that the reversal potential occurs

at a potential close to that predicted by the Nernst equation (the electrical potential needed to balance a particular combination of ionic concentrations, so that no current flows, is called the reversal potential: it can be predicted by the Nernst equation). In our simulation system, as in a macroscopic system composed of an ensemble of real biological channels, the force driving ions across the membrane can be provided either by an externally applied electric field or by a concentration gradient.

5.2 Theory

5.2.1 Langevin Equation

Brownian dynamics offers one of the simplest methods for following the trajectories of interacting ions in a fluid. The algorithm for BD is conceptually simple: the motion of the i th ion with mass m_i and charge q_i is governed by the Langevin equation

$$m_i \frac{d\mathbf{v}_i}{dt} = -m_i \gamma_i \mathbf{v}_i + \mathbf{F}_R(t) + q_i \mathbf{E}_i. \tag{5.1}$$

The first two terms on the right-hand side of Eq. 5.1 describe the effects of collisions with the surrounding water molecules. The first term corresponds to an average frictional force with the friction coefficient given by $m_i\gamma_i$: $1/\gamma_i$ is the relaxation time constant of the system. The second term, $\mathbf{F}_R(t)$, represents the random part of the collisions and rapidly fluctuates around a zero mean. The frictional and random forces in Eq. 5.1 are connected through the fluctuation-dissipation theorem [61], which relates the friction coefficient to the autocorrelation function of the random force

$$m_i \gamma_i = \frac{1}{2kT} \int_{-\infty}^{\infty} \langle F_R(0) F_R(t) \rangle dt, \tag{5.2}$$

where k and T are the Boltzmann constant and temperature in degrees Kelvin, respectively. Here and throughout angular brackets denote ensemble averages. Finally, $\mathbf{E}_i$ in Eq. 5.1 denotes the total electric field at the position of the ion arising from (i) other ions, (ii) fixed charges in the protein, (iii) membrane potential, and (iv) induced surface charges on the water-protein boundary. This term in Eq. 5.1 is computed by solving Poisson's equation. Note that in three dimensions, Eq. 5.1 has to be solved for each cartesian component (x, y, z) of the velocity.

Here we give the basic steps in solution of the Langevin equation that are implemented in the BD algorithm of van Gunsteren and Berendsen [72]. Using the the integrating factor $e^{\gamma t}$, the Langevin equation, Eq. 5.1, can be integrated from an initial time t_n to t to obtain for the velocity

$$v(t)\, e^{\gamma t} - v(t_n)\, e^{\gamma t_n} = \frac{1}{m} \int_{t_n}^{t} [F(t') + F_R(t')]\, e^{\gamma t'} dt'. \tag{5.3}$$

Here and in the following, the indices referring to ions and Cartesian components are omitted for convenience. The integral over the random force in Eq. 5.3 can be obtained using the stochastic properties of $F_R(t)$. For the electric force, we Taylor expand $F(t)$ around t_n

$$F(t) = F(t_n) + \dot{F}(t_n)(t - t_n) + \ldots, \tag{5.4}$$

where $\dot{F}(t_n)$ denotes the derivative $F(t)$ at $t = t_n$. Here the first order expansion of $F(t)$ is sufficient as the positions in the BD algorithm are exact to third order. Substituting Eq. 5.4 in 5.3 and integrating the force terms gives

$$\begin{aligned} v(t) = v(t_n)\, e^{-\gamma(t-t_n)} &+ \frac{F(t_n)}{m\gamma}\left(1 - e^{-\gamma(t-t_n)}\right) \\ &+ \frac{\dot{F}(t_n)}{m\gamma^2}\left(\gamma(t-t_n) - 1 + e^{-\gamma(t-t_n)}\right) \\ &+ \frac{e^{-\gamma t}}{m}\int_{t_n}^{t} F_R(t')\, e^{\gamma t'} dt'. \end{aligned} \tag{5.5}$$

To find the position after a time step Δt, we need to integrate Eq. 5.5 once more from t_n to $t_n + \Delta t$. Integration of all the terms in Eq 5.5 are straightforward except the last one which can be done by parts using $du = e^{-\gamma t}$ and v as the integral of F_R

$$\begin{aligned} &\int_{t_n}^{t_n+\Delta t} \frac{e^{-\gamma t}}{m}\int_{t_n}^{t} F_R(t')\, e^{\gamma t'} dt' \\ &\quad = \frac{1}{m\gamma}\int_{t_n}^{t_n+\Delta t}\left[1 - e^{\gamma(t-t_n-\Delta t)}\right] F_R(t) dt \\ &\quad \equiv X_n(\Delta t), \end{aligned} \tag{5.6}$$

where we have defined the random variable $X_n(\Delta t)$, which has the same stochastic properties as $F_R(t)$. We refer to Ref. [72] for details of how $X_n(\Delta t)$ is implemented in the BD algorithm. Using Eq. 5.6, the position at time $t_{n+1} = t_n + \Delta t$ is found to be

$$\begin{aligned} x(t_{n+1}) = x(t_n) &+ \frac{v(t_n)}{\gamma}(1 - e^{-\tau}) + \frac{F(t_n)}{m\gamma^2}(\tau - 1 + e^{-\tau}) \\ &+ \frac{\dot{F}(t_n)}{m\gamma^3}\left(\frac{\tau^2}{2} - \tau + 1 - e^{-\tau}\right) + X_n(\Delta t). \end{aligned} \tag{5.7}$$

Here $\tau = \gamma\Delta t$ is a dimensionless parameter which signifies a diffusive regime when $\tau >> 1$ or a microscopic one when $\tau << 1$. A more convenient form for $x(t_{n+1})$, which does not involve the velocity, can be obtained by adding $e^{-\tau}$ times $x(t_{n-1}) \equiv x(t_n - \Delta t)$ to Eq. 5.7

$$x(t_{n+1}) = x(t_n)(1 + e^{-\tau}) - x(t_{n-1})e^{-\tau} + \frac{F(t_n)}{m\gamma^2}\tau(1 - e^{-\tau})$$

$$+ \frac{\dot{F}(t_n)}{m\gamma^3}\left(\frac{\tau^2}{2}(1+e^{-\tau}) - \tau(1-e^{-\tau})\right) + X_n(\Delta t) - X_n(-\Delta t)e^{-\tau}. \quad (5.8)$$

Similarly, a simple expression for the velocity follows by subtracting $x(t_{n-1})$ from Eq. 5.7

$$v(t_n) = \frac{2\gamma}{\sinh\tau}\left[x(t_{n+1}) - x(t_{n-1}) + 2\left(\frac{F(t_n)}{m\gamma^2} - \frac{\dot{F}(t_n)}{m\gamma^3}\right) \times (\sinh\tau - \tau) - X_n(\Delta t) + X_n(-\Delta t)\right]. \quad (5.9)$$

Eqs. 5.8 and 5.9 provide the basic input for the BD algorithm used in the simulations.

5.3 Methods

5.3.1 Algorithm

We solve the Langevin equation using the BD algorithm devised by van Gunsteren and Berendsen [72], which consists of the following computational steps:

- step 1. Compute the electric force $\mathbf{F}(t) = q_i\mathbf{E}_i$ acting on each ion at time t_n and calculate its derivative $[\mathbf{F}(t_n) - \mathbf{F}(t_{n-1})]/\Delta t$.
- step 2. Compute a net stochastic force impinging on each ion over a time period of Δt from a sampled value of $\mathbf{F}_R(t)$.
- step 3. Determine the position of each ion at time $t_n + \Delta t$ and its velocity at time t_n by substituting $\mathbf{F}(t_n)$, its derivative $\mathbf{F}'(t_n)$ and $\mathbf{F}_R(t)$ into the solutions of the Langevin equation (Eqs. 5.8 and 5.9).
- step 4. Repeat the above steps for the desired simulation period.

An advantage of the above algorithm over some earlier ones is that one is not limited by the condition $\Delta t \ll 1/\gamma$. For the Na ions, this condition would require $\Delta t \ll 10$ fs, which would severely limit the applicability of BD to ion channels. With this algorithm only two factors limit the choice of Δt. The average distance a particle traverses in each time step must be small compared to the dimensions of the system. Also, the time derivative of the electric forces must be small relative to the absolute magnitude of the force. In a preliminary series of simulations, we have systematically increased the time step, Δt, from 25 fs to 1.6 ps and examined the motion of the test particle. As Δt increased beyond 100 fs, the trajectory of the

test particle began to deviate systematically from that obtained with a short time step. In the current simulations, we have used $\Delta t = 50$ fs. Using the average thermal velocity for the sodium ions (see Fig. 5.2 A), the average displacement of ions in time Δt is found to be about 0.25 Å. (The radius of the narrow segment of the toroidal channel, in contrast, is 4 Å.) The change in the electric field during this time step is calculated to be at most a few percent.

5.3.2 Reflective Boundaries

When the ionic concentration in the reservoirs is high, ions at times are able to jump large distances and end up very close to another ion. The forces at the next time step in such instances can be very large and the affected ions may leave the system. To correct this problem, we check ion-ion distances at each time step. If two ions are within a 'safe distance', chosen to be 3/4 of the sum of the ionic radii, then their trajectories are traced backwards in time until such a distance is exceeded. By performing these checks and corrections, the system is well behaved over the simulation, even for very high concentrations. Such a minor re-adjustment of the position of an ion is needed about once every 100 time steps when the reservoirs and the channel contain 52 ions. The steep repulsive force at the dielectric boundary due to the image charges and the ion-protein potential is usually sufficient to prevent ions from entering the channel protein. We ensure that no ions appear inside the channel protein by erecting an impermeable hard wall at 1 Å from the water-protein interface. Any ion colliding with this wall is elastically scattered. A similar hard wall is implemented for the reservoir boundaries.

5.3.3 Physical Parameters

The following physical parameters were employed in our calculations for the toroidal channel:
Dielectric constants: $\epsilon_{\text{water}} = 78.54, \quad \epsilon_{\text{prot}} = 2.$
Masses: $m_{\text{Na}} = 3.8 \times 10^{-26}$ kg, $\quad m_{\text{Cl}} = 5.9 \times 10^{-26}$ kg.
Diffusion coefficients: $\text{D}_{\text{Na}} = 1.33 \times 10^{-9}$ m^2 s^{-1}, $\text{D}_{\text{Cl}} = 2.03 \times 10^{-9}$ m^2 s^{-1}.
Relaxation time constants, γ^{-1}: $\gamma_{\text{Na}} = 8.1 \times 10^{13}$ s^{-1}, $\quad \gamma_{\text{Cl}} = 3.4 \times 10^{13}$ s^{-1}.
Ion radii, $r_{\text{Na}} = 0.95$ Å, $\quad r_{\text{Cl}} = 1.81$ Å.
Room temperature: $T_r = 298$ °K.
Boltzmann constant: $k = 1.38 \times 10^{-23}$ JK^{-1}.

Frictional coefficients γ are derived from the diffusion coefficients D by the Nernst-Einstein relationship $D = kT/m\gamma$, that is $\gamma = kT/mD$. However, since the diffusion coefficients were calculated from the limiting equivalent conductivities λ_0 (from Robinson and Stokes [63]) by another form of

this relation, $D = RT\lambda_0/zF^2$, the frictional coefficients are in effect calculated from $\gamma = zeF/m\lambda_0$. The limiting equivalent conductivities are strictly only valid in the limit of infinite dilution. At the concentrations of 150-300 mM used in the simulations the difference is around 10% (see appendix 11.2 of reference [63]). This difference is due to the effect of high concentrations of ions on the structure of bulk water. Since the confined spaces of a channel may have a completely different (and unfortunately unknown) effect on water structure and diffusion coefficients, we do not include compensation for the higher concentrations.

5.3.4 Testing

To confirm that the behavior of the interacting ions deduced from simulations accords with the physical reality, we examined the mean-square displacement, $\langle x^2 \rangle$, the velocity distribution, and the velocity autocorrelation function, $\langle v(0)v(s) \rangle$. These simulations were carried out on the toroidal channel with two reservoirs, as described in section 5.1, except that the dielectric constant of the protein was set equal to that of water. Thus ions are scattered elastically from the boundary but otherwise there were no forces acting on them due to the change in the dielectric constants.

Theoretically, the mean square displacement $\langle x^2 \rangle$ should obey the relation

$$\langle x^2 \rangle = \frac{2kT}{m_i \gamma_i} t, \quad \text{for} \quad t \gg \gamma_i^{-1}. \tag{5.10}$$

In Fig. 5.1, the mean-square displacement obtained for sodium (filled circles) and chloride (open circles) from one simulation lasting 500,000 time steps (25 ns of real time) is plotted against time. These are compared with the predicted slopes obtained from Eq. 5.10 (solid lines in Fig. 5.1). The simulation results are about 7% lower than the predicted values for a bulk solution, which is probably due to ions scattering back from the boundary, retarding their free diffusion.

Figure 5.2 A shows the velocity distributions of sodium and chloride ions in the system. From the equipartition theorem, the equilibrium distribution of the velocity should be Maxwellian of the form [61]

$$F(v)dv = 4\pi n \left[\frac{m_i}{2\pi kT} \right]^{1/2} \exp(-m_i v^2/2kT)\, v^2 dv, \tag{5.11}$$

where n is the number density of ions and $F(v)dv$ is the mean number of ions per unit volume with a speed in the range between v and $v + dv$. The velocity distributions obtained from the BD simulations are seen to match closely those computed from Eq. 5.11 (solid lines).

The velocity autocorrelation function is of the form [61]

$$\langle v(0)v(s) \rangle = \frac{kT}{m_i} \exp(-\gamma_i |s|). \tag{5.12}$$

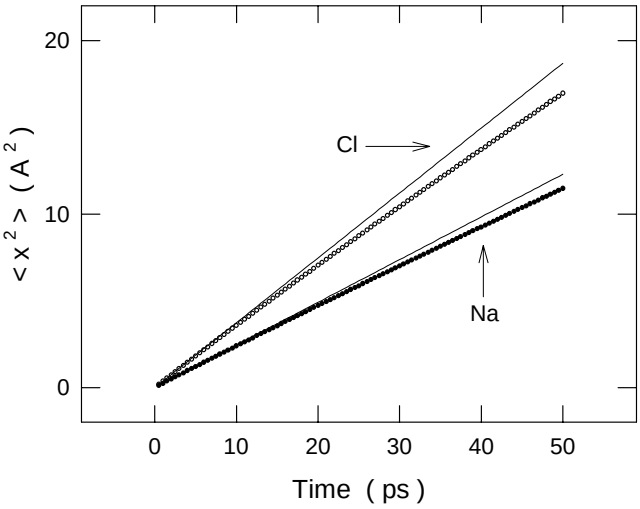

Figure 5.1: Test of the Brownian dynamics algorithm: mean-square displacements. The mean-square displacements, $\langle x^2 \rangle$, of chloride ions ($\circ$) and sodium ions ($\bullet$) are plotted against time. The solid lines superimposed on the graph are derived from the relation, $\langle x^2 \rangle = 2$ D t where the diffusion coefficients D for sodium and chloride ions are given in section 5.3.3. The mean-square displacements determined from simulated data deviated systematically from the predicted values. The reason for these discrepancies between the theoretical and measured values is given in the text.

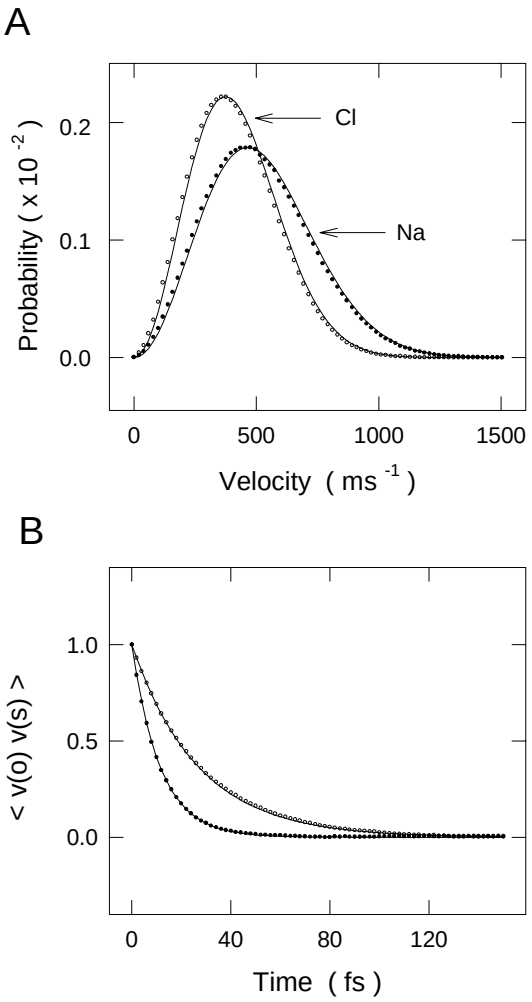

Figure 5.2: Test of the Brownian dynamics algorithm: velocity functions. (A). The Maxwellian velocities distributions, $F(v)dv$, of sodium (•) and chloride (○) ions are normalized for the volume of phase space and plotted. The solid lines superimposed on the measured distributions are calculated from Eq. 5.11. (B). The velocity autocorrelation functions, $\langle v(0)v(s)\rangle$, for sodium (•) and chloride (○) ions decayed exponentially. The continuous lines are calculated from Eq. 5.12.

Thus, regardless of the initial velocity, the successive velocities will be correlated over a time interval of the order of $1/\gamma_i$, the relaxation time constant of the system. To verify Eq. 5.12, we determined the velocities of the ions at every 0.5 fs for 50,000 time steps. The autocorrelation functions shown in Fig. 5.2 B decayed exponentially, as predicted from Eq 5.12 (solid lines). Again, filled and open circles represent the calculated values of sodium and chloride ions, respectively.

From a number of these preliminary simulations, we conclude that the BD algorithm faithfully characterizes the motion of interacting ions in a fluid confined with a reflective boundary.

5.4 Results

5.4.1 Repulsive Dielectric Force

When deliberately placed inside the toroidal channel, ions were rapidly expelled to the reservoir within 1 to 2 ns. A sodium ion in the system, the test particle, was placed inside the channel, on the central axis of the pore at $z = 5$ Å, as indicated in the inset of Fig. 5.3. The initial locations of the remaining 99 ions were randomly assigned. The position of the ion placed in the channel, as well as the remaining ones in the system, was calculated at each discrete time step of 50 fs for 50,000 time steps. Thus, the total simulation time for one such trial was 2.5 ns. These computational steps were repeated 5 times. For each trial, the positions of all ions, except the test particle, at the last time step in the preceding trial were used as the initial starting positions of the subsequent trial. The same series of simulations were repeated for a chloride ion. A representative simulation from each set is shown in Fig. 5.3 A, where the trajectories of the sodium and chloride ions placed in the channel are plotted against time. Each of the consecutive 200 points plotted in Fig. 5.3 A represents an average of 100 time steps or 5 ps. The ensemble averages of 5 trials each for the sodium and chloride ions are illustrated in Fig. 5.3 B. Here the positions of the ions during the entire simulation period of 2.5 ns are plotted.

The speed with which the ionic species were ejected was different. Owing to their higher mobility, chloride ions were consistently expelled faster than sodium ions. Once they were ejected from the channel, these or any other ions in the upper reservoir rarely, if ever, drifted back inside of the channel. These simulations demonstrate that the repulsive dielectric force arising from induced surface charges on the protein wall renders the channel vestibule for the most part devoid of ions.

The magnitude of the repulsive force presented to an ion by the dielectric boundary is sufficiently large that a driving force provided by a transmembrane potential of 100 mV cannot counteract it. This conclusion is based on the following series of simulations. After placing a sodium ion at $z = -20$ Å

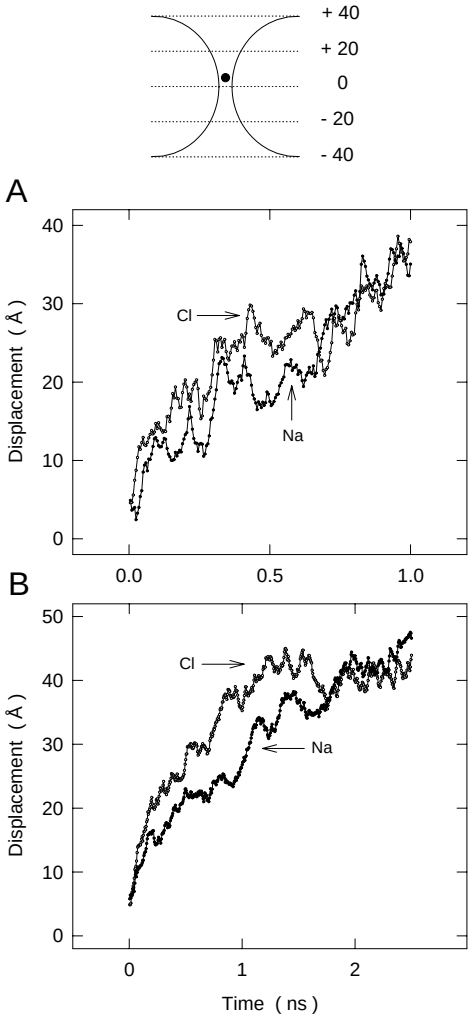

Figure 5.3: Ejection of ions from the vestibule. The filled circle in the inset indicates the initial position of the input ion at the beginning of each set of simulations. Each simulation lasted 50,000 time steps. For clarity, the reservoirs and the remaining 99 ions are not shown. (A). The graphs show the positions of a sodium ion (•) and a chloride (○) ion during the first 1 ns. Each point represents the average of 100 consecutive time steps or 5 ps. From the starting position at $z = 5$ Å, both anion and cation rapidly moved out from the narrow segment of the channel towards the upper reservoir. (B). The mean positions at each consecutive 5 ps are averaged over 5 trials and then plotted against time.

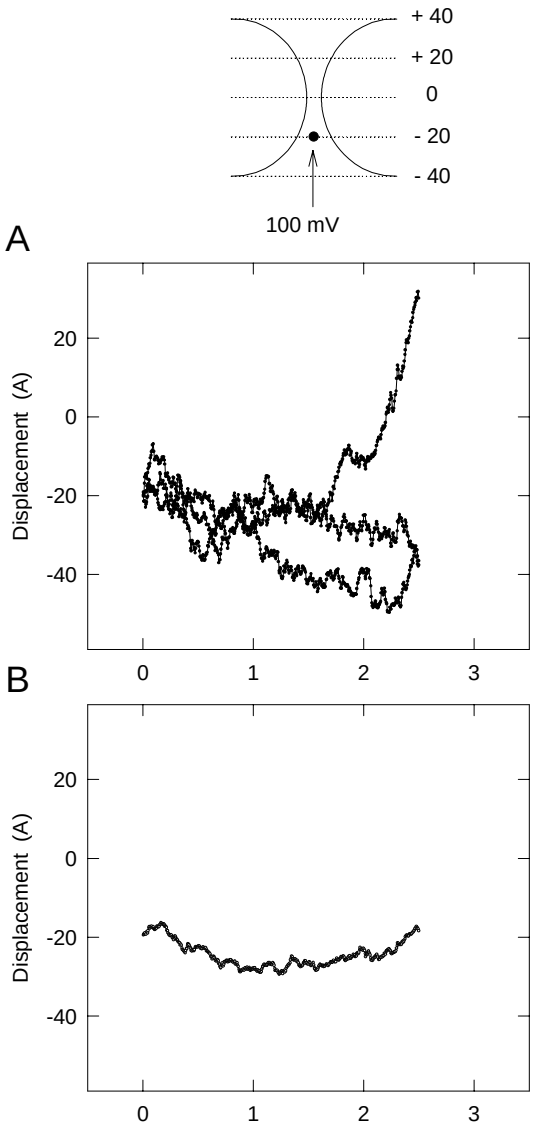

Figure 5.4: Repulsive dielectric force and applied electric field. After placing the test sodium ion at $z = -20$ Å, an electric field of 10^7 V/m was applied in the positive z direction. Shown in (A) and (B) are, respectively, three examples of the trajectories of the test particle and the average trajectory of 9 trials.

(see the inset of Fig. 5.4), an electric field of 10^7 V/m was applied across the channel in the positive z direction. In the absence of any dielectric force opposing it, the ion would have drifted across the channel within 2 ns. In Fig. 5.4 A, 3 trajectories of a sodium ion are illustrated. Again, each point represents the average of 100 consecutive time steps, or 5 ps. In 7 out of 9 trials, the ion placed at $z = -20$ Å was either ejected from the channel and entered the lower reservoir or remained in the channel vestibule. In the remaining 2 trials, the ion was able to penetrate into the other side of the channel. The average of all 9 trials is shown in Fig. 5.4 B. The driving force provided by the applied electric field was effectively opposed by the repulsive dielectric force.

5.4.2 Dipoles in the Transmembrane Segment

The previous simulations indicate that, unless the potential barrier arising from the induced surface charges is counteracted by fixed charges or dipoles in the channel protein, ions in the majority of trials are not able to permeate the channel. In the following series of simulations, we explored the effects of such residual charges on ion permeation, by placing a ring of four dipoles at each end of the transmembrane segment, as described in the section 5.1.4 (see the inset of Fig. 5.5). The total strength of the dipoles on each side was 100×10^{-30} Cm. This configuration of dipoles would be attractive to cations but would create an additional repulsive force for anions.

Figure 5.5 demonstrates the effects of dipoles on the motion of sodium and chloride ions that were deliberately placed inside the channel. A chloride ion placed at $z = 5$ Å along the central axis was expelled from the channel vestibule. In contrast, a sodium ion, when placed at the same position, remained in the vicinity of the dipoles, where the charges of the opposite polarity were providing an attractive potential for the ion. Sample trajectories of a chloride ion (open circles), and a sodium ion (filled circles) are shown in Fig. 5.5 A. The trajectories shown in Fig. 5.5 B are the averages of 5 such trials. Averaging reduced the fluctuations, making the main trend clearer. Thus, a chloride ion was expelled from the channel rather quickly (in less than a nanosecond). For a sodium ion, on the other hand, the dipoles have eliminated the repulsive dielectric force that would have impinged on it, and hence it diffused freely in the channel.

5.4.3 Permeation of Ion Through the Channel

The channel that had been impermeable to both cations and anions (see Fig. 5.4) becomes a cation-selective channel once dipoles are placed in the transmembrane segment such that their negative poles would face the channel lumen. In Fig. 5.6 A, we illustrate the mean positions of a sodium ion during successive 5 ps steps as it moves across the channel under the in-

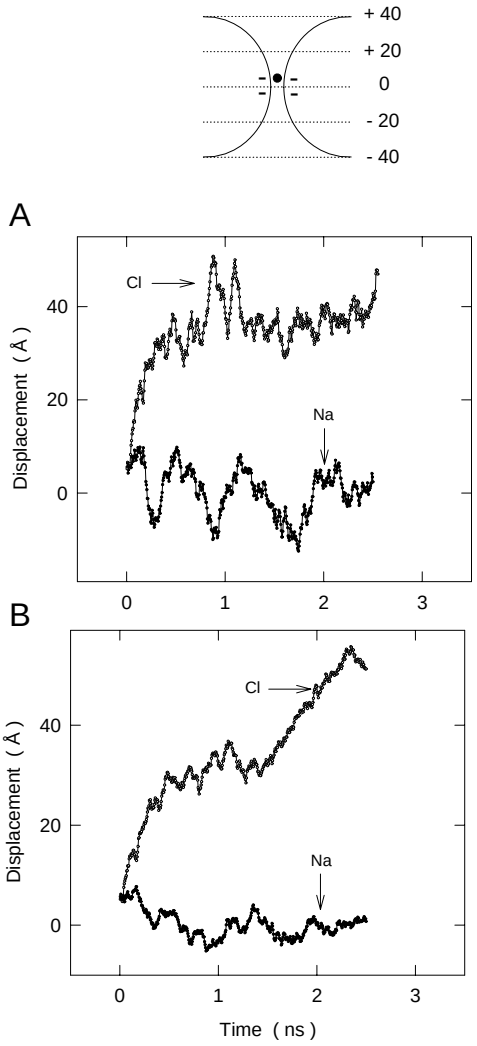

Figure 5.5: Cancellation of repulsive force by dipoles. The test particle, placed at $z = 5$ Å, was released and its positions during the subsequent 2.5 ns were plotted. The procedures of simulations were identical to those in Fig. 5.3, except that 4 dipoles with the total moment of 100×10^{-30} Cm were placed on each side of the midline. The dipoles were placed in the channel protein such that their negative poles would face the lumen. (A). The trajectory of a chloride ion (○) obtained from one trial shows that it was rapidly ejected from the channel. In contrast, a sodium ion (●) remained in the constricted segment of the channel. (B). The trajectories for the test ions, open circles for chloride and filled circles for sodium, are obtained by averaging 5 successive trials.

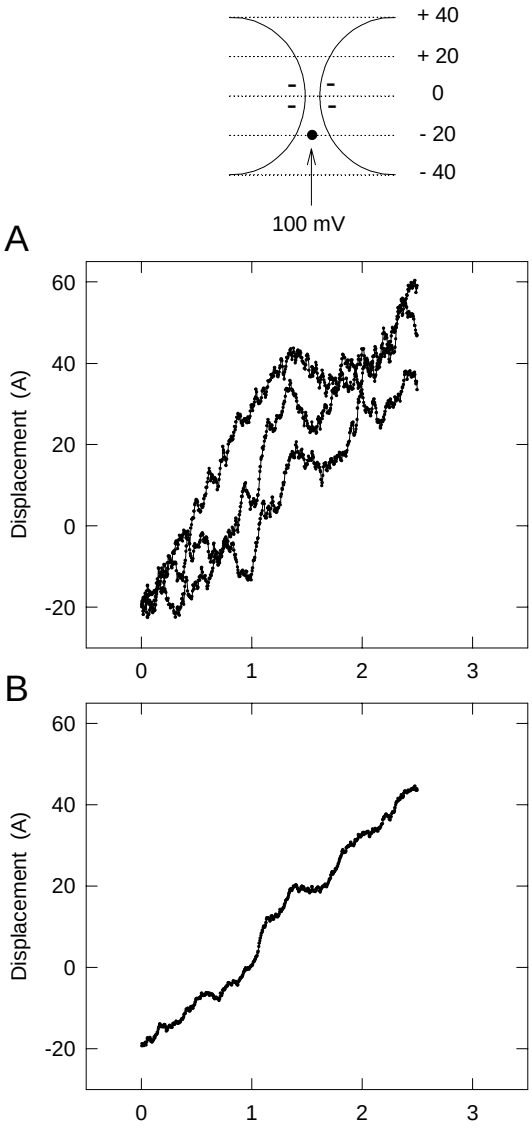

Figure 5.6: Permeation of sodium ions across the channel. A sodium ion was placed at $z = -20$ Å, as indicated in the Inset, and then a potential difference of 100 mV was applied across the channel. Dipoles on each side of the transmembrane segment had the total moment of 100×10^{-30} Cm. (A). Three single trajectories show that the test ions successfully traversed the channel under the influence of the driving force. (B). The trajectory illustrated are the average of 9 trials. The mean drift velocity of the particles was 2.6 m s^{-1}.

fluence of an applied electric field of 10^7 V/m. The three trajectories illustrated in the figure were obtained from the first three consecutive trials. The strength of the dipoles on each side of the transmembrane segment was 100×10^{-30} Cm. In all 9 such attempts, a sodium ion, when released from $z = -20$ Å, successfully navigated across the channel. The trajectory averaged over 9 trials is shown in Fig. 5.6 B.

The sodium ion in these simulations had an average drift velocity of 2.6 m/s in the channel, which is about 5 times faster than that of a sodium ion in bulk electrolyte solutions moving under the influence of the same applied potential gradient. In part this is because the electric field in the constricted segment of the channel, far from being constant, is enhanced by the dielectric boundary and the presence of dipoles (see Ref. [42]). Also noteworthy in Fig. 5.6 is that the ion was not detained at the two regions where the rings of dipoles were located, indicating that the potential well created by them was not deep enough to trap the ion in it for a prolonged period of time.

5.4.4 Trajectory of Ions

The path taken by an ion as it journeys across the channel is predominantly along the central axis. Figure 5.7 shows snapshots of the positions of a sodium ion as it traversed across the channel under the influence of an electric field of 10^7 V/m and in the presence of dipoles of strength 100×10^{-30} Cm (these are the same simulations mentioned in Fig. 5.6). Each dot in the figure represents the location of the ion on the z- and x-axes averaged over 100 time steps. In the first example (Fig. 5.7 A), the ion was slightly deflected towards the dipoles as it moved across the transmembrane segment. In the second and third examples (Fig. 5.7 B, 5.7 C), the ions spent longer periods of time in the vicinity of the rings of dipoles, as indicated by the densities of dots. We have not expected, nor have we found, that an ion would bind to binding sites on the channel protein. These findings are in accord with those reported by Bek and Jakobsson [8].

5.5 Discussion

Despite their preliminary nature, the results in this chapter suggest a qualitative model for conductance in ligand gated cation channels. Although the analytical method is not fast enough to allow the prediction of conductance, by analyzing the trajectory of individual ions we have demonstrated some important points about our model channel. Without dipoles in the channel wall, the electrostatic barrier created by the channel is sufficient to repel ions from the vestibules and neck, preventing ions from crossing the channel even when a realistic driving force is applied (Figs. 5.3 and 5.4). However,

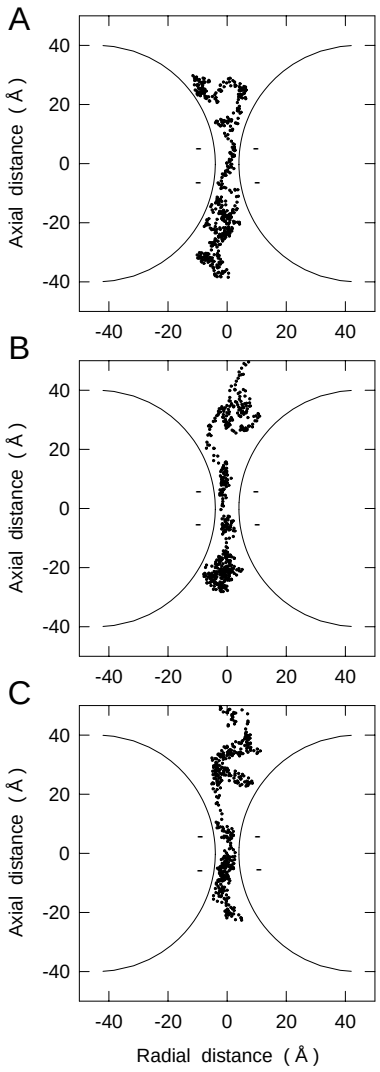

Figure 5.7: The path of ions. The mean positions of the test ions, as they navigate across the channel, are indicated as dots. Each dot represents the average of 100 consecutive positions of the cation, as it drifts across the pore. The data were derived from those illustrated in Fig. 5.6. Three different examples are shown. The small horizontal bars inside the torus boundary indicate the position of the negative ends of the dipoles.

if dipoles are added to the neck region with appropriate strengths and orientations, then the barrier is removed for cations, and they are able to cross the channel (Figs. 5.5 and 5.6). These same dipoles increase the barrier for anions, which are rejected from the channel even more quickly than was the case without dipoles (Fig. 5.5).

The picture that emerges for a ligand gated cation channel is of a device which provides a path for cations by removing the electrostatic barrier of the membrane. The wide vestibules and neck provide water which surround the ion, and reduce the barrier due to dehydration. Some of the barrier remains, however, especially in the neck region, where the pore is narrowest. Dipoles in the neck region overcome this remaining barrier, and cations are able to move through the channel by rapid diffusion. The result is a channel with a large conductance, that is highly selective for anions over cations, but not very selective between cations. This picture is consistent with structural studies, which suggest the wide vestibules (around 12 Å radius) and neck (around 4 Å radius), and the dipoles in the neck region [70, 71, 22]. It is also consistent with patch clamp studies, which demonstrate the large conductance and selectivity for cations (but not among cations) of this class of channel [34, 27, 2]. The Brownian dynamics simulations begin to show how the channel works, how the structural parameters are connected to the conductance characteristics.

Some doubts remain, however. Trajectories of individual ions give a good intuitive feel for the operation of the channel, but cannot yield quantitative predictions of conductance or its relation to structural parameters (such as dipole strength). Although the model is based on realistic physical assumptions, it contains many simplifications, and needs to be tested against experiment before it can be fully believed. For this to happen it needs to be capable of making quantitative predictions. Another area of concern is the effect of the other ions. These are included in the simulations, but the initial placement of the ion under examination is artificial, rather than emerging out of the simulation. The other ions may not have time to react to such a placement, and so shielding by counterions may have been ignored. This is an important point, since the Poisson-Boltzmann and Poisson-Nernst-Plank techniques predict that such shielding completely removes the electrostatic barrier, without any need for compensating dipoles. We have done equilibration tests which indicate that this is not the case [45], but a fully convincing demonstration requires a much longer simulation, in which the ions could enter and leave the channel in a natural and realistic manner. Thus both of these doubts could be removed by sufficiently long simulations, which would be possible if only the electrostatic system could be solved more rapidly. The next chapter describes how this can be achieved.

Chapter 6

Lookup Table Method

The BD algorithm requires calculation of electric forces acting on ions at each time step. Given the positions of ions, this can be achieved by solving Poisson's equation for an appropriate boundary. However, as emphasized above, this direct approach is computationally too expensive to be useful in the long time-scale simulations necessary for the calculation of conductance. Here we adapt an alternative method where the electric field and potential are pre-calculated on a grid of points for various configurations, and the results are stored in a number of lookup tables. During simulations, the field and potential at desired points are reconstructed by interpolating between the table entries. Compared to the analytical solution of Poisson's equation in toroidal coordinates, the lookup method is 60 times faster. The lookup method has the further advantage that one is not restricted to a toroidal channel: numerical solutions of Poisson's equation for more realistic channel shapes can be as easily stored in tables.

6.1 Components of the Potential

For calculational purposes, it is convenient to break the total electric potential V_i experienced by an ion i into four pieces

$$V_i = V_{S,i} + V_{X,i} + \sum_{j \neq i} V_{I,ij} + \sum_{j \neq i} V_{C,ij}, \tag{6.1}$$

where $V_{S,i}$ is the self potential due to the surface charges induced by the ion i on the channel boundary and $V_{X,i}$ is the external potential due to the applied field, fixed charges in the protein wall, and charges induced by these. The next two terms in (6.1) take the influence of other ions into account, namely, $V_{I,ij}$ is the image potential due to the charges induced by the ion j, and $V_{C,ij}$ is the Coulomb potential due to the ion j, which is computed directly from

$$V_{C,ij} = \frac{1}{4\pi\epsilon_0} \frac{q_j}{\epsilon |\mathbf{r}_i - \mathbf{r}_j|}, \tag{6.2}$$

where $\mathbf{r}_i$ and $\mathbf{r}_j$ are the positions of the ions. The electric field experienced by the ion is decomposed in the same way

$$\mathbf{E}_i = \mathbf{E}_{S,i} + \mathbf{E}_{X,i} + \sum_{j \neq i} \mathbf{E}_{I,ij} + \sum_{j \neq i} \mathbf{E}_{C,ij}, \tag{6.3}$$

each field component being defined as in the potential (6.1).

6.2 Generalized Coordinates

The first three components in Eqs. (6.1) and (6.3) depend on the boundary and, in general, they are determined from numerical solutions of Poisson's equation (see chapter 3). Each of these components is calculated for a grid of positions and stored in separate tables. To allow rapid look up, the pre-calculated values must be on an evenly spaced grid. Because the use of a rectilinear grid would result in many wasted points and a jagged edge near the pore boundary, we use a system of generalized cylindrical coordinates in constructing the look up tables. In terms of the cylindrical coordinates (r, θ, z)

$$r = \sqrt{x^2 + y^2}, \quad \theta = \tan^{-1}(y/x), \quad z = z, \tag{6.4}$$

the generalized coordinates (ρ, θ, ζ) are defined as

$$\rho(r, z) = r/r_{\max}(z), \quad \theta = \theta, \quad \zeta(z) = (z - z_{\min})/(z_{\max} - z_{\min}), \tag{6.5}$$

where $r_{\max}(z)$ is the limiting radius of the pore, and $z_{\max}$ and $z_{\min}$ are the maximum and minimum z coordinates for the system. The coordinates ζ and ρ are normalized and cover the range $[0, 1]$. For θ, we use the range $[-\pi, \pi]$ for convenience (see below). The limiting radius $r_{\max}(z)$ is offset from the pore wall by the radius of the smallest ion in the simulation, which defines the closest possible approach for an ion to the pore wall. Both the analytical and iterative methods are unable to calculate the potential *on* the pore wall, and both become less accurate the closer the boundary is approached, so it makes sense to set the limit of the generalized coordinates to the closest possible approach of an ion to the pore wall.

Besides providing a smooth edge near the boundary, the generalized coordinates also allow the cylindrical symmetry of the channel to be exploited. For example, the θ coordinate is redundant in the calculation of the self potential $V_{S,i}$, therefore it is stored in a 2 dimensional table $V_{2d}(\rho_m, \zeta_n)$. Similarly, the image potential $V_{I,ij}$ depends on the relative angle between the ions i and j, and it is stored in a 5 dimensional table $V_{5d}(\rho_m, \zeta_n, \rho_{m'}, \zeta_{n'}, \theta_k)$. Due to reflection symmetry, θ_k and $-\theta_k$ lead to the same image potential. Hence θ_k in V_{5d} covers only the range $[0, \pi]$. The fixed charges do not possess any particular symmetry, so the external potential $V_{X,i}$ is stored in a full 3 dimensional table $V_{3d}(\rho_m, \zeta_n, \theta_k)$. Here θ_k covers the whole range $[-\pi, \pi]$.

The electric field is stored in the same way as the potential, except that three values are required for each point in a table, one for each Cartesian component of the field. So while the field tables are indexed by the generalized coordinates, their contents are stored as Cartesian coordinates in the tables $\mathbf{E}_{2d}(\rho_m, \zeta_n)$, $\mathbf{E}_{3d}(\rho_m, \zeta_n, \theta_k)$, and $\mathbf{E}_{5d}(\rho_m, \zeta_n, \rho_{m'}, \zeta_{n'}, \theta_k)$. Note that, in principle, these results could be combined and stored in the same table. However, separate tables are more flexible and assist in minimizing the interpolation error, and are therefore preferred.

6.3 Lookup Algorithm

Once the positions of the ions have been converted to generalized coordinates, the extraction of the potential and field from the tables is relatively straightforward, and therefore fast. The values of the electric potential and field at the position of the ion are extracted from the tables by multidimensional linear interpolation, a simple algorithm that generalizes easily to dimensions greater than 2 [58]. Because the grid points are evenly spaced in the generalized coordinates, the appropriate indices can be found by division, rather than by a time consuming binary search. For an ion i with charge q_i at the position $\mathbf{r}_i = (\rho_i, \zeta_i, \theta_i)$ and another ion with charge q_j at $\mathbf{r}_j = (\rho_j, \zeta_j, \theta_i)$, the potentials are given by

$$\begin{aligned} V_{S,i} &= \frac{q_i}{e} V_{2d}(\rho_i, \zeta_i), \\ V_{X,i} &= V_{3d}(\rho_i, \zeta_i, \theta_i), \\ V_{I,ij} &= \frac{q_j}{e} V_{5d}(\rho_i, \zeta_i, \rho_j, \zeta_j, |\theta_i - \theta_j|), \end{aligned} \tag{6.6}$$

where $V_{2d}(\rho_i, \zeta_i)$, $V_{3d}(\rho_i, \zeta_i, \theta_i)$, and $V_{5d}(\rho_i, \zeta_i, \rho_j, \zeta_j, |\theta_i - \theta_j|)$ are obtained by applying the interpolation algorithm to the 2 dimensional self potential table, the 3 dimensional external potential table, and the 5 dimensional image potential table, respectively. The self potential and image potential tables are constructed assuming a positive unit charge as source, so the results are rescaled to the actual source charge after lookup.

The symmetries used to reduce the size of the tables require that the recovered electric field be rotated and reflected appropriately so that it corresponds to the simulation's Cartesian axes. The fields are extracted from the interpolated table values as follows

$$\begin{aligned} \mathbf{E}_{S,i} &= \frac{q_i}{e} R_z(\theta_i) \mathbf{E}_{2d}(\rho_i, \zeta_i) \\ \mathbf{E}_{X,i} &= \mathbf{E}_{3d}(\rho_i, \zeta_i, \theta_i) \\ \mathbf{E}_{I,ij} &= \frac{q_j}{e} \mathcal{R}_y(\theta_i, \theta_j) R_z(\theta_i) \mathbf{E}_{5d}(\rho_i, \zeta_i, \rho_j, \zeta_j, |\theta_i - \theta_j|) \end{aligned} \tag{6.7}$$

where $R_z(\theta_i)$ denotes the rotation matrix around the z-axis by an angle θ_i

and $\mathcal{R}_y(\theta_i, \theta_j)$ is a reflection operator on the x-z plane defined by

$$\mathcal{R}_y(\theta_i, \theta_j) = \begin{cases} D(1,1,1), & \text{if } \pi > \theta_j - \theta_i > 0, \\ D(1,-1,1), & \text{if } 0 > \theta_j - \theta_i > -\pi. \end{cases} \tag{6.8}$$

Here D denotes a diagonal matrix with entries as indicated in the arguments.

Once the field and potential are known, the force and potential energy on ion i can be calculated from

$$\mathbf{F}_i = q_i \mathbf{E}_i, \tag{6.9}$$

$$U_i = q_i (V_i - \frac{1}{2} V_{S,i}). \tag{6.10}$$

Note that only half the self potential is used when calculating the potential energy, as explained earlier.

6.4 Testing

To test the accuracy of the lookup method, we compare the interpolation results for potential energy and force with those obtained from the analytical solution of Poisson's equation for a toroidal channel in a variety of situations. The channel boundary is generated by rotating a circle in the x-z plane around the z-axis. The radius of the circle is 40 Å and its center is located at $x = 44$ Å, $z = 0$. Refer to chapter 4 for details of the analytical solution. The results of electric potential and each Cartesian component of the field for the self, external and image parts are stored in tables with dimensions (37×97), $(10 \times 171 \times 40)$ and $(7 \times 119 \times 7 \times 119 \times 14)$, respectively. These dimensions are found after an optimization of the lookup program for the toroidal channel. The catenary channel described in Fig. 3.1 has a similar shape, and lookup tables with the same dimensions are used in the BD simulations in the next chapter.

Among the three potential (or field) parts, the self potential displays larger errors compared to the image and external potentials. Therefore, in the following tests, we focus on the potential energy and the force on a single ion in a toroidal channel which has no other fixed charges or external fields. In Fig. 6.1, we show the potential energy and the z-component of the force for a single ion moving parallel to the central axis but offset from it by 3 Å. Since the z-component of the force provides the driving force in the BD simulations, only that one is shown in this figure. The solid lines are calculated from the analytical method, and the circles by interpolating from the pre-calculated values stored in the lookup tables. The spacing between points in the lookup table is 1.77 Å in the z-direction, and the circles are at the midpoints of these intervals, where the maximum interpolation error is expected to occur. The radius of the channel varies with z, and hence the spacing between points in the r-direction changes. Therefore, the circles are

not necessarily located at the midpoints of the interpolation intervals in the radial direction.

The relative error for the potential and force are not shown in a separate graph because they are less than 1% for all the points in Fig. 6.1. Almost identical results are obtained for other ion trajectories parallel to the central axis but with different radial offsets. In Fig. 6.2, we show a similar plot of the potential energy and the radial component of the force in the $z = 0$ plane as the ion is moved radially from the central axis towards the boundary. Note that the closest approach is limited by the size of the ion. Here the circles correspond to the midpoints of the interpolation intervals in both the z and the radial directions. The relative error is again less than 1% for all the points in Fig. 6.2. In Fig. 6.3, we show another comparison for the potential energy and the radial component of the force on a radial trajectory in the $z = 30$ Å plane. Again the circles are chosen at the midpoints of the interpolation intervals. The relative error remains less than 1% for the potential but rises to a few percent for the force for points near the boundary in Fig. 6.3. The agreement between the analytic and lookup methods evident in Figs. 6.1, 6.2, and 6.3 indicates that the interpolation error is negligible for the potential energy and the z-component of the force in the most important parts of the channel.

Tests carried out on a catenary channel yield a similar agreement between the lookup method and the numerical solution results. The relative error is slightly larger when an ion approaches the vestibular wall in the catenary channel, but this is not of great concern in simulations since ions tend to stay away from the water-protein boundary.

The system of generalized coordinates we use has a weakness at the entrance to the pore, where the boundary runs horizontally, perpendicular to the z-axis. The radius suddenly jumps from that of the reservoir to that of the pore entrance. This results in spurious interpolation between points near the channel's top surface and points in the pore entrance. Errors in the potential near the channel's top surface are unlikely to affect the results of simulations. Errors in the potential in the pore entrance are of greater concern. The magnitude of the force is rather small in this region, however, and we have checked in control runs that it has no effect on the simulations. An improved system of generalized coordinates that avoids this problem may be desirable in other applications of this method.

6.5 Performance

The use of lookup tables is practical despite the large number of points at which the field needs to be calculated, because the time used by the algorithms depends much more on the number of solutions needed rather than the number of points per solution. Both the iterative and analytical

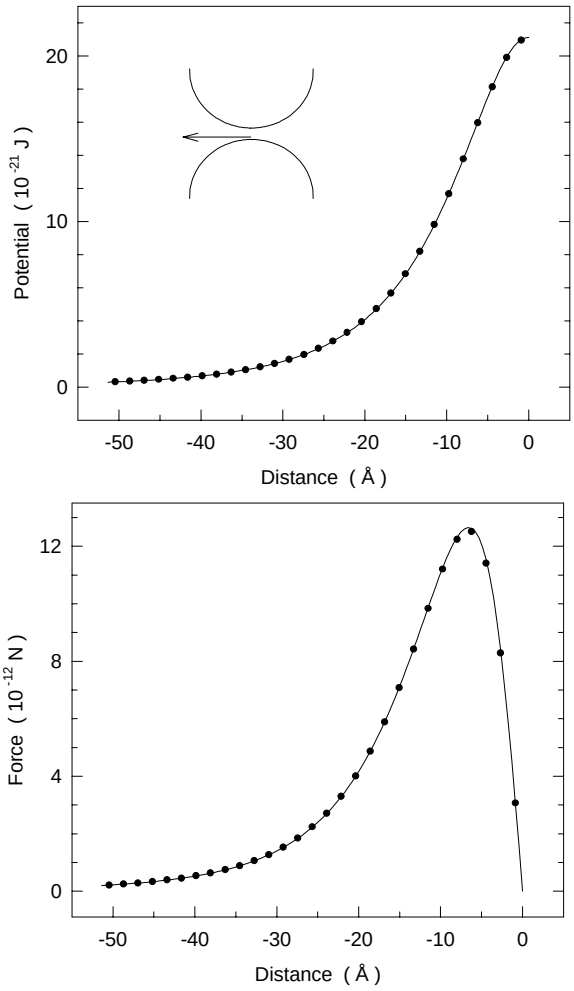

Figure 6.1: Comparison of the potential energy and the z-component of force, obtained from the lookup tables by interpolation (circles), with the analytical solutions (lines) for a toroidal channel. An ion is moved along the trajectory that is parallel to the central axis but is offset from it by 3 Å, as indicated by the arrow in the inset. The position of each circle in the z-direction is located at the midpoint between two adjacent points stored in the lookup table.

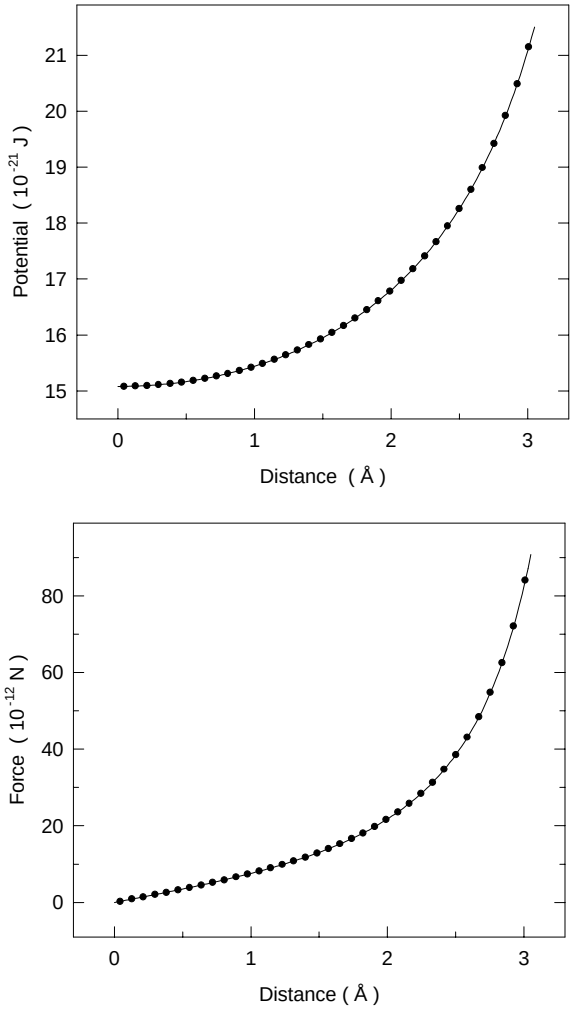

Figure 6.2: Same as Fig. 6.1 but for a radial trajectory in the $z = 0$ plane. The lookup results (circles) are calculated at the midpoints of the interpolation intervals in both the z and the radial directions.

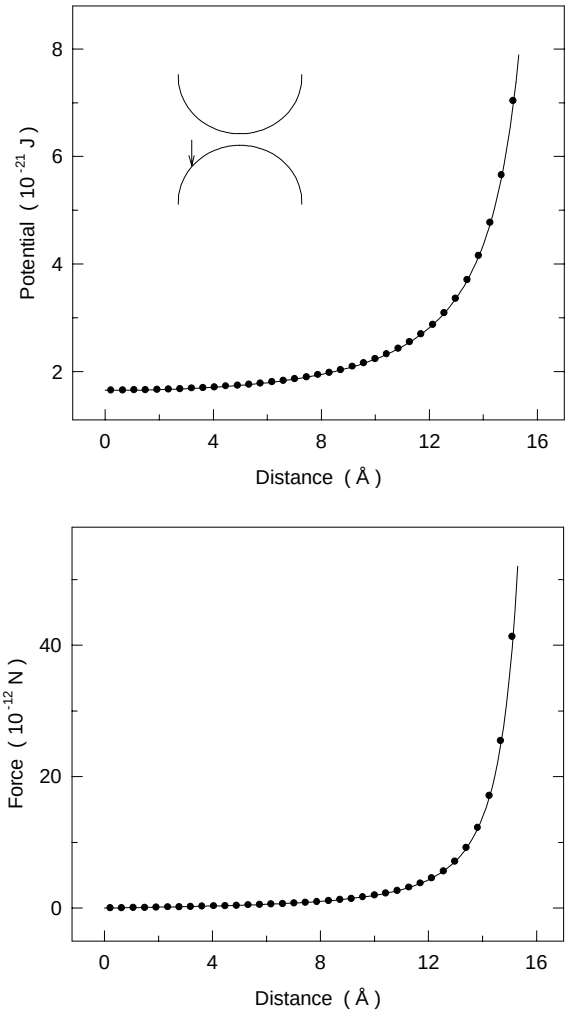

Figure 6.3: Same as Fig. 6.2 but for a radial trajectory in the $z = 30$ Å plane (see inset).

algorithms can easily generate the field at multiple points arising from many charges at given positions (which we call one solution). On the VPP a solution for 50 ions and 16 fixed charges takes 0.4 s (of CPU time) by the analytical algorithm, 2 s by the iterative algorithm, but only 0.006 s by the lookup table method. A BD simulation of 2 million steps would thus take 220 hours by the analytical algorithm, 46 days by the iterative method, and 3 hours by the lookup table method. The filling of the tables takes only an hour using the analytical solution and 10 hours using the iterative solution. To give an example, generating a 5d lookup table using the iterative method (which is the most time consuming) requires only 833 solutions, each for a single ion and at 12000 points. Each solution takes 21 s and the total time required is about 5 hours. Another advantage of the method is that once the tables are constructed for a given geometry, they can be used in many simulations studying different aspects of channel conductance.

Chapter 7

Single-Ion Channel

This chapter describes our BD simulations of a model catenary channel based on the hour-glass shaped acetylcholine receptor channel [70].

7.1 Model

7.1.1 Shape of the Channel

A catenary channel was generated by rotating the closed curve shown in Fig. 7.1 around the symmetry, z-axis. The vestibule of the channel, whose shape is similar to that visible in the electron microscope picture of the acetylcholine channel [70], was generated by a hyperbolic cosine function, $y = a \cosh x/a$, where $a = 4.87$ Å. The radius of the entrance of the vestibule was fixed at 13 Å. Two identical vestibules were connected with a cylindrical transmembrane region of length 10 Å and radius 4 Å. The total interior volume of the model channel was 2.16×10^{-26} m^3. We assumed, for simplicity, that the two vestibules are identical in size, although the image of the channel produced by Toyoshima and Unwin [70] shows that the extracellular vestibule is larger than the intracellular vestibule.

7.1.2 Dipoles in the Protein Wall

To investigate how the permeation of ions across the channel is influenced by the presence and absence of dipoles in the protein wall, we placed in some simulations a set of 4 dipoles inside the protein boundary at $z = 5$ Å and another set of 4 dipoles at $z = -5$ Å. Their orientations were perpendicular to the central axis of the lumen (z-axis). For each dipole, the negative pole, placed 2 Å inside the water-protein boundary, was separated from the positive pole by 5 Å. Thus, if 5/16 of an elementary charge was placed on each pole, then the total moments of 4 such dipoles would be 100×10^{-30} Coulomb-meter. The same configuration of dipoles was used in all the simulations, giving rise to an attractive potential for sodium ions and

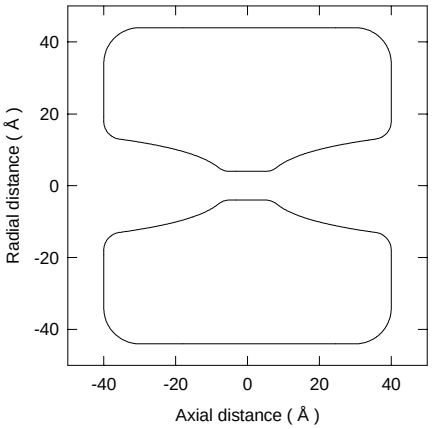

Figure 7.1: Idealized biological ion channel. A model channel with two catenary vestibules was generated by rotating the closed curves along the symmetry z-axis by 180^o. To approximate the shape of the acetylcholine receptor channel, vestibules at each side of the membrane were constructed using a hyperbolic cosine function, $y = a \cosh\ x/a$ where $a = 4.87$ Å. The radius of the entrance of the vestibule was fixed at 13 Å and the cylindrical transmembrane segment had a radius of 4 Å. Each cylindrical reservoir, 60 Å in diameter and 22 Å in height, contained a fixed number of sodium and chloride ions. Unless stated otherwise, the ionic concentration in the volume composed of the channel vestibules and the reservoirs was 300 mM. The cylindrical reservoir had a glass boundary, in that an ion moving out of the boundary was reflected back into the reservoir.

a repulsive potential for chloride ions in the channel. These fixed charges represent the charged side chains thought to form a ring around the entrance of the constricted region [71], and their nearby counter charges. For convenience, we adjust the amount of charge rather than the number or positions of the charges, but in reality the side chains of charged amino acid residues would have one electron charge each if they are fully ionized or unprotonated at neutral pH. Polar groups located in the transmembrane segment of the channel that may rotate in and out to form temporary hydrogen bonds with an ion navigating across it, as found in gramicidin A pores, are not explicitly modeled in our single ion channel.

7.1.3 Energy Barrier in the Transmembrane Segment

An ion in the vestibule needs to surmount an energy barrier to traverse the narrow, constricted segment of the channel. The presence of such an additional energy barrier in the gramicidin pore has been revealed by molecular dynamics calculations. Intuitively, this barrier arises from the interactions between the protein wall and the hydrated ion as the ion negotiates its way into the narrow, cylindrical, transmembrane pore. To enter the narrow segment, the hydration shell of an ion needs to be re-arranged or some of the water molecules in the primary or secondary hydration shell need to be substituted with polar groups on the protein wall. To re-arrange the ion-water geometry requires an additional energy, and the ion can surmount such a barrier only when it gains a sufficient kinetic energy. To mimic a barrier present in the ion channel, we placed in some simulations a potential step near the constricted segment of the channel. The energy must be paid to enter the neck, and is returned when the ion exits. The method we used for implementing such a potential barrier in the Brownian dynamics algorithm is detailed below.

7.1.4 Applied Electric Field

A potential difference across a lipid membrane is produced by a surface charge density on each side of the membrane. In microscopic terms, the surface charge density is a cloud of unpaired ions on either side of the membrane. Because these clouds are too diffuse to be explicitly included in our simulation, we apply an external electric field E of a constant strength to represent the average effect of the ionic clouds. In the absence of any dielectric boundary, the potential difference across a channel with the length d is E/d. The presence of a dielectric boundary, however, severely distorts the field, enhancing it in the transmembrane segment and attenuating it in the vestibule. Thus, the precise potential difference will depend on the selected reference points at the two sides of the catenary channel. For simplicity, we apply a field strength of 10^7 V m^{-1} and refer to it as an applied potential

of 100 mV.

7.2 Theory

7.2.1 Pöschl-Teller Function

If the ionic concentrations on the two faces of the channel are the same, the current-voltage relationship obtained from patch-clamp recordings is in general ohmic. The current-voltage relationship deduced from our simulations becomes nonlinear whenever there is a potential barrier for the ions to surmount in order to cross the channel (Fig. 7.8). This deviation from Ohm's law is more pronounced when the potential barrier is large. Although the precise shape of the curve cannot be deduced *a priori*, it is easy to see how such a curvature in the current-voltage relationship would arise. The presence of a barrier is less of an impediment when the driving force is large. This intuitive observation suggests a modification of Ohm's law with the Pöschl-Teller function

$$I = \frac{\gamma V}{1 + \beta/\cosh(eV/V_B)}, \tag{7.1}$$

where γ is the conductance, V_B is the barrier height, and β is a dimensionless constant. When $eV \gg V_B$, the denominator goes to 1, and one recovers Ohm's law. For $eV \ll V_B$, Eq. (7.1) is again linear but with a conductance reduced to $\gamma V/(1+\beta)$. The nonlinearities in the $I-V$ curves become apparent only when $eV > V_B$, which corresponds to the region $V \approx 100 \sim 200$ mV for our model channel.

7.2.2 Michaelis-Menten Equation

Experimentally it has been shown that the current first increases with an increasing ionic concentration and then saturates [59, 31]. Such a relationship is expected to be found when the transport of ions across the channel is determined by two independent processes, one of which depends upon ion concentration and one that does not. In our simulations, for example, the time τ_1 it takes for an ion to arrive near the constricted segment is inversely proportional to the electric field E and ionic concentration $[c]$, whereas the time τ_2 it takes for the ion to acquire a sufficient kinetic energy to surmount the barrier placed near the transmembrane segment and traverse the second half of the channel is relatively independent of the ionic concentration but dependent only on the electric field. Thus, assuming a uniform electric field, the transit times can be written as

$$\tau_1 = \frac{k_1}{[c]\ E}, \quad \tau_2 = \frac{k_2}{E}, \tag{7.2}$$

where k_1 and k_2 are constants. The total time τ it takes an ion to traverse the channel is $\tau = \tau_1 + \tau_2$, and the current flowing across it will be $I = nze$, where the number n of ions carrying charges ze is $1/\tau$. Thus, the current is inversely proportional to the total transit time, that is,

$$I \propto \frac{ze}{(\tau_1 + \tau_2)} = \frac{zeE}{k_1/[c] + k_2}. \tag{7.3}$$

For large concentrations, Eq. (7.3) approaches to a maximum value that we denote by $I_{\max} = zeE/k_2$. Factoring out k_2 and introducing $K_s = k_1/k_2$, Eq. (7.3) can be written in the form

$$I = \frac{I_{\max}}{1 + K_s/[c]}. \tag{7.4}$$

The form of this equation is identical to that of the Michaelis-Menten equation, which is derived under an entirely different set of assumptions. The curves calculated from Eq. (7.4) fit the current-concentration relationships obtained from our simulations reasonably well (see Fig. 7.9).

7.3 Methods

7.3.1 Stochastic Boundaries

To ensure that the desired intracellular and extracellular ion concentrations were maintained throughout the simulation, a stochastic boundary was applied. When an ion crossed the transmembrane segment, an ion of the same species was transplanted so as to maintain the original concentrations on both sides of the membrane. For example, if a sodium ion from the left-hand side of the channel crossed the narrow transmembrane segment and reached the imaginary plane at $z = 10$ Å, then a sodium ion located at the furthermost right-hand reservoir was taken out and placed in the far left-hand side of the left reservoir. When transplanting ions, we chose a point no closer to another ion than the defined safe distance. The stochastic boundary trigger points, located at $z = \pm 10$ Å, were checked at each time step of the simulation.

7.3.2 Short Timestep Algorithm

The use of a long time step causes a problem in implementing potential barriers and steps in Brownian dynamics as short range forces. In our simulations, the Brownian dynamics algorithm operates predominantly in the diffusive regime. In other words, random forces are far more important than the velocity on the previous step in determining an ion's new velocity and position. The algorithm devised by van Gunsteren and Berendsen [72] uses

the factors $[\exp(-\gamma\Delta t)]$ and $[1-\exp(-\gamma\Delta t)]$ to switch between kinetic and diffusive regions. With the long time step ($\Delta t = 100$ fs) that we use,

$$\begin{aligned} 1-\exp(-\gamma_{\mathrm{Na}}\Delta t) &= 0.9997, \\ 1-\exp(-\gamma_{\mathrm{Cl}}\Delta t) &= 0.9666. \end{aligned}$$

Thus, for chloride ions only 3% of the previous velocity remains after one time step, while the motion of sodium ions is in effect purely diffusive, with no velocity correlation between steps. Since an ion can move a large fraction of the barrier width in a single time step (around 0.3 Å on average), the effect of the barrier force on the ion's motion will not be accurately integrated. Also, in the diffusive regime, external forces cause only an average drift velocity which does not move the ion far in a single time step. For example, a repulsive force of 120×10^{-12} N ($3\ kT_r$ over 1 Å) produces a drift velocity of 39 ms^{-1} for sodium, and a displacement of 0.04 Å in one time step. This is only 1/7 of the average random displacement in one time step—an ion can diffuse right through a potential barrier before the barrier force has time to act.

To obviate these problems, we used two different time steps: a short time step of 1 fs when an ion was in the process of climbing or descending the barrier and the long time step of 100 fs otherwise. A smooth potential barrier of height V_B was erected at $z = \pm 10$ Å (5 Å from the entrance of the cylindrical segment), with the profiles at the ends as

$$U(s) = V_B(10s^3 - 15s^4 + 6s^5), \tag{7.5}$$

where

$$s = \frac{z - z_b}{\Delta z} + \frac{1}{2}. \tag{7.6}$$

Here $z_b = \pm 10$ Å is the location of the center of the profile and $\Delta z = 1$ Å is the width of the profile. The potential profile $U(s)$ is chosen such that it rises from zero at $z = \pm 10.5$ to V_B at $z = \pm 9.5$, and the first and second derivatives of $U(s)$ vanish at $z = \pm 9.5$ and $z = \pm 10.5$. The force due to the barrier is obtained by differentiating Eq. (7.5).

We included a safety distance of 0.5 Å in the potential profile. Thus, whenever ions were in the band of $z = 9$ - 11 Å or $z = -9$ to -11 Å, we switched from long time steps to an equivalent sequence of short time steps for those ions. Trajectories of ions in these bands were determined by a sequence of 100 short time steps for the subsequent 100 fs. In the meantime, all the other ions were simulated for a single long time steps in the normal way. The long range (electrostatic) forces on the ion were calculated at the start of the sequence of 100 short steps, and held constant thereafter. Similarly, reflection from the boundary walls was done once at the end of the sequence of short steps. The force from the barrier, however, was recalculated for each short step, thus ensuring that the effect of the barrier on the ion's motion would be accurately simulated.

7.3.3 Procedure for Calculating Conductance

Simulations under various conditions, each lasting between 500,000 and 2,000,000 time steps, were repeated many times, from 5 to 9 trials. For the first trial, the positions of ions in the reservoirs were assigned randomly with the proviso that the minimum ion-ion distance should be 2.7 Å, or 1.5 times the radius of a chloride ion. For successive trials, the positions of the ions in the last time step were used as the initial starting positions of the following trial. The current given in pA was extrapolated from the total number of ions traversing the channel over the simulation period.

On each side of the vestibule, a cylindrical reservoir with radius 30 Å and an adjustable height was placed. A fixed number of sodium and chloride ions were placed in each reservoir, and the height of the cylindrical reservoir was adjusted to give a desired ionic concentration. As ions were forbidden to approach the wall of the reservoir within 1 Å, the effective radius of the cylindrical reservoir was 29 Å. For example, if 13 sodium and 13 chloride ions were placed in each reservoir and the desired ionic concentration was 300 mM, the height of each of the two cylindrical reservoirs was adjusted to 22 Å.

7.4 Results

7.4.1 Dipoles in the Channel

In the absence of any dipoles in the protein wall, the potential barrier presented to an ion moving under the influence of an applied potential of 100 mV is shown in Fig. 7.2 (top curve, labeled 0). The potential profile presented to the ion as it moved from outside (left-hand side) to inside (right-hand side) increased slowly, peaking at the center of the cylindrical transmembrane segment (labeled 0 Å), and then decreased steadily as it traversed the second half of the channel. Without the membrane potential, one would have obtained a symmetrical, bell-shaped barrier with a peak height of 14.5×10^{21} J. The presence of the membrane potential had lowered the relative height of the barrier to 3.5×10^{21} J and distorted the shape of the profile to an asymmetrical curve.

Two rings of dipoles, together with an applied electric potential of 100 mV, eliminated the repulsive dielectric force. The number accompanying each curve in Fig. 7.2 represents the total strength of 4 dipoles ($\times 10^{-30}$ Cm) in each ring. Since there were two rings of dipoles, one at $z = -5$ Å and the other at $z = +5$ Å, the strength of dipoles placed on the entire channel wall was twice the value indicated in the figure. In the presence of dipoles, an ion traversing from outside to inside would encounter an attractive potential throughout its trajectory. With each stepwise increase in dipole strength, what used to be a potential barrier became a potential well whose depth

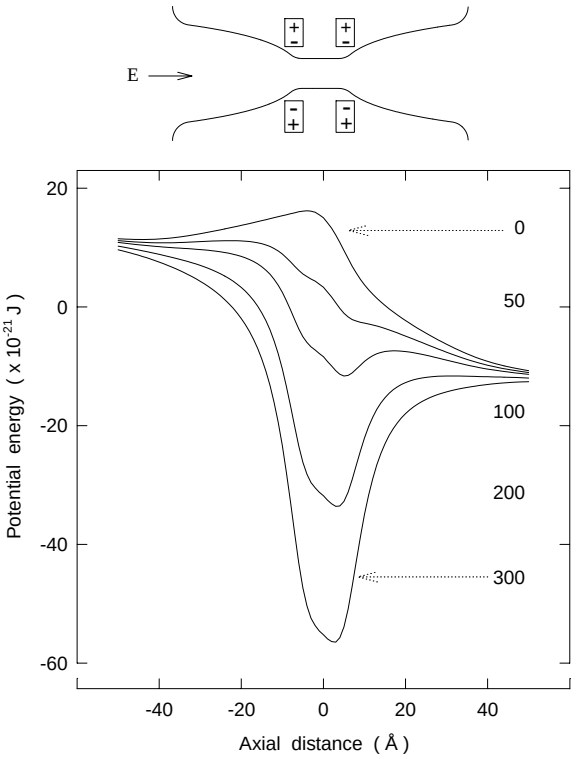

Figure 7.2: Changes in the potential profile with dipole strength. The potential barrier presented to a cation is plotted against its position along its trajectory. A membrane potential of 100 mV was applied such that inside (right-hand side) was negative with respect to outside (left-hand side). The value at each position was computed from a numerical method of solving Poisson's equation. The uppermost curve, labeled 0, was obtained in the absence of dipoles on the channel wall. The next four curves represent the potential profiles encountered by a cation traversing the channel in the presence of dipoles with strengths of, respectively, 50, 100, 200 and 300×10^{-30} Cm. The approximate positions of four of the 8 dipoles in the channel are indicated in the inset. The remaining four dipoles are on the orthogonal plane to those shown.

increased with the strength of dipole moments.

In Fig. 7.3, the number of ions that traversed the channel under the driving force of 100 mV during a simulation period of 0.45 μs (4.5 million time steps) is converted to current in pA and plotted against the dipole strength. On the right-hand ordinate of Fig. 7.3, current in pA are converted to conductance in pS at the physiological concentration of 150 mM. Since the current in these ranges of ionic concentrations increases almost linearly with concentration (see later), such an extrapolation of conductance results is justified. With no dipoles placed on the channel wall, the number of sodium ions that traversed from outside to inside in 0.45 μs was 10, which corresponds to a current of 3.6 pA. The net current increased rapidly with the increasing dipole strength up to 100×10^{-30} Cm (filled circles in Fig. 7.3). The number of ions crossing the channel increased further with a further increase in the dipole strength, but many ions were also traversing in the opposite direction, against the direction of the applied electric field. The current flowing from inside to outside is indicated as open circles in Fig. 7.3. As a result, the net current actually decreased as the dipole strength was increased further from 300 to 600×10^{-30} Cm.

7.4.2 Ionic Concentrations in the Channel

In the volume of our model channel, which is 2.16×10^{-26} m^3, there would be 720 water molecules. At a concentration of 300 mM, a similar bulk volume would contain 4 sodium and 4 chloride ions. Here we examine the number of sodium and chloride ions inside the channel under various conditions. To compute the average number and concentration of sodium and chloride ions inside the channel, we divided the model catenary channel, whose length is 80 Å, into sixteen 5-Å-thin sections as shown in the inset of Fig. 7.4. The volumes of the slices from the outermost layer to the smallest layer in the transmembrane segment are 2.94, 2.18, 1.88, 1.54, 1.16, 0.71, 0.25 and 0.15×10^{-27} m^3.

In the absence of a membrane potential and dipoles in the protein, ions were virtually excluded from entering the vestibule neck owing to the repulsive dielectric force presented to them by the dielectric wall. In Fig. 7.4 A and Fig. 7.4 B, the time averages of sodium and chloride concentrations in the channel are illustrated. The number of ions present in each layer per unit time was first tabulated (filled and open circles) and then the concentration in each layer was derived by taking into account its volume. The average ionic concentration in each of the two outermost layers was about 10% lower than that in the adjoining reservoir, which was 300 mM. The ionic concentration in successive layers declined progressively, dropping to less than 10% of the reservoir value in the neck region.

When a membrane potential of 100 mV was applied across the channel, such that the right-hand side reservoir was made negative with respect to the

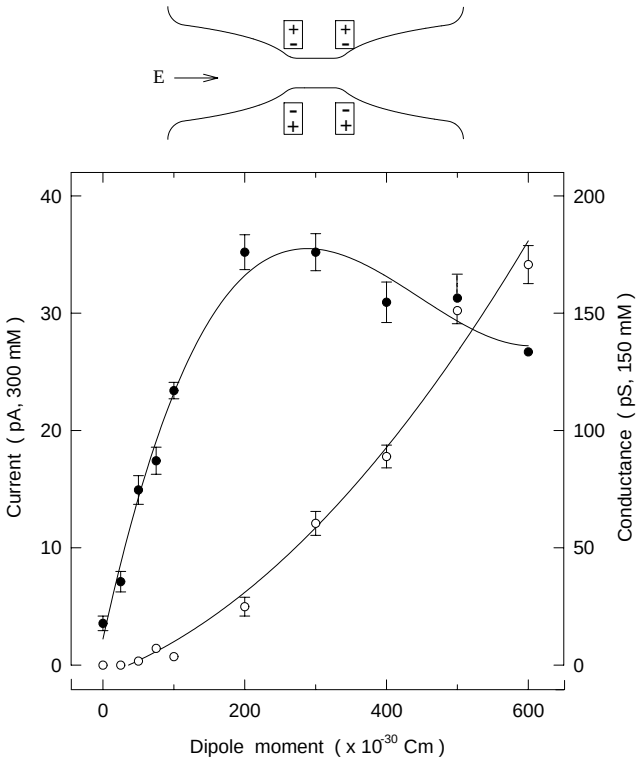

Figure 7.3: Channel conductance as a function of dipole strength. The magnitudes of sodium currents flowing across the channel in the presence of a membrane potential of 100 mV are plotted against strengths of dipoles. The ionic concentration of the reservoir was 300 mV. The left-hand side of the ordinate indicates the current in pA at 300 mM, whereas the right-hand side of the ordinate indicates the conductance in pS at 150 mM. The filled circles show the net current, *i.e.*, the sum of currents in both directions, which flows from outside to inside. The open circles show the current flowing against the potential gradient, namely, from inside to outside. Simulation time for each data point was 0.45 μs, except the value for 100 $\times 10^{-30}$ Cm, which was 2 μs. The points were fitted with a polynomial function.

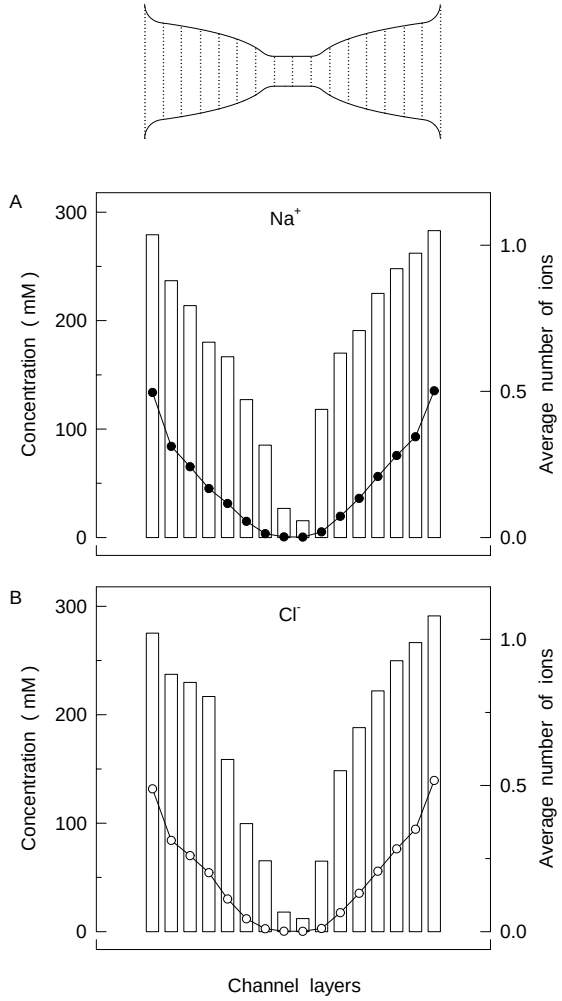

Figure 7.4: Concentrations of sodium and chloride ions in the channel. The model channel was divided into sixteen 5-Å-thick sections, as indicated in the inset, and the average number of ions present over the simulation period of 0.45 μs in each section was tabulated (filled and open circles). The ionic concentration in each section was then calculated by dividing the average number of ions in each section by its volume (bars). The concentration of sodium (and chloride) ions in the reservoirs was 300 mM in this and the following 3 figures. With no dipoles on the channel wall and no applied electric field, the probability of sodium ions (A) and chloride ions (B) being in each section decreased steadily with its distance from the reservoir.

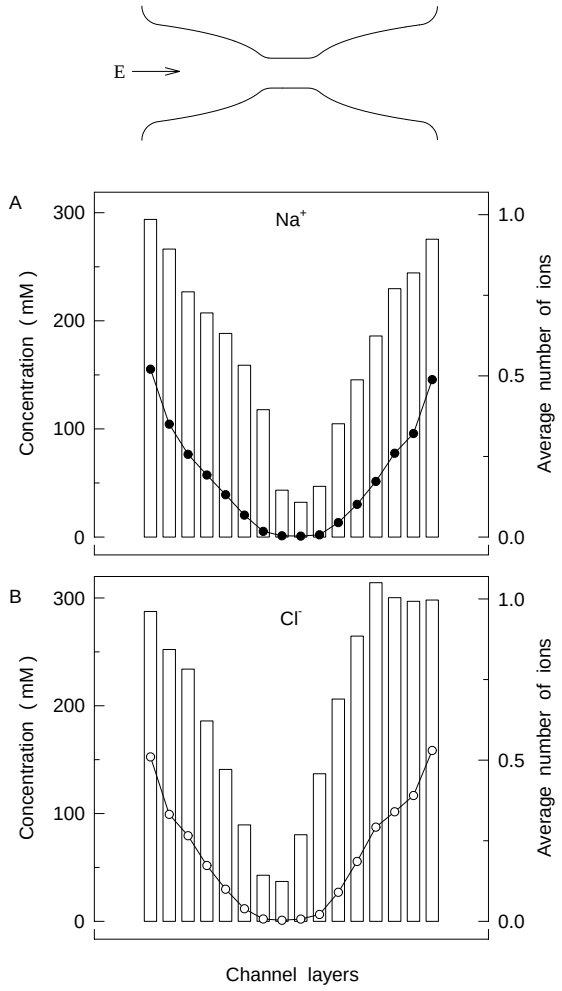

Figure 7.5: Concentrations of sodium and chloride ions in the channel in the presence of a membrane potential E. When a membrane potential of 100 mV was applied, as shown in the inset, there was a small increase in the concentration of sodium ions in the left-hand side vestibule (A) and a similar but slightly larger increase in chloride ions in the right-hand side vestibule (B). The difference is due to the larger diffusion coefficient of chloride ions compared to that of sodium ions.

left-hand side, there was a small but consistent increase in the concentration of sodium ions in the left vestibule and in the concentration of chloride ions in the right vestibule (Fig. 7.5). Other than this small asymmetry in the concentrations and a slight increase in the probability of ions being present in the constricted segment, the applied field had little effect on the average concentrations in the channel. A drastic change in the pattern of charge densities occurred when, instead of applying an electric potential across the channel, two rings of dipoles were placed on the channel wall. As shown Fig. 7.6, there was a marked increase in the concentration of sodium ions in the constricted region of the channel. Sodium ions entering the channel occasionally would become detained in the potential well created by the dipoles on the wall. Some ions travelled from one well to the other and drifted across to the other side, but because there was no potential gradient, the number of ions drifting in one direction (11.7 ± 1.3 pA) was about the same as that in the opposite direction (10.7 ± 1.3 pA).

To mimic the concentration gradient in the channel during its open state, we placed an energy barrier of 1.5 kT_r at the constricted segment and applied a membrane potential of 100 mV. As shown in Fig. 7.7, the sodium concentration in all layers of the channel was approximately constant under these conditions and ions steadily moved from outside to inside, without being detained by the dipoles on the channel wall. In contrast, chloride ions were virtually excluded from entering the inside of the channel (Fig. 7.7 B). The conductance of the channel under this condition was 78 ± 4 pS at 150 mM (or 15.5 ± 0.7 pA at 300 mM), and no sodium ions traversed against the potential gradient.

7.4.3 Current-Voltage Relationships

The current-voltage relationships obtained from excised single channels are in general ohmic, although some show pronounced inward or outward rectification. The reversal potential observed in asymmetric ionic solutions closely matches that predicted by the Nernst equation. Here we show how the presence of an energy barrier in the channel can distort the linear current-voltage relation.

The current increased linearly with the applied voltage, as shown in Fig. 7.8 A, when there was no additional potential barrier in the channel presented to ions for penetrating the transmembrane segment. In this and all subsequent current-voltage curves, we used the total strength of 4 dipoles in each ring of 100×10^{-30} Cm. The core conductance of the channel, deduced from the regression line of the form, $I = \gamma\, V$, fitted through the data points, was 232 ± 4 pS (or 116 pS at 150 mM). When an energy barrier of 3.0 kT_r was erected at the entrance of the constricted segment, the current was attenuated, but not by a constant proportion at all voltages. For example, the currents in the absence and presence of this barrier at

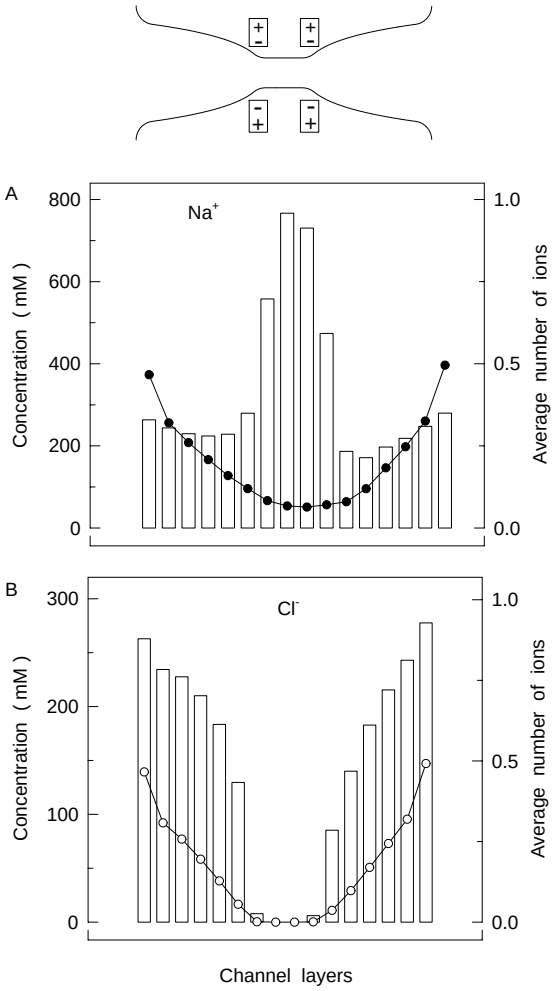

Figure 7.6: Concentrations of sodium and chloride ions in the channel in the presence of two dipole rings. Each dipole ring, with the total moment of 100×10^{-30} Cm, was placed in the positions indicated in the inset. There was a large increase in the concentrations of sodium ions in the innermost sections of the channel (A). In contrast, chloride ions were excluded from the innermost sections (B).

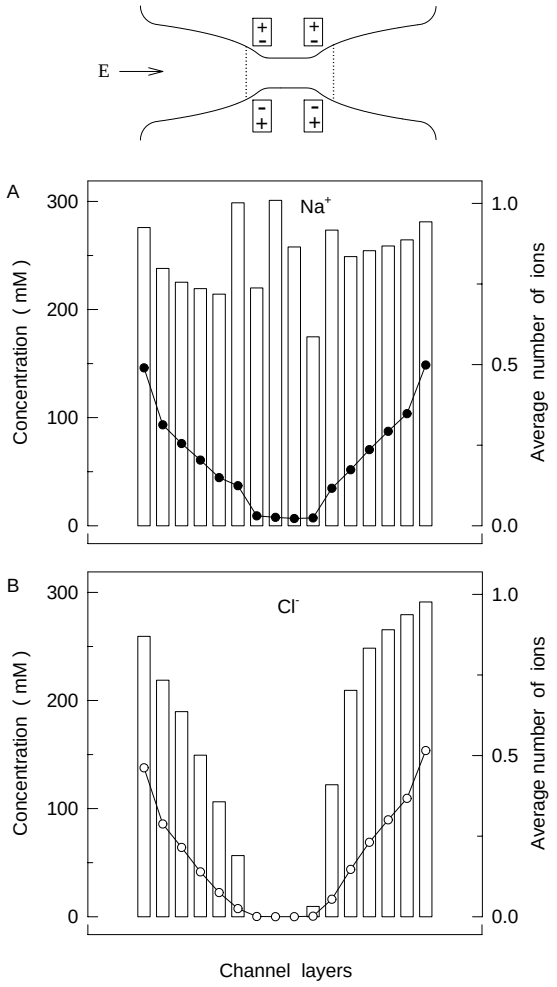

Figure 7.7: Concentrations of sodium and chloride ions in the presence of dipoles and an applied electric field. Two potential barriers of 1.5 kT_r were placed at the positions indicated in the inset. With two rings of dipoles canceling the repulsive dielectric force and a driving force provided by a membrane potential of 100 mV, sodium ions steadily traversed the channel. The concentrations of sodium ions in all sections of the channel remained approximately constant (A). In contrast, chloride ions were virtually excluded from the transmembrane sections (B).

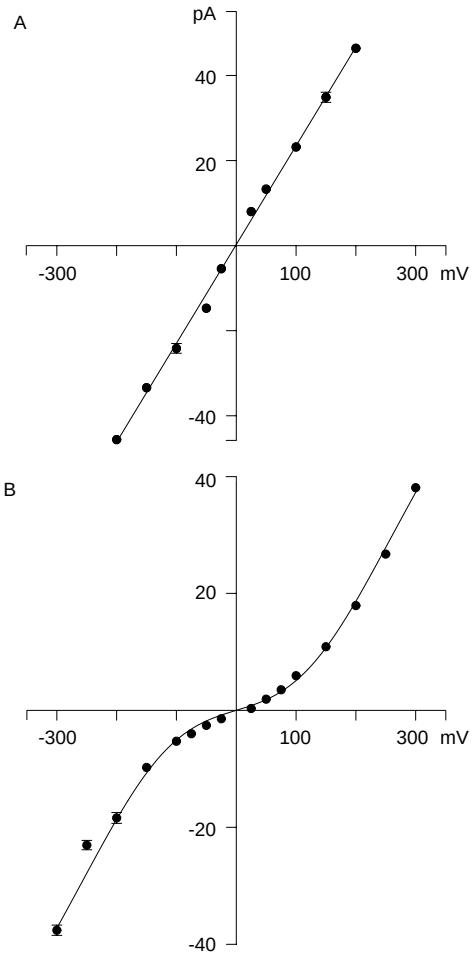

Figure 7.8: Current-voltage relationships obtained with symmetrical solutions. (A) The currents flowing across the channel that had no potential barrier near the entrance of the transmembrane segment were measured at different applied potentials. Two rings of dipoles, each ring with the strength of 100×10^{30} Cm, were placed on the channel wall. The current-voltage relationship obtained under these conditions is ohmic. The slope of the line drawn through the data points is 232 ± 4 pS. (B) When potential barriers 3.0 kT_r was erected, the current-voltage relationships became nonlinear. The data points were fitted with a modified Ohm's law which takes the barrier into account (see Eq. (7.1). The values of γ and β used to fit the curve were, respectively, 142 ± 4, and 3.5 ± 0.4. The simulation period used to obtain each data point was 1 μs.

200 mV were, respectively, 46.0 pA and 18.2 pA (39.6%). With the applied potential of 50 mV, however, the current was reduced from 14.0 pA to 2.2 pA (15.7%), thus indicating that the barrier of the same height became less of an impediment when the driving force was large. With a 3.0 kT_r barrier, the current-voltage relationship became nonlinear, deviating markedly from Ohm's law, as shown in Fig. 7.8 B. The solid line fitted through the data points in Fig. 7.8 B was calculated from the Pöschl-Teller function of the form, $I = \gamma\ V/[1 + \beta\ \text{sech}\ x]$, where $x = eV/V_B$ and V_B is the barrier height. The justification for fitting the data with this function is given in section 7.2.1. The values of γ and β used to generate the curves shown in solid lines are given in the figure legend.

7.4.4 Conductance-Concentration Curve

Experimentally, current across a biological ion channel increases monotonically with an increasing ionic concentration initially and then saturates with a further increase in concentration [31]. Saturation of channel currents occurs when there is a rate-limiting permeation process that is independent of ionic concentrations. For example, an ion arriving near the constricted membrane segment will be detained there for a period of time if, before traversing the narrow pore, it needs to gain sufficient kinetic energy to climb over an energy barrier. The reason for the presence of such a barrier is explained in the section 7.1.3.

In Fig. 7.9, the conductance of the channel is plotted against the concentrations of sodium ions in the reservoirs. The two reservoirs contained an equal number of sodium-chloride pairs, and an applied membrane potential of -100 mV provided the driving force for sodium ions to move inward. The presence of 2 rings of dipoles, with their negative poles pointing to the lumen, ensured that the channel was selectively permeable to sodium ions. When the channel had no potential barrier, the ionic current carried by sodium ions increased linearly with concentration, as shown in Fig. 7.9 A. Since the magnitude of the current in this series of simulations was large, we used the total simulation period of 0.225 μs for each point shown in Fig. 7.9 A. The linear conductance-concentration relation became distorted when a barrier was placed at 5 Å from each end of the cylindrical pore. Figure 12B illustrates the conductance-concentration curve obtained from the channel with a step potential barrier of 3.0 kT_r. The ordinate of Fig. 7.9 B is expanded, since the currents were greatly attenuated by the presence of the barrier. At a low ionic concentration, the conductance was nearly proportional to the ionic concentration. As the ionic concentration was increased, however, the conductance increased less with increasing concentrations. We fitted the points with the curve calculated from the Michaelis-Menten equation of the

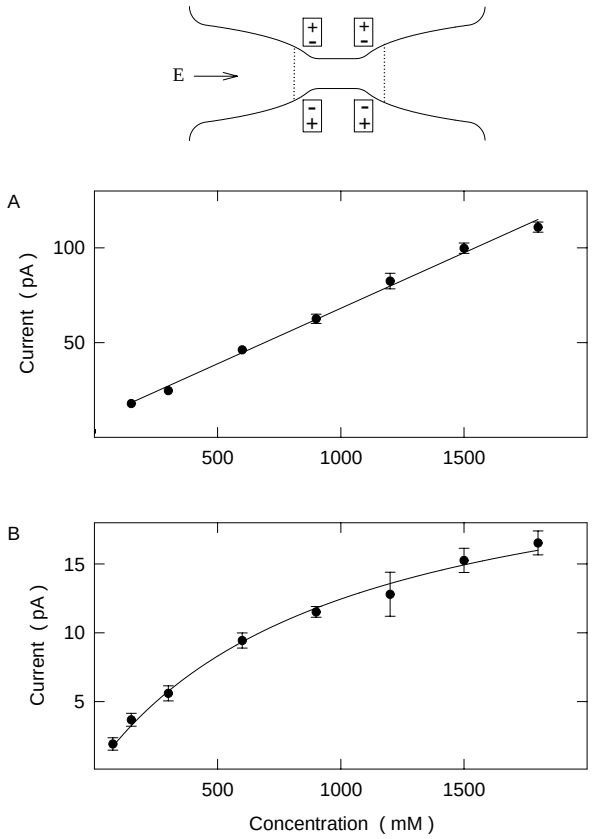

Figure 7.9: Conductance-concentration curve. The ionic concentrations in the two reservoirs were systematically increased while keeping the strength of dipoles and an applied membrane potential constant at 100×10^{-30} Cm and 100 mV, respectively. The number of ion pairs in each reservoir, with the radius of 30 Å, ranged from 3 (for 75 mM) to 78 (for 1,800 mM). (A) With no barrier present, the current increased linearly with ionic concentrations. Each point represents the average of 9 trials, each trial lasting 250,000 time steps or 0.225 μs. (B) When a step barrier, whose height was 3.0 kT_r, was erected at 5 Å from the entrance of the transmembrane segment, the conductance-concentration relation became nonlinear. The current increased linearly with an increasing ionic concentrations at first and then began to saturate. The data points of (B) were fitted with Eq. (7.7). The simulation period for each point in (B) were 1 μs, except for those representing 1.2, 1.5 and 1.8 M, for which the simulation periods of 0.3 μs were used.

form

$$I = \frac{I_{\max}}{1 + K_s/[c]} \tag{7.7}$$

where $I_{\max}$ and K_s are the fit parameters. For the solid line drawn through the data points of Fig. 7.9 B, the numerical values of these two parameters are $I_{\max} = 25 \pm 5$ pA and $K_s = 996 \pm 351$ mM. In section 7.2.2, we give a possible physical interpretation of Eq. (7.7).

7.5 Discussion

The idea that dipoles are needed to allow free permeation through the model channel is confirmed by the results in this chapter, with the proviso that some current flows even without dipoles. In the absence of dipoles permeation through the channel is severely retarded: the conductance is around 20 pS as compared to a maximum of around 175 pS with dipole rings (Fig. 7.3). This reduction in conductance can be attributed to the electrostatic energy barrier created by the dielectric boundary in the absence of dipoles (Fig. 7.2). This barrier reduces the concentration of ions in the neck region to around 40 mM, compared to 300 mM in the reservoirs (Fig. 7.5). However, when dipole rings are added the energy barrier is replaced by an energy well (Fig. 7.2), the concentration in the neck region increases to around 750 mM (Fig. 7.6), and a substantial current can flow (Fig. 7.3). The results of the long simulations confirm the picture hinted at by the ion trajectories of the previous chapter, but add detail and provide quantitative predictions.

These results also give support to another explanation for the presence of ions in the neck region of channels: that they serve to increase the concentration of ions in the neck, increasing conductance in the narrowest part of the channel, so overcoming a bottle-neck and producing a channel with a large conductance [31]. Even the small energy well created by 100×10^{-30} Cm dipole rings increases the concentration of cations in the neck region to 2.5× the bulk concentration. Dipole rings of 200×10^{-30} Cm strength produce a much bigger well and increase conductance from 115 pS to 175 pS. However, increasing dipoles beyond this strength does not increase conductance, and actually reduces it slightly for strengths of 400×10^{-30} Cm or more (Fig 7.2). The two explanations for the dipoles need not be mutually exclusive: it is quite possible that dipoles in the neck region of a channel serve firstly to overcome the membrane energy barrier and allow conductance, and secondly to increase ion concentration in the narrowest part of the channel and increase conductance through this bottle-neck. Indeed if permeation through the channel is considered to be one-dimensional, and entropy is included, then the narrow neck region becomes an entropic barrier in addition to the electrostatic membrane barrier, and dipoles are needed to overcome

the combined barrier. This may explain why increasing the strength of the dipoles beyond a certain point does not increase conductance. Note that the simulations are three-dimensional, so that the entropic effects of a narrowing channel emerge implicitly from the motion of the ions, and do not need to be included explicitly.

Shielding by counter-ions seems to be having some effect, but does not completely remove the electrostatic barrier. This can be seen by comparing concentrations in the neck region with the electrostatic energy profiles. Without dipoles the height of the barrier is around 4 kT which, by applying the Boltzmann factor, would suggest a dilution to 1/50 bulk concentration or around 6 mM for both cations and anions. In Fig. 7.4, however, the concentrations are around 20 mM, suggesting that shielding has reduced the barrier by about 30%. Dipoles of 100×10^{-30} Cm create a well of around 2.5 kT, which should increase their concentration by a factor of 12, but Fig. 7.6 shows that the increase is only by a factor of 2.5, suggesting that interactions with other ions have reduced the depth of the well to about 1 kT. Fig. 7.5 is interesting, in that the applied field reduces the height of the barrier to 2 kT (Fig. 7.2), which by the Boltzmann factor suggests a concentration of around 40 mM, which is what is seen in the figure. This might indicate that shielding has a much smaller effect when current is flowing and ions are moving through the channel, but it is difficult to be sure, as the use of the Boltzmann factor is inappropriate in this non-equilibrium situation.

Without an additional energy barrier both current-voltage (Fig 7.8) and conductance-concentration (Fig 7.9) curves are linear, indicating that ions navigate the channel independently, without multi-ion interactions playing an important role. When an sharp energy barrier is added in the neck region both curves become non-linear. The conductance-concentration curve shows saturation with increasing concentration, and can be fitted to the Michaelis-Menten equation. The current-voltage curve shows a particular pattern of non-linearity, with a switch from a region of lower conductance to one of higher conductance at around 100 mV of applied potential. This curve can be fitted to a Pöschl-Teller function, as described in section 7.2.1. Thus, without an energy barrier the model is of a high-conductance single ion channel with linear conductance characteristics, while with energy barriers the model predicts a lower conductance and specific types of non-linearity.

Chapter 8

Multi-Ion Channel

In this chapter we describe the construction of an approximate model of a potassium channel and its use to perform BD simulations. The model is based on the structure of the KcsA channel as described by Doyle et. al. [21]. This is done with the primary aim of seeing if it is possible to build a working model of a multi-ion channel using only a diffusive mechanism. A secondary aim is to test the plausibility of some of the conductance mechanisms proposed by Doyle et. al., but since these mechanisms are deduced in a quite straightforward way from the experimental structure, this might equally be regarded as a test of the plausibility of our model and techniques.

Although their gating characteristics differ, most potassium channels show similarities in amino acid sequence, conductance characteristics, selectivity, and blocking agents. These common characteristics identify them as a group and strongly suggest a common pore structure. Thus, even though KcsA is a bacterial channel, its structure can be taken as representative of the pore structure of all the potassium channels with similar characteristics. The conductance characteristics of potassium channels, specifically ionic flux coupling and saturation at high concentrations, are strong evidence that potassium channels contain between 2 and 3 ions when conducting. They are also taken as evidence that potassium channels contain binding sites, and that conductance is by hopping between these sites, with any diffusion that occurs being irrelevant or incidental (see chapter 14 of Hille [31]). This is because the theories that best describe these characteristics (RRT and the Michaelis-Menten mechanism) are theories about chemical reactions which, as applied to enzymes, involve the binding of a substrate to an enzyme. The explanation in terms of binding sites is reasonable, given that no diffusion based theory has been able to adequately explain conductance in multi-ion channels, but it does not take into account the theoretical problems with RRT as applied to channels (see section 2.1), and does not explain the far greater turnover rate of channels compared to enzymes and carriers (see section 1.2 and chapter 11 of Hille [31]). By attempting to build a diffusion

based model of a multi-ion channel we hope to shed some light on this issue.

The structure of the KcsA channel contains several clues to its conductance mechanisms [21]. At the top (extracellular) end of the channel is a very narrow, 12 Å long section of pore lined by hydrophilic protein backbone much like a gramicidin pore, although the protein chains are straight, not arranged in a helix. This is recognizably a selectivity filter and must hold the key to explaining the extreme selectivity of potassium channels. Doyle et. al. suggest a possible mechanism, but this cannot be investigated by the techniques described here, as macroscopic electrostatics completely ignores the subtle close-range interactions essential for selectivity between ions of the same valence (see section 1.2). The x-ray crystallography used to find the structure of the channel also shows the preferred positions of ions in the pore. There are two such positions in the selectivity filter, located near each end, 7.5 Å apart. These could be interpreted as binding sites, specific locations with a high affinity for potassium ions, but this does not readily explain the high conductance of the channel, as a hop of 7.5 Å (carrying the intervening water with it) seems unlikely, and the selectivity filter is too narrow for diffusion to be considered irrelevant. The interpretation of Doyle et. al. is different: they suggest that the whole selectivity filter has a high affinity for potassium ions, and would trap a single ion, preventing conductance. However, the two ions in the filter destabilize each other by electrostatic repulsion (hence their locations near the ends of the filter), and this allows ions to escape and conductance to occur. We test the plausibility of this mechanism in our BD simulations by placing small dipoles representing carbonyl groups around the model selectivity filter. This creates the necessary high affinity for cations, and transport is provided by the simulated diffusion of the BD motion algorithm.

This model of the selectivity filter may be quite unrealistic. The real carbonyl groups have some freedom to move, a hydrogen bond is not completely representable as a dipole interaction, and calculations by macroscopic electrostatics in such a confined space can be no more than an estimate. The selectivity filter may be more like a series of 4-6 connected binding sites than a continuous attractive region, transport might be through a series of short hops rather than by diffusion, and the single file nature of the filter means that ions and water should move in a coordinated manner, whatever the transport mechanism. All of these issues need to be studied using MD or similar microscopic simulation techniques. However, despite these reservations, and crude as it is, the BD model captures the essential features of the proposed mechanism: a selectivity filter with a high affinity for ions, and mutual destabilization by long-range electrostatic repulsion.

Below the selectivity filter lies a central cavity, and below that an inner pore leading to the cytoplasmic mouth of the channel. The central cavity is an elongated spheroid, about 10 Å across and 12 Å long. The inner pore is around 18 Å long and wide enough for a potassium ion to move

through 'and still remain mostly hydrated' [21]. The linings of both of these regions are predominantly hydrophobic, which raises the question of how the electrostatic barrier created by the membrane is overcome. Doyle et. al. propose mechanisms to reduce the barrier. They suggest that the central cavity and inner pore provide water to surround the ion and thus reduce the barrier, while the hydrophobic walls do not interact greatly with the ion, allowing it to diffuse without impediment. The wider cavity is in the centre of the pore, providing the most hydrating water where the barrier is greatest. They also observe that the pore helices (four short alpha helices that support the selectivity filter) point directly towards the central cavity and (as do all alpha helices) posses significant dipole moments. The negative ends of these large dipoles are closest to the central cavity, and thus they are expected to attract cations. Another preferred ion position is located at the centre of the cavity, although it is more diffuse than the ones in the selectivity filter: this supports the idea that the water filled cavity and helix dipoles overcome the membrane barrier and create instead an energy well which attracts ions. Doyle et. al. point out that this preferred ion position in the cavity does not represent a binding site in the conventional sense, but rather 'a hydrated cation cloud'.

Three-dimensional BD seems well suited to the task of investigating conductance in the inner pore and central cavity. The mechanism that Doyle et. al. propose for transport in this region is diffusion, with the electrostatic barrier overcome by a combination of shielding by water molecules and long range electrostatic interactions with the channel structure. These are exactly the physical phenomena that the methods described in this thesis are designed to reproduce (although the accuracy of this reproduction may be far from perfect due to the use of macroscopic electrostatics and other simplifications). This region of the channel represents around 70 percent of its length, and if Doyle et. al. are right about the purpose of the central cavity and helix dipoles, is relevant to the channel's conductance. Of course the conductance of a channel depends on its entirety, not just particular regions, so the selectivity filter must be included in any simulation expected to reproduce conductance. Although our model of the selectivity filter is necessarily crude, and other techniques are better suited to investigating this region of the channel, the conductance mechanism proposed by Doyle et. al. is not incompatible with a BD simulation or macroscopic electrostatics.

8.1 Model

This model was derived from the structural descriptions and figures in the paper by Doyle et. al. [21], not the molecular coordinates: at the time it was built we did not have the ability to analyze such coordinates to produce a model.

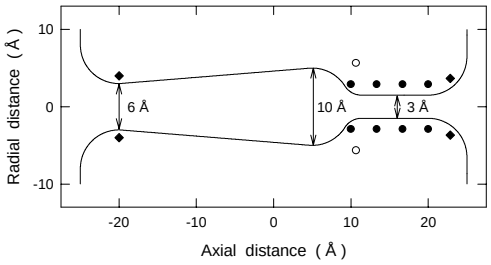

Figure 8.1: Idealized potassium channel. The channel shape is generated by rotating the curves outlined along the symmetry z-axis by 180°. The positions of the negative ends of the dipoles in the channel wall are indicated: filled circles show 8 of the 16 carbonyl oxygen atoms; open circles the helix dipoles, and filled diamonds, the mouth dipoles.

8.1.1 Shape of the Channel

The shape of our model channel is a simple, geometric representation of the pore structure (see Fig. 8.1). The three-dimensional shape of the channel is generated by rotating the curves shown around the symmetry axis (z axis) by 180°. The total length of the model channel is 50 Å, compared to 45 Å for the real channel. The model channel is slightly longer due to the need to add curved sections at each mouth of the channel (the iterative method of solution does not deal well with sharp corners). These curves are quarter circles with a radius of 5 Å.

The selectivity filter is represented by a cylindrical section 1.5 Å in radius and 10 Å long. The real selectivity filter is around 12 Å long, but in our model the inner 2 Å of the curved extracellular mouth is very narrow (maximum radius 1.9 Å), and can be regarded as part of the filter. The radius of the selectivity filter is deduced from the ions that can pass through it (see chapter 13 of Hille [31]). Potassium ions (radius 1.33 Å) can pass through easily, as can rubidium ions (radius 1.48 Å). Caesium ions (radius 1.69 Å) can enter the filter but tend to get stuck: presumably some areas of the filter are wider than others, and the filter has some flexibility. For our

very simplified model for use with BD, 1.5 Å seems a reasonable average radius.

The central cavity and inner pore are represented in our model by a hemisphere and a truncated cone. The hemisphere has a radius of 5 Å, corresponding to the 10 Å width of the central cavity. The truncated cone is 25 Å long and has a radius of 5 Å where it meets the hemisphere reducing to 3 Å where it meets the cytoplasmic mouth. The cytoplasmic mouth of the channel admits tetraethylammonium (TEA) ions to the inner pore when the channel is open [21]. This suggests a width of at least 5-6 Å, since a TEA ion (chemical formula $(CH_3)_4N^+$) consists of four carbon atoms in a tetrahedron bonded to the central nitrogen atom, and carbon atoms have a hard-sphere radius of 1.4 Å. The total length of hemisphere and cone is 30 Å, corresponding to the total length of central cavity (12 Å) and inner pore (18 Å) in the real channel.

Small curved sections join the selectivity filter, hemisphere, truncated cone, and cytoplasmic mouth without sharp corners. In our coordinate system the model channel runs from $z = -25$ Å on the cytoplasmic side to $z = 25$ Å on the extracellular side. The narrowest point in the inner pore is at $z = -20$ Å, the centre of the cavity is at $z = 5$ Å, and the selectivity filter runs from $z = 10$ Å to $z = 22$ Å.

8.1.2 Dipoles

The positions of fixed charges and dipoles in our model are based, where possible, on the structure described by Doyle et. al. We regard their strengths as adjustable parameters, however. This is done in order to give the model flexibility to cope with the possible inaccuracies in the calculation of energy barriers and wells which might arise due to the use of macroscopic electrostatics. We place four sets of dipoles in the model protein wall, each with four-fold symmetry around the z axis. Two of these sets are mouth dipoles, representing the negative charges at each entrance of the channel reported by Doyle et. al. [21]. The negative ends of these dipoles are placed at $z = 22.83$ Å and $z = -20$ Å, just inside the protein wall (filled diamonds in Fig. 8.1). For each mouth dipole we place a counter-charges 5 Å further in, but this is a guess, as it is not clear from the descriptions or diagrams in the paper whether there are counter-charges for the negative charges near the channel entrances, or if so where they are. The third set are the helix dipoles, representing the dipole moments of the pore helices. The position and orientation of these dipoles is known from the structure: their negative ends are 8 Å from the centre of the cavity (open circles in Fig. 8.1), they are aligned at 45° from the channel axis, and they point directly towards the centre of the cavity [21]. Their length can be deduced to be 16 Å based on number of residues in each helix. The fourth set are the carbonyl dipoles, representing the carbonyl groups that line the selectivity filter. As explained

above, these are only a rough approximation of the hydrophilic lining of the filter. Four carbonyl dipoles are placed along the selectivity filter, spaced evenly along a distance of 10 Å and oriented perpendicularly to the z axis. With the four-fold symmetry around the z axis this gives a total of 16 small dipoles. The dipoles are located at $z = 10$, 13.33, 16.67 and 20 Å with the negative pole of each placed 1 Å from the boundary (filled circles in Fig. 8.1), and the positive pole 1.2 Å further away. The dipole length of 1.2 Å is chosen to correspond to that typically used for carbonyl groups in MD simulations [11].

8.1.3 Brownian Dynamics

We use our multiple time step algorithm (see section 7.3.2) to simulate the motion of ions more accurately and allow non-reflective repulsion from the walls in the narrowest regions of the pore. A short time step of 2 fs is used in the mouth regions of the channel and the selectivity filter. A long time step of 100 fs is used elsewhere. Specifically, there are two short time step bands, $-25 < z < -15$ and $7.5 < z < 25$, comprising both entrances and the selectivity filter. If an ion is in one of these bands at the beginning of a 100 fs period, it is simulated by 50 short steps instead of one long step; so synchronization between the ions is maintained. Long-range forces are calculated normally at the start of the 100 fs period, and are assumed to be constant throughout. Short range forces are calculated every 2 fs. Coulomb interactions between ions are calculated at the start of each long time step except where both ions are in the same band, when they are recalculated for each 2 fs step. Forces due to the Born energy barriers described in the next section are also calculated every short time step.

The short range forces represent the repulsion that occurs when electron clouds overlap. They are approximations, primarily intended to prevent ions from interpenetrating each other or the protein walls, but they do provide more accurate motion than the reflection algorithm which serves this purpose in the long time step regions. We do not expect that short range forces have a large role in conductance in the inner pore and central cavity, as these regions have a hydrophobic pore lining. Short range forces obviously *are* important in the selectivity filter, but our techniques cannot reproduce them accurately, so we must be content with a crude model of this region. As explained above, even such a simplified model may well be useful.

The ion-ion interaction is given by the potential function

$$U_{II}(r_{12}) = \frac{F_0}{9} \frac{(R_1 + R_2)^{10}}{r_{12}^9}, \tag{8.1}$$

where r_{12} is the ion-ion distance, R_i, $i = 1, 2$, are the Pauling radii of the ions and F_0 is the magnitude of the short range force at contact. For the

ion-protein wall potential U_{IW}, a similar form is used

$$U_{IW}(r) = \frac{F_0}{9} \frac{(R_i + R_W)^{10}}{(\rho(z) + R_W)^9}, \tag{8.2}$$

where R_W is the radius of the atoms making up the wall and $\rho(z) = R_C(z) - r$ is an estimate of the distance from the ion to the channel wall, r being the radial coordinate of the ion and $R_C(z)$ being the radius of the pore at the ion's z coordinate. We use $R_W = 1.4$ Å (the Pauling radius of a carbon atom) and $F_0 = 2 \times 10^{-10}$ N (estimated from the ST2 water model used in molecular dynamics [69]).

8.1.4 Dielectric Constant

Conditions in the pore may be quite different from those in a bulk electrolyte solution (see section 3.1.4) so we regard the dielectric constant in the pore as an adjustable parameter. Unfortunately, due to the limitations of our iterative method, the dielectric constant for the model water must be the same throughout the simulation: the dielectric constant can only change at dielectric boundaries, and the iterative method does not give meaningful results if an ion crosses such boundaries. This means that when we reduce the dielectric constant in the pore, the dielectric constant in the reservoirs is also reduced, whereas in reality it should probably be close to the bulk value. One consequence is that the energy barrier due to the ion moving from a high dielectric strength region (the reservoir) to a lower one (the pore) is not reproduced by our electrostatic calculations.

In an attempt to compensate for this omission, we add an extra energy barrier in the form of a step at each entrance of the channel. The height of this energy barrier is given by the Born energy (see section 3.1.2)

$$E_{\mathrm{B}} = \frac{q^2}{8\pi\epsilon_0 R_{\mathrm{B}}} \left(\frac{1}{\epsilon} - \frac{1}{80} \right). \tag{8.3}$$

We use $R_{\mathrm{B}} = 1.93$ Å which is derived from the estimated enthalpy of hydration for K^+ ions [10]. The shape of the potential step is given by the smooth switching function

$$U_{\mathrm{B}}(s) = (E_{\mathrm{B}}/16)(3s^5 - 10s^3 + 15s) + (E_{\mathrm{B}}/2), \quad s = \frac{z - z_c}{\Delta z}, \tag{8.4}$$

which has continuous first and second derivatives and rises gradually from 0 to E_{B} as s changes from -1 to 1. Here, $z_c = \pm 22.5$ Å is the location of the center of the profile and $\Delta z = \mp 1.5$ Å is its half-width. To give an indication of the barrier heights involved, we note that for $\epsilon = 20$, 40 and 60, $E_{\mathrm{B}} = 5.4$ kT, 1.8 and 0.6 kT, respectively.

8.2 Methods

8.2.1 Energy Profiles

In the results section we calculate both single-ion and multi-ion energy profiles. The potential profile of an ion is constructed by solving Poisson's equation with the ion fixed at a series positions spaced at 1 Å intervals along the z-axis. This is done using the lookup tables in the same way as in the BD simulations. This is a simple process for a single-ion profile, but the channel contains more than one ion while it is conducting, and so we need to be able to calculate energy profiles in the presence of additional ions.

To visualize the shape of the energy barrier an ion encounters as it attempts to enter a channel that is occupied by one or more ions, we have constructed multi-ion energy profiles. We move one of the ions from the intracellular space into the channel in 1 Å steps, holding it fixed at each step. We then allow the other ions in the selectivity filter to adjust their positions so that the force on them will be zero, thus minimizing the total energy of the system. The minimization is performed at each step and the positions of the ions and the total energy are recorded. The total energy corresponds to the total electrostatic energy required to bring in the charge on the ions from an infinite distance in infinitesimal amounts, and it is given by

$$U_{\text{total}} = \sum_i \frac{q_i}{2} \left[2V_{\text{X},i} + V_{\text{S},i} + \sum_{j \neq i} (V_{\text{I},ij} + V_{\text{C},ij}) \right] + U_{\text{B},i}, \tag{8.5}$$

where the indices i and j range over all the ions. The potential terms in Eq. (8.5) are described in section 6.1 and section 8.1.4. The factors of $1/2$ in the middle three terms arise from the integration of charge during build up. Using a modified version of the steepest descent algorithm (see [58]), the total energy of a multiply-occupied channel given in Eq. (8.5) is successively minimized until the forces on the free ions vanish.

8.3 Results

8.3.1 Dipoles and Energy Profiles

As an ion approaches the boundary between an aqueous solution and the protein wall, it experiences an electrostatic repulsion due to induced charges at the boundary. In computing the potential energy of an ion as it moves along the central axis, we assume initially that the dielectric constant ϵ in the reservoirs and the pore is 60. The energy of transition from bulk water, estimated from the Born energy, is incorporated as a potential barrier at the channel entrance as explained in the section 8.1.4.

In the absence of any charge moieties on the protein wall, an ion attempting to traverse the channel encounters a significant energy barrier.

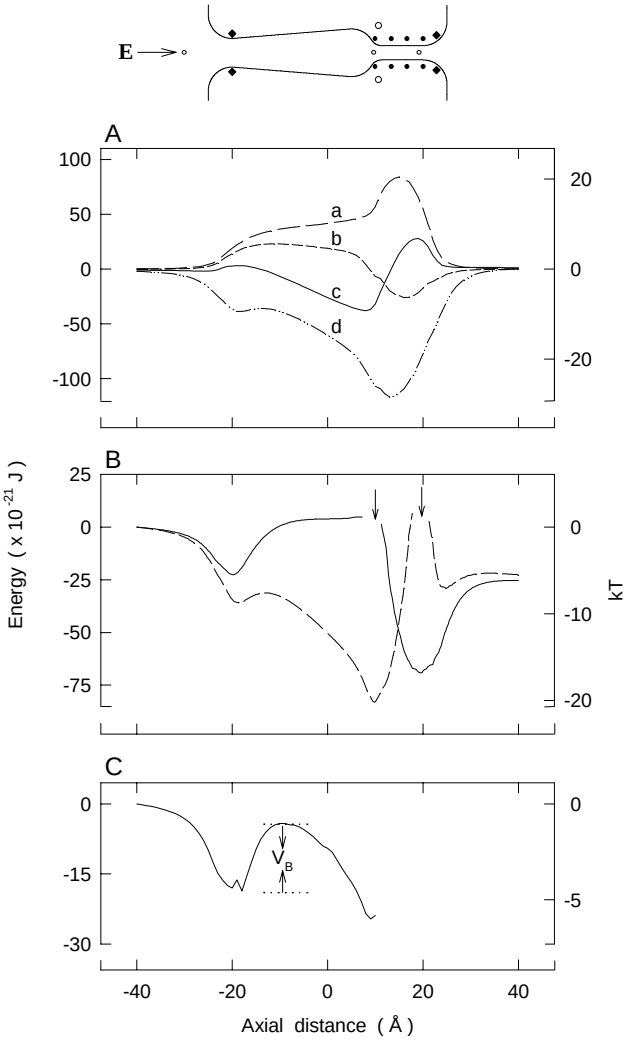

Figure 8.2: Electrostatic energy profile of a potassium ion traversing the channel. (A) The potential energy of an ion along the central axis. The profile **a** is the potential energy seen by the ion, in the absence of any charge moieties on the channel wall, profile **b** is obtained with 4 sets of 4 carbonyl groups (filled circles in the inset), profile **c** is obtained with 4 helix macrodipoles (open circles in the inset), and profile **d** is obtained with the carbonyl groups, helix dipoles and 2 rings of mouth dipoles (filled diamonds in the inset). (B) Potential profiles seen by individual ions while the other is fixed at the equilibrium position (indicated by arrows). The applied field corresponds to a potential difference of about 150 mV between the channel entrances. The first ion is placed at the equilibrium position $z = 10$ Å and the profile seen by the second ion is computed (solid line). The second ion is now placed at $z = 19.75$ Å and the profile seen by the first ion is computed. (C) The potential profile encountered by a third ion, as it moves from left to right. At each fixed position of the third ion, the stable configuration of the first two ions is determined iteratively and then the total energy of the assembly is computed. The strengths of each carbonyl group, mouth dipole and helix dipole are, respectively, 7.2, 30 and 96.3 $\times 10^{-30}$ Cm.

The potential energy at a fixed position of an ion is computed numerically and the calculation is repeated at 1 Å intervals. The profile presented to the ion as it moves from inside (left) to outside (right) increases slowly at first and then rises steeply in the narrow selectivity filter, reaching a peak of 20 kT, as shown in Fig. 8.2 A (curve labeled **a**). Four rings of dipoles, with 4 carbonyl groups in each ring, placed along the selectivity filter, transform a section of the barrier into a well (**b**) as do 4 helix dipoles placed just below the selectivity filter (**c**). As it will be shown later, two sets of additional mouth dipoles are needed to render the channel permeable to ions. When all three sets of dipoles – 16 carbonyl groups, 4 helix macrodipoles and 8 mouth dipoles – are placed along the channel wall, the profile an ion encounters while traversing the central axis of the channel is a deep potential well (**d**).

The potential well created by the dipoles, reaching a depth of nearly 30 kT, attracts cations. An ion, upon entering the channel, will proceed towards the bottom of this well. A second ion entering the channel sees a different profile, altered by the presence of the first ion. The well in Fig. 8.2 A (**d**) is deep enough to hold two ions in a stable configuration. Through an iterative energy minimization procedure, one can determine the equilibrium positions of the pair of ions in the well. The potential profile seen by either ion while the other is fixed at the equilibrium position, in the presence of an applied field of 1.5×10^7 V/m, is shown in Fig. 8.2 B. At these positions (indicated by arrows), the z-component of the force experienced by the ions is zero. The two-ion potential profiles exhibit relatively deep wells that may attract a third ion. In Fig. 8.2 C we show the potential profile seen by a third ion moving into the channel from the left. Here the potential is calculated at a given position of the third ion after finding the equilibrium positions of the first two ions. There is a shallow well near the entrance of the channel, produced by the ring of mouth dipoles. Once in the well, the third ion will be delayed until random Brownian motion allows it to escape. We note here that the potential minimum is along the central channel axis, so that ions are preferentially funneled along it. The repulsive force from the induced surface charges swings into action whenever an ion strays from the central axis, pushing it back to the axis. The corresponding electric potential profile along the radial axis is similar in appearance to a harmonic well, except that it rises much more sharply near the boundary (see Ref. [33]).

From these electrostatic calculations, we deduce that the channel is normally occupied by two cations. Conduction is unlikely to take place unless these ions are resident in the pore to reduce the energy well created by the charge moieties.

8.3.2 Dependence of Conductance on Dipole Strengths

For the channel to conduct ions, there is a narrow range of moments various dipole groups must possess. Using BD simulations, we have determined how the magnitude of currents flowing across the channel varies with dipole strengths and the effective dielectric constant in the channel lumen.

As shown in Fig. 8.3 A, the conductance increases rapidly as the moment of each carbonyl group is increased from 0 to 7.2×10^{-30} Cm. The current begins to decline when the moment is further increased to 14.4×10^{-30} Cm. The three curves illustrated in Fig. 8.3 A are obtained by letting the effective dielectric constant of the pore be 80 (top curve), 70 (middle curve) and 50 (bottom curve). The charge placed on the terminals of each helix dipole and the strength of each mouth dipole are kept constant at 0.6×10^{-19} C and 30×10^{-30} Cm, respectively. In this and subsequent figures, unless stated otherwise, each point is the average of five simulations, each simulation period lasting for 100 ns. The error bar accompanying a data point is one standard error of means and is not shown if it is smaller than the size of the data point. Again, unless noted otherwise, 13 potassium and 13 chloride ions are placed in the left-hand reservoir (representing the intracellular space), whose volume is adjusted so as to give the ionic concentration of 300 mM, and the same number of ions is placed in the right-hand side reservoir (representing the extracellular space). The applied electric field between the two ends of the reservoirs produces a potential difference of about 150 mV, inside positive with respect to outside. The peak current is always obtained when the strength of the carbonyl groups is fixed at 7.2×10^{-30} Cm (2.16 Debye), irrespective of the assumed dielectric constant. In Fig. 8.3 B, the variation of currents with the dipole moment is determined at 3 different applied potentials, 150 mV, 200 mV and 250 mV, while keeping $\epsilon = 60$ throughout. Again the current peaks at about the same dipole strength.

The results of simulations showing the variation of current with the strengths of mouth dipoles (A) and helix dipoles (B) are illustrated in Fig. 8.4. The dipole moment of each carbonyl group in the selectivity filter is kept at 7.2×10^{-30} Cm throughout. The current flowing across the channel is largest when the charge on each of the four helix dipoles is 0.6×10^{-19} C. Similarly, the current is maximum when the strength of each of the mouth dipoles is 30×10^{-30} Cm. Fig. 8.4 reveals, as does the previous figure, that the dielectric constant of the channel has pronounced effect on the permeability of the channel. With optimum pore helix and mouth dipole strengths, $\epsilon = 60$ gives the physiological conductance of approximately 40 pS, as found experimentally [67]. The channel conductance is progressively suppressed when the dielectric constant in the pore is lowered and no conduction takes place, with the driving force of 150 mV, when $\epsilon \leq 40$.

Here and in all subsequent series of simulations, we assume that the channel possesses the strengths of various dipole groups that enables the

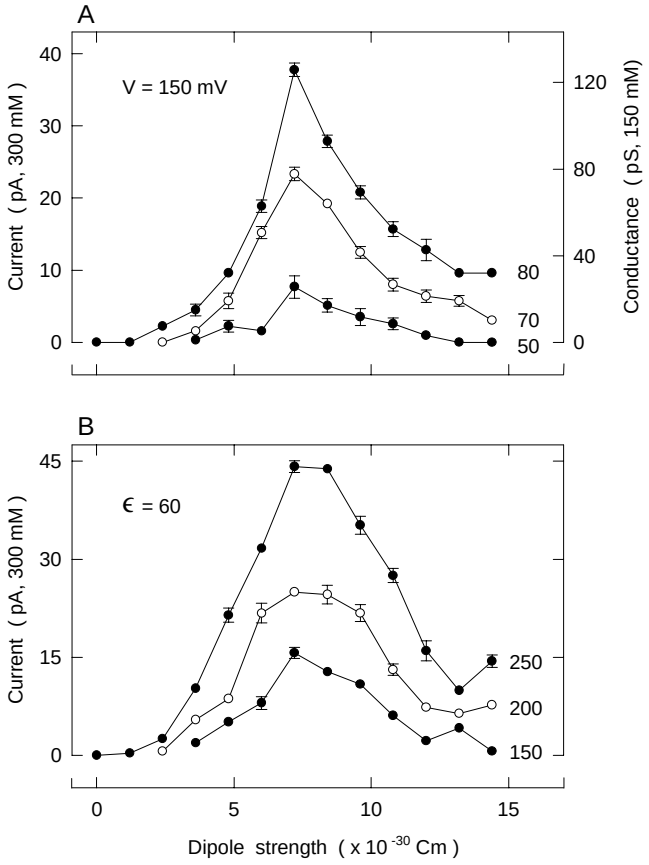

Figure 8.3: Changes in channel conductance with the strength of carbonyl groups. Simulations under various conditions, each lasting 100 ns, are repeated 5 times. The height of each reservoir is adjusted to give an ionic concentration of 300 mM, and inside is made 150 mV positive with respect to outside. The current (in pA) is determined from the total number of ions traversing the channel over the simulation period of 0.5 μs. (A) Keeping the moments of each helix dipole and mouth dipole constant at 96.3 and 30 $\times 10^{-30}$ Cm, the strength of each carbonyl group is systematically changed. The current (in pA) is plotted against dipole strength for three values of the dielectric constant, $\epsilon = 50$, 70 and 80. (B) The current is plotted against the strength of carbonyl groups for three values of applied potential, 150 mV, 200 mV and 250 mV, while keeping ϵ constant at 60.

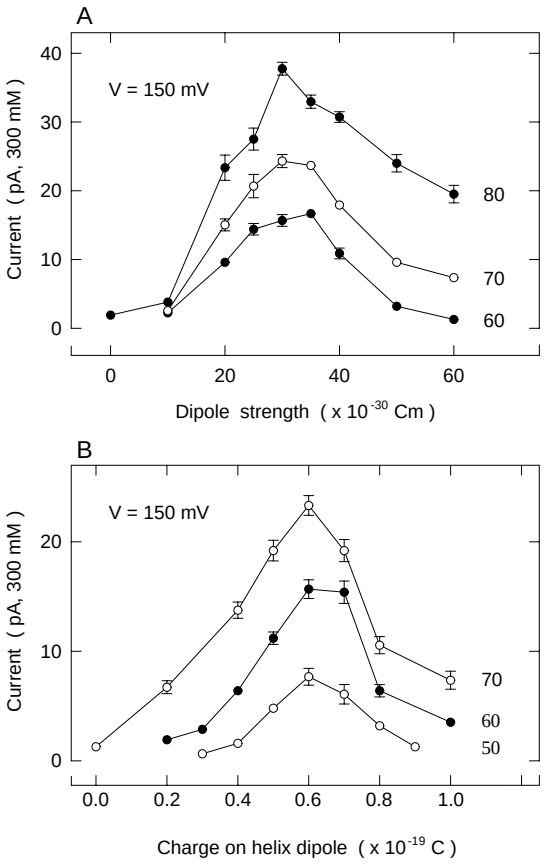

Figure 8.4: Changes in channel conductance with the strength of mouth dipoles (A) and helix dipoles (B). (A) The strength of each mouth dipole is changed systematically while keeping the moments of each carbonyl group and helix dipole constant at 7.2 and 96.3 $\times 10^{-30}$ Cm. The current is plotted against the strength of mouth dipoles for three different values of dielectric constant, $\epsilon = 60$, 70 and 80. (B) The charge placed on each helix dipole is changed systematically while keeping the moments of each carbonyl group and mouth dipole constant at 7.2 and 30 $\times 10^{-30}$ Cm. The current (in pA) is plotted against dipole strength for three values of the dielectric constant, $\epsilon = 50$, 60 and 70.

maximum number of ions to be translocated across the channel for a given driving force, that is, the dipole strengths for each of 8 mouth dipoles, 16 carbonyl groups and 4 helix dipoles are, respectively, 30, 7.2 and 96.3 $\times 10^{-30}$ Cm.

8.3.3 Effects of Dielectric Constant and Diffusion Coefficient on Currents

From the results given in the previous section, it is clear that, for the channel to conduct, the effective dielectric constant ϵ in the pore must be high. In other words, water molecules resident in the pore must not be tightly bound to the protein but be able to rotate relatively freely so as to reduce the interaction energy between the ions and the charges located on the channel wall. In Fig. 8.5, we examine further the influence of ϵ on the magnitude of current flowing across the channel. The depth of the energy well created by dipoles increases as ϵ is lowered. An example of the energy well created by four mouth dipoles located near the channel entrance, when there are two ions resident in the selectivity filter (*c.f.*, Fig. 8.2 C), is illustrated in Fig. 8.5 A. Here, ϵ is assumed to be 30 and a potential of 300 mV is applied across the channel. An ion attempting to cross this well encounters a barrier V_B, the height of which decreases monotonically with increasing ϵ, as shown in Fig. 8.5 B. Increasing the applied potential from 150 mV to 300 mV reduces the barrier height by about 1.5 kT. A steep increase in the barrier height as ϵ is lowered suggests that the channel will not conduct ions if ϵ in the pore is less than 40. The inference drawn from electrostatic calculations is in accord with the results obtained from BD simulations. The current across the channel under the driving force of 150 mV, 200 mV, 250 mV and 300 mV is plotted against ϵ in Fig. 8.5 C. These four curves broadly mirror the way the barrier height increases with ϵ. The current ceases to flow when the barrier height reaches 7 kT.

The diffusion coefficient of potassium ions D_{K} in bulk electrolyte solutions is 1.96 $\times 10^{-9}$ m^2/s. This value is reduced when an ion is diffusing through a narrow tube [64, 17, 47, 68, 5]. The magnitude of the diffusion coefficient of an ionic species depends, among others, on the radius of the cylinder and the composition of the wall. A molecular dynamics simulation of the KcsA channel [6] shows that D_{K} in the wider segment, including the oval chamber, in nearly the same as that in bulk solutions, whereas that in the selectivity filter is on average 1/3 of the bulk value. The following series of simulations are carried out to assess how much the channel conductance is suppressed by a low D_{K} in the narrow filter.

When ions enter the channel segment extending from $z = 7.5$ to $z =$ 25 Å, their motions are determined by a D_{K} that is lower than the bulk value. Fig. 8.6 shows the current across the channel as a function of D_{K} at three different values of dielectric constants, $\epsilon = 60$ (A) and $\epsilon = 50$ and 70

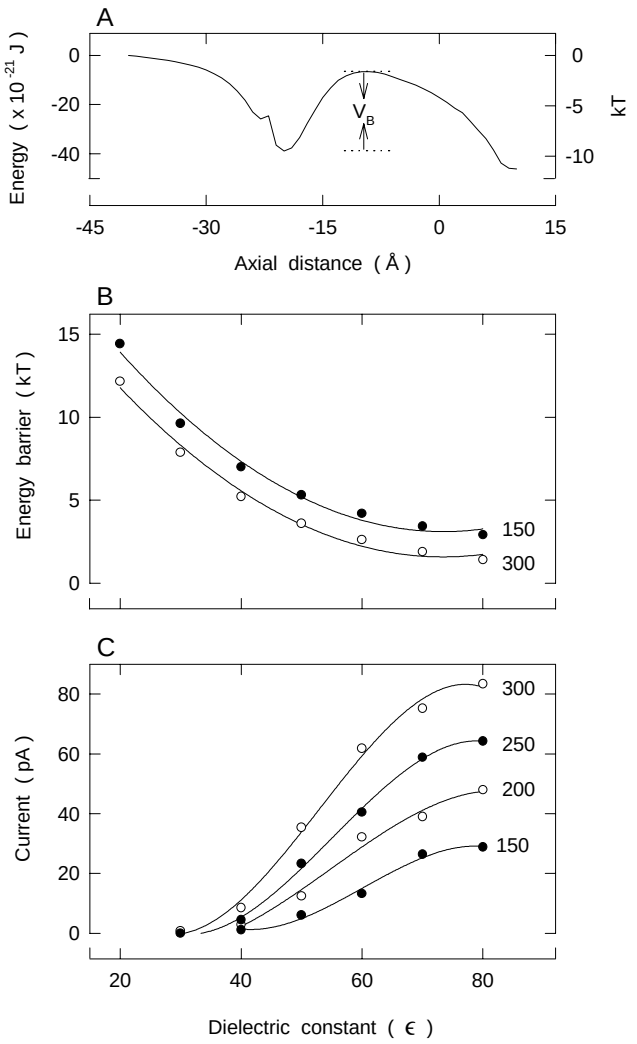

Figure 8.5: Effects of the effective dielectric constant on conductance. (A) A energy well near the channel entrance created by four mouth dipoles is encountered by an ion given that there are two resident ions in the selectivity filter. The energy minimization is carried out with $\epsilon = 30$ and an applied potential of 300 mV. An ion upon entering the well must surmount a barrier of height V_B to traverse the channel. (B) The height of the barrier V_B is plotted against the effective dielectric constant for two different values of applied potential, 150 mV (filled circles) and 300 mV (open circles). (C) The inward currents under the driving force of 300 mV (open circles), 250 mV (filled circles), 200 mV (open circles) and 150 mV (filled circles) are plotted against the effective dielectric constant. Each point is derived from a simulation period of either 1 μs (150, 200 and 250 mV) or 2 μs (300 mV).

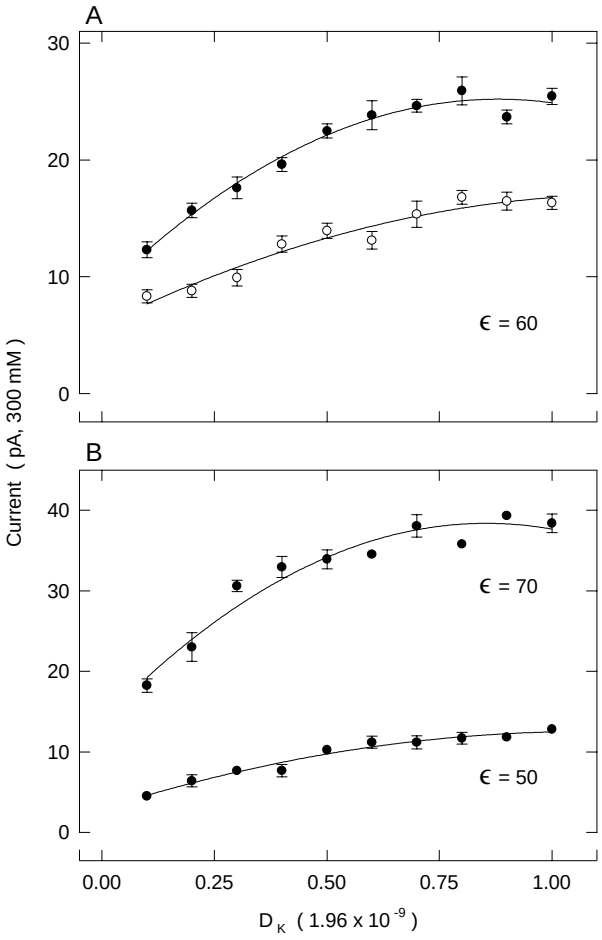

Figure 8.6: Effects of the diffusion coefficient on conductance. The diffusion coefficient of potassium ions in the selectivity filter, extending from $z = 7.5$ to 25 Å, is progressively lowered from the bulk value of 1.96×10^{-9} m^2/s and its effect on conductance is examined. (A) The outward (filled circles) and inward (open circles) current is plotted against diffusion coefficient in the selectivity filter, with $\epsilon = 60$ and an applied potential of 200 mV. (B) The outward current is plotted against diffusion coefficient in the selectivity filter for $\epsilon = 70$ (upper curve) and 50 (lower curve). Each point in (A) and (B) is derived from a simulation period of 1 μs.

(B). The filled and open circles in (A) represent, respectively, the outward and inward currents. The applied potential across the channel and the ionic concentration in the reservoir are kept constant at 200 mV and 300 mM, respectively. In contrast to bulk conductance, where current is proportional to the diffusion coefficient, the current in the potassium channel depends on D_{K} in a non-linear fashion. It decreases with decreasing D_{K} at a very slow rate at first (until D_{K} is reduced about 0.5 of its bulk value), and then becomes more or less proportional to D_{K}. When D_{K} is reduced to 1/3 of the bulk value, the current is only suppressed by about 30%.

8.3.4 Current-Voltage Relationships

The current-voltage relationships, shown in Fig. 8.7, are obtained with symmetrical solutions of 300 mM in both reservoirs. The diffusion coefficient in the selectivity filter is assumed to be the same as that in bulk electrolytes. Because the effective dielectric constant ϵ of the channel is unknown, we have determined the current-voltage curves, assuming ϵ to be 60, 70 and 80. The curves derived from these three conditions all reveal several distinct features. First, at any given applied potential, the outward current is larger than the inward current. Secondly, the magnitude of current across the channel at any given driving force increases steadily with increasing dielectric constant. The outward current at 100 mV is 6.7 ± 1.2, 11.8 ± 2.1 and 15.0 ± 1.0 pA when ϵ is assumed to be 60, 70 and 80, respectively (Fig. 8.7 A, B, & C). Because the current begins to saturate with increasing ionic concentrations (see later), the conductance at 150 mM K^+ will be slightly larger than 33, 59 and 75 pS at these three values of dielectric constants. Thirdly, the relationship is approximately linear when the applied potential is less than 100 mV, but it deviates systematically from Ohm's law with a further increase in the membrane potential. Given the results described in chapter 7 (see Fig. 7.8) and the preceding section (see Fig. 8.5), it seems reasonable to assume that this nonlinearity results from the presence of an energy barrier in the model channel.

To provide the solid lines in Fig. 8.7 we use a modification of the Pöschl-Teller function described in section 7.2.1:

$$I = \frac{\gamma V}{1 + \beta/[\exp(eV/V_{B1}) + \exp(-eV/V_{B2})]}, \tag{8.6}$$

where γ is the limiting conductance at large V, β is a dimensionless parameter and V_{B1} and V_{B2} are the right and left barrier heights. This function reduces to Ohm's law at very small and very large voltages, with conductance $\gamma/(1 + \beta/2)$ when the voltage is close to zero, and conductance γ when the voltage is positive and much greater than V_{B1} or negative and much smaller than V_{B2}. The solid lines are intended only to help visualize the conductance data, not to provide a physical interpretation, and for this reason the fit parameters are not given.

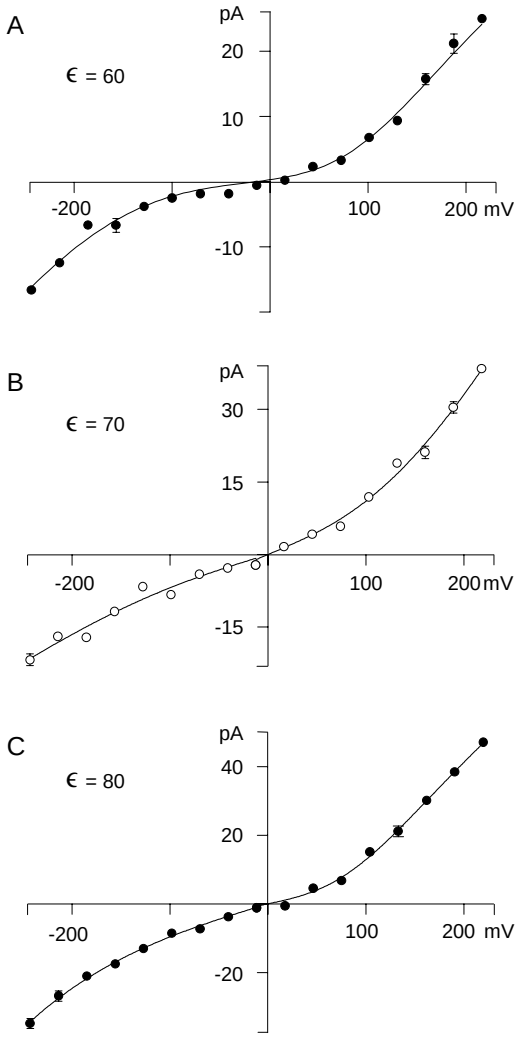

Figure 8.7: The current-voltage relationships. The current measured at various applied potentials is obtained with symmetrical solutions of 300 mM in both reservoirs. The solid lines fitted through data points are calculated from Eq. (8.6). The values of ϵ used for (A), (B) and (C) are 60, 70 and 80, respectively.

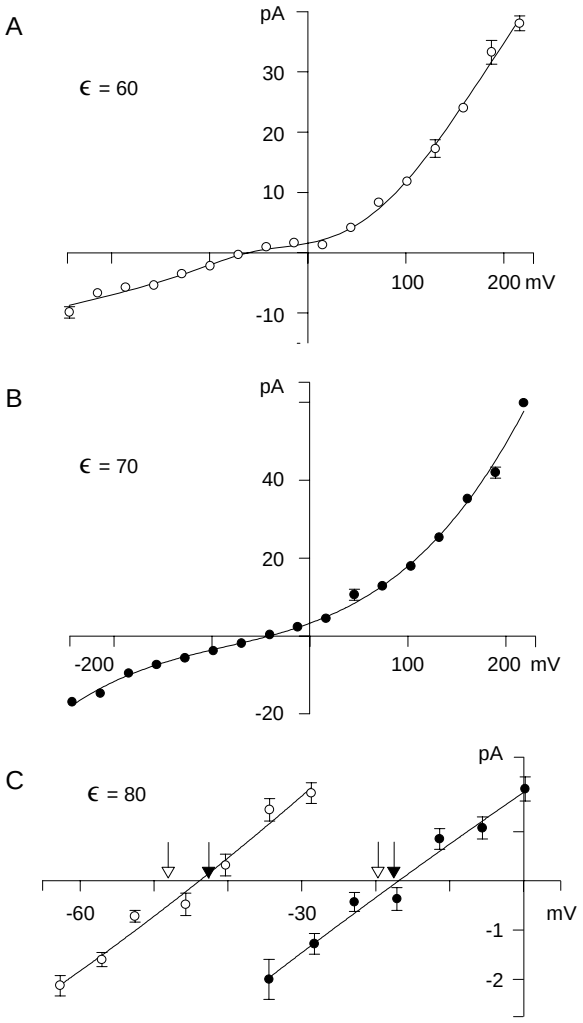

Figure 8.8: The current-voltage relationships. The current measured at various applied potentials is obtained with asymmetric solutions for $\epsilon = 60$ (A) and 70 (B). The concentration in the reservoir representing the intracellular space is 500 mM, whereas that representing the extracellular space is 100 mM. The solid lines drawn through the data are calculated with Eq. (8.6) multiplied by the Goldman factor, Eq. (8.7). For (C), obtained with $\epsilon = 80$, the measured concentrations in the intracellular and extracellular reservoirs are 482.0 mM and 71.5 mM (open circles) and 385.3 mM and 176.2 mM (filled circles). The open downward arrows indicate the reversal potential calculated from the Nernst equation. The predicted Nernst potentials taking the activity coefficients into account are indicated with filled downward arrows. The values of activity coefficients used for 71.5, 176.2, 386.3 and 482.0 mM are, respectively, 0.79, 0.73, 0.67 and 0.63.

The current-voltage relationships obtained with asymmetrical ionic solutions in the two reservoirs are shown in Fig. 8.8. The curves exhibited in the figure are obtained by assuming that ϵ in the channel is, respectively, 60 (A) and 70 (B). The ionic concentrations inside and outside are 500 mM and 100 mM. As expected, the asymmetry between the inward and outward currents is accentuated. As with the symmetrical solutions, an increase of ϵ from 60 to 70 causes an increase in the magnitude of currents flowing across the channel. The zero current of the two current-voltage relationships appears to be somewhere between -25 mV and -50 mV.

The solid lines fitted through the data points are obtained from Eq. (8.6) multiplied by a factor of the form:

$$\left[\frac{5-\exp(-eV/kT)}{1-\exp(-eV/kT)}\right]. \tag{8.7}$$

This factor comes from the Goldman-Hodgkin-Katz (GHK) equation which is usually used to fit the current-voltage curves of ion channels (see chapter 13 of Hille[31]). In the situation under discussion it is possible to express the GHK equation in the form:

$$I = KV\frac{1-5\exp(-eV/kT)}{1-\exp(-eV/kT)}, \tag{8.8}$$

where K is a constant and the factor of 5 arises from the outside to inside ratio of concentrations [18]. The GHK equation is derived under assumptions of a constant electric field and independent ion motion, which certainly do not apply to the model channel: as with the symmetric current-voltage results, the solid lines are only intended to help visualize the data.

To ascertain how closely the measured reversal potentials match with those predicted by the Nernst equation, we estimate currents flowing across the channel with two different ionic concentrations in the reservoirs and under various applied potentials. The concentrations of K^+ in the extracellular and intracellular aspects of the channel are computed from the average number of ions in the reservoirs throughout the simulation periods. The measured ionic concentrations in the left and right reservoirs in one series of simulations are 71.5 and 482.0 mM and in another series of simulations are 176.2 and 385.3 mM. Figure 8.8 shows the currents flowing across the channel at various applied potentials. Because the net current for these driving forces is small, the total simulation period of 3 μs is used to derive each data point. For the same reason, we use $\epsilon = 80$ for the effective dielectric constant of the channel, which results in a larger current flow. The reversal potential for each asymmetrical solutions is estimated by fitting a polynomial curve through the data points (solid line in Fig. 8.8 C). There are small but consistent discrepancies between the reversal potentials deduced from simulations and those predicted from the Nernst equation (indicated with open downward arrows). The zero currents occur at -45 mV and -17 mV when the

concentration ratios in the two reservoirs are, respectively, 6.7:1 and 2.2:1. The predicted reversal potentials are −48.1 mV and −19.7 mV. These discrepancies between the predicted and measured zero currents disappear if we take the activity coefficients of KCl at the measured ionic concentrations into account [73], as indicated by the filled arrows in Fig. 8.8 C. From a number of *I-V* curves obtained with asymmetrical solutions, we conclude that the zero current occurs at a potential predicted by the Nernst equation within the errors of simulations.

8.3.5 Ions in the channel

It is of interest to note where in the channel ions dwell predominantly. To compute the average number of ions inside the channel, we divide the channel into 32 thin sections and compute the time averages of potassium ions in each section. When a potential of 200 mV is applied so as to produce an outward current, two ions on average tend to reside in the channel. The preferred positions where ions dwell are in the selectivity filter at $z = 9.4$, 14.1 and 23.4 Å, as shown in Fig. 8.9 A. We note here that, although the histogram (Fig. 8.9 A) shows three distinct peaks near the selectivity filter, there are on average 1.5 ions in this region, as can be deduced by summing the heights of the bars. A similar sum for the peak near the intracellular entrance gives 0.5 ions, that is, an ion is present there 50% of the time. The preferential positions of the ions in the channel are shifted when the direction of the current is reversed by making inside negative with respect to outside. Under this condition, two ions mainly linger around $z = 9.4$ and 17.2 Å (Fig. 8.9 B). Thus, the preferred locations of ions in the channel depend on, among other factors, the direction and the strength of the applied field.

To better illustrate the behavior of ions under the influence of the electric and stochastic forces, we bisect the channel and denote the number of ions on the left and right hand sides by $[n_l, n_r]$. The occupation probabilities of distinct states are tabulated in Table 8.1 for five different potentials. At the bottom of the table, we give the average number of ions resident in the channel, which is about 2 regardless of the applied potential.

When the applied potential is 100 mV, which is relevant for the operation of the potassium channel, the most common occupation pattern is [0, 2]. That is, no ion is present in the first half (intracellular side) of the channel, while 2 ions are present in the second half (extracellular side). In addition to the patterns listed in Table 8.1, there are five other distinct patterns that are observed during the total simulation period of 0.5 μs (or 5 million time steps), but the frequencies of their occurrences are less than 1%. About 32,000 transitions occur between these patterns when the snapshot of the channel configuration is taken once every pico-second. The most common transitions are between [0, 2] and [0, 1], and between [1, 2] and [1, 1], which corresponds to the following process: driven by thermal energies, one of the

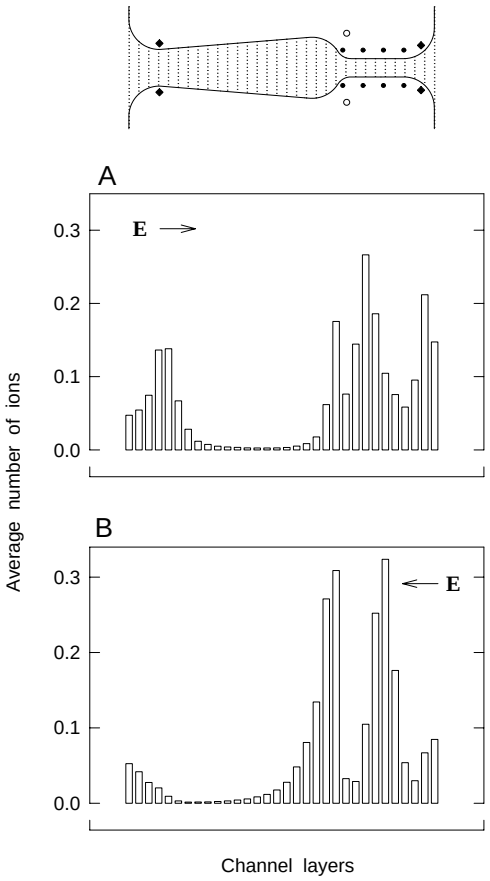

Figure 8.9: Concentrations of potassium ions in the channel. The channel is divided into 32 sections, as indicated in the inset, and the probability of ions present in each section over a simulation period of 0.5 μs is tabulated (bars). The ionic concentration in the reservoirs is 300 mM. The applied electric field in (A) is 2×10^7 V/m such that inside (left-hand side) is about 200 mV positive with respect to outside (right-hand side). The direction of the field is reversed to obtain the distribution shown in (B).

Table 8.1: Occupation probabilities of multi-ion states $[n_l, n_r]$ and the average number of ions in the channel $\langle n_l + n_r \rangle$ for different applied potentials.

$[n_l, n_r]$	-200 mv	-100 mV	100 mV	200 mV	300 mV
[0, 1]	3.5	3.4	12.1	15.2	17.2
[1, 1]	6.6	3.3	19.2	36.6	41.9
[0, 2]	78.9	78.2	49.2	30.3	25.3
[1, 2]	6.8	12.5	18.4	17.2	14.8
[0, 3]	3.8	2.4	-	-	-
Total %	99.6	99.8	98.9	99.3	99.2
$\langle n_l + n_r \rangle$	2.07	2.11	2.06	2.02	1.98

two ions in the second half of the channel escapes and then re-enters. The forward and backward transitions between these two sets account 64% of the total transitions. Less frequent transitions, occurring about 20% of all transitions, are between [0, 2] and [1, 2]. Finally, transitions between [0, 1] and [1, 1] account for 6% of the total transitions, while the forward transition between [1, 1] to [0, 2] accounts only for 0.3% of the total transitions.

8.3.6 Conductance-Concentration Relationships

If the transport of ions across the channel is determined by two independent processes, one of which depends on ionic concentration in the reservoir and one of which does not, then we expect that the current I will first increase with an increasing ionic concentration $[c]$ and then saturate, leading to a current-concentration relationship of the Michaelis-Menten form:

$$I = \frac{I_{\max}}{1 + K_s/[c]}, \tag{8.9}$$

so that the current approaches the saturation current $I_{\max}$ when $[c] \gg K_s$.

The magnitude of current across the channel plotted against the concentrations of potassium ions in the reservoirs, shown in Fig. 8.10, has the same shape as those observed experimentally [19, 59]. The two curves in (A) and (B) are the outward (filled circles) and inward (open circles) currents determined by assuming $\epsilon = 60$ (A) and $\epsilon = 70$ (B). The applied potentials used for (A) and (B) are, respectively, 200 mV and 150 mV. The conductance increases rapidly with an increasing ionic concentration at first and then saturates with a further increase in concentrations. The values of $I_{\max}$ and K_s

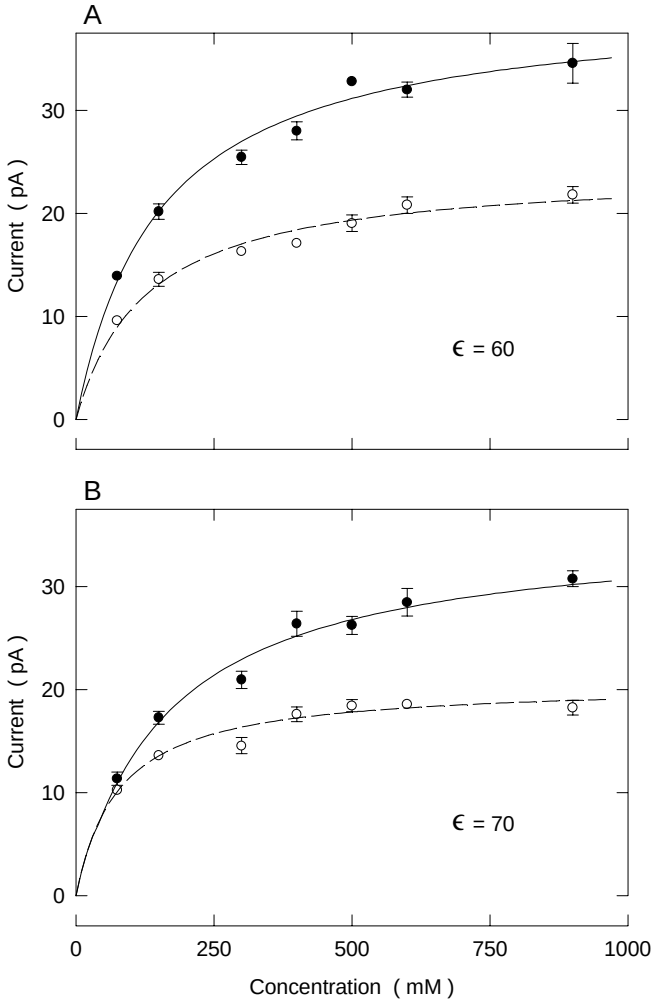

Figure 8.10: The conductance-concentration curves. The outward (filled circles) and inward (open circles) are obtained with symmetric solutions of varying concentrations in the two reservoirs. An applied potential of 200 mV and $\epsilon = 60$ are used for (A), while a potential of 150 mV and $\epsilon = 70$ are used for (B). The lines fitted through data points are calculated with Eq. (8.9).

used to fit the data points are: for A, 41 ± 1 pA and 151 ± 11 mM (outward currents), 24.2 ± 0.8 pA and 127 ± 11 mM; for B, 36 ± 1 pA and 169 ± 15 mM (outward currents) and 20.6 ± 0.5 pA and 77 ± 9 mM. The concentrations for half-maximal currents K_s we derive are slightly higher than the experimentally determined value for a potassium channel from sarcoplasmic reticulum by Coronado et al. [19].

8.4 Discussion

The fixed charges in the model, as adjusted to give maximum conductance, are somewhat smaller than expected. The helix dipoles have charges of 0.6×10^{-19} C (giving a dipole moment of 96×10^{-19} Cm over a length of 16 Å), compared to a value of 0.8×10^{-19} C (or 12×10^{-19} Cm per 1.5 Å) calculated from the structure of an alpha helix [32]. The mouth dipoles also have charges of 0.6×10^{-19} C, where 1.6×10^{-19} C (one elementary charge) might be expected. However, it is possible that in a ring of negative charges like this some of the side chains would become protonated and lose their negative charge [3]. If only two of the side chains were charged this would be consistent with four mouth dipole charges of 0.8×10^{-19} C, although two charges of 1.6×10^{-19} C would be a better representation. The carbonyl dipole charges of 0.6×10^{-19} C are as expected for a carbonyl group [11], but considering the crudeness of the filter model and the doubts about the electrostatic calculations in this region, this must be considered fortuitous.

The adjusted dielectric constant of 60 for the water in the channel is not in agreement with molecular dynamics studies. The dielectric constant must be at least 60 for the model channel's conductance to agree with experiment. When the dielectric constant is reduced to 40 the model channel effectively ceases to conduct, at least for realistic voltages. Molecular dynamics studies of water in spherical cavities [74] and narrow pores [66] suggest that the dielectric constant in confined spaces is substantially reduced compared to the bulk value.

Given the high dielectric constant the conductance characteristics of the model channel are reasonable, but they have not been compared in detail to the characteristics of real KcsA channels, as the comprehensive electrophysiological data required to do so is not yet available. The overall conductance of the model channel of around 33 pS (at 150 mM potassium and for $\epsilon = 60$) is in reasonable agreement with the experimental single channel conductance of around 40 pS (at 200 mM potassium) for the most common conductance state [67]. The model channel's conductance saturates in a manner similar to real potassium channels, showing the expected Michaelis-Menten form. The partial rectification shown by the model channel for symmetric solutions is interesting, as it is probably a multi-ion effect, but it is difficult to compare with results from real channels. Most potassium channels rectify,

but they do so by gating or ionic block, meaning that usually only one half of the current-voltage curve is available.

The x-ray crystallography done on the KcsA channel [21] shows three preferred ion positions: two in the selectivity filter and one in the central cavity. As described below, the model channel seems to have stable states in which the ions preferentially occupy particular positions depending on the applied voltage and the number of ions in the channel. If so this is consistent with the presence of sharply defined ion positions. The model channel contains an average of around two ions, but this is not in itself inconsistent with a channel with three ion positions, since the positions need not be occupied all the time. Nor is it inconsistent with ionic flux coupling results which suggest more than two ions in a conducting potassium channel [31], since the model channel may be more likely to conduct when it contains three ions, and almost certainly does not conduct when it contains one. Averages need to be interpreted with care; the real story is in the distribution and this is where a discrepancy shows up. In the model channel ions are concentrated in three areas, the selectivity filter, the cytoplasmic mouth, and the extracellular mouth, but never in the central cavity. This is a clear difference between the model channel and experimental results.

The likely causes of this discrepancy and the requirement for a high dielectric constant are inaccuracies in estimation of the electrostatic forces and problems with charge positions in the model channel. It is possible that the whole concept of modelling this channel with diffusion and electrostatics is wrong, and binding sites and hopping really are essential to its operation. This seems to us unlikely, however, since the model channel does show many similarities with the real channel, and multi-ion channels in general. Also the main problem, the lack of ion concentration in the central cavity, is in a region expected to be controlled by electrostatics and diffusion. Possible improvements to the electrostatics techniques are described in section 3.1.4, and these may be needed to provide an accurate description of the channel. Surprisingly the crude selectivity filter model works reasonably well, concentrating ions but allowing conductance by mutual destabilization. However, it may be that the small dipoles in the filter (which have some ability to move in the real channel) need to be represented in part by a locally increased dielectric constant rather than fixed charges. This could lead to a reduction of their long range effect in the central cavity without removing their ability to concentrate ions in the selectivity filter. Another possibility is that the arbitrarily placed counter charges in the mouth dipoles are too close to the negative charges surrounding the mouths of the channel. This could result in artificially sharp energy wells, leading to the barrier near the cytoplasmic mouth which seems to cause of the need for a large dielectric constant. A good start towards a better model channel would be to generate the shape and charge positions directly from the molecular structure, rather than in the rather ad-hoc way described above. This would also have the

advantage of reducing the number of adjustable parameters.

It seems we have constructed a working model of a multi-ion channel, albeit with an unrealistically high dielectric constant, but not a functional replica of the KcsA channel. After optimization of dipole strengths and the dielectric constant the model channel has a conductance comparable with the KcsA channel and other potassium channels. The concentration profiles (Fig. 8.9) and occupation probabilities (Table 8.1) show that the channel is usually occupied by two ions, and almost always by at least one, and this suggests that the channel contains at least two ions while conducting, since a single ion traversing the channel would leave it unoccupied when it exited. The current through the model channel saturates with increasing concentration (Fig. 8.10), as is characteristic of multi-ion channels. The channel also shows partial rectification with symmetrical solutions (Fig. 8.7), and it seems likely that this is an effect of the interactions between multiple ions within the channel.

So the model channel is multi-ion, and it shows conductance characteristics similar to real multi-ion channels. Its operation cannot, however, be explained in terms of hopping between binding sites as is usual for multi-ion channels. The model channel contains no binding sites, only a broad energy well (Fig 8.2 A), and all transport is by simulated diffusion. If an explanation of its conductance is desired, a different mechanism must be found. The existence of such a mechanism is useful because, if understood, it might lead to an alternative theory to RRT for conductance in multi-ion channels. Although RRT is the best available theory for summarizing experimental conductance data from a channel, and provides intuitive explanations for aspects of the the conductance of multi-ion channels that other theories cannot, the physical basis for its application to channels is doubtful (see section 2.1).

The concentration profile for an outward electric field (Fig. 8.9 A) shows that ions spend most of their time in particular regions of the model channel. Ions are concentrated in the selectivity filter and the cytoplasmic and extracellular mouth regions: they are rarely found in the inner pore or central cavity. Since ions must travel through the inner pore for the channel to conduct (which it does), the low concentration in this region suggests that the ions move through rapidly, and that transitions are relatively infrequent compared to the time spent in the channel mouths and selectivity filter. The concentration of ions in particular locations in the model channel (as evidenced by peaks in the concentration profiles) is consistent with the idea of binding sites. However, the single ion energy profile (Fig. 8.2 A, curve d) is smooth, showing only a broad energy well centred on the selectivity filter, and a very shallow well near the cytoplasmic mouth. There is no sign of the sharp localized wells that would indicate binding sites. This is not surprising given the method used to calculate the electrostatic potential (macroscopic electrostatics). The real channel may or may not contain ion binding sites,

but the concentration profiles are for the model channel and so the peaks in them cannot be explained in this way. A likely explanation is that the broad energy well attracts more that one ion to the channel, these ions change the energy profile experienced by each other (as they must), and that the interactions between the ions and the channel create temporary energy wells which confine the ions and cause the peaks. In other words the ions self-organize into particular positions in the channel depending on the number of ions present and the strength and direction of the applied field.

The multi-ion energy profiles (Figs. 8.2 and 8.5) support this interpretation. In Fig. 8.2 B energy profiles are calculated while another ion is fixed in the selectivity filter. The energy wells are sharper then that of the single ion profile (Fig. 8.2 A, curve d), and are consistent with two ions residing in particular locations at either end of the selectivity filter, and producing two separate peaks in the concentration profile. In Fig 8.2 C the energy profile is calculated for an ion entering the channel from the cytoplasmic end with two other ions already in the selectivity filter. These two ions have their positions altered to minimize energy as the first ion is moved into the channel (see section 8.2.1). The energy profile shows a well near the cytoplasmic mouth and a barrier centred on the inner pore. This is consistent with the peak in the concentration profile (Fig 8.9 A) just inside the cytoplasmic mouth, and the low concentrations in the inner pore. The height of the barrier in the multi-ion profile depends on the dielectric constant used for the simulation (Fig. 8.5 B): as the dielectric constant is increased, the inner pore and central cavity become more effective at hydrating the ion (as simulated by macroscopic electrostatics), and the barrier is reduced. This in turn increases the conductance of the channel (Fig. 8.5 C). Considering a single ion at at time does not provide such a direct explanation: as the dielectric constant increases, so does the depth of the well in the single ion profile, but it is not clear why this should cause the conductance of the channel to increase. The multi-ion energy profiles, based on the assumption of multiple ions self-organizing in the model channel, provide an explanation for the peaks in the concentration profiles, as well as the increase of conductance with increasing dielectric constant.

If the ions in the model channel self-organize into stable states, then transition between these states is probably by rapid diffusion, as indicated by the low concentration of ions in the inner pore. This suggests an overall picture of relatively stable states with rapid transitions between states. This is similar to RRT but with different physical causes. The occupation probabilities summarized in table 8.1 are a preliminary attempt to recognize possible states. Since the division between right and left halves of the channel is in the rarely occupied inner pore, an ion in the left half is probably in the well near the cytoplasmic mouth, while ions in the right half are probably in the selectivity filter or extracellular mouth. Unfortunately, while the occupation probabilities give some idea of possible states, they do

not give clear information about transitions between states. Some examples of transition probabilities are given in the text (section 8.3.5), but most of the transitions consist of ions briefly entering the mouth regions of the channel and immediately leaving. The problem is that the occupation probabilities do not represent identified stable states, but simply the very rough positions of the ions: each occupation pattern may represent zero or more stable states as well as various transient events. If there are stable states, then the patterns containing them will dominate the probabilities. Thus the distribution of probabilities in the table is some evidence that stable states exist in the model channel. Transitions between stable states are relatively rare, however, and cannot easily be picked out of the occupation probability data. Clearly a more sophisticated method of state identification and analysis is needed.

If ions in the model channel self-organize to form stable states this implies that the preferred positions of ions may change depending on the number of ions in the channel and the strength and direction of the electric field. There is evidence of this happening in the concentration profiles (Fig. 8.9) and the occupation probabilities (Table 8.1). The concentration profile for +200 mV (Fig. 8.9 A) shows a peak near the cytoplasmic mouth and one main peak in the centre of the selectivity filter, with subsidiary peaks on either side in the extracellular mouth and at the cytoplasmic end of the filter. In contrast the concentration profile for -200 mV (Fig. 8.9 B) shows two strong peaks in the selectivity filter, with not many ions elsewhere. This seems to correspond to the dominant [0, 2] pattern for occupancy under these conditions, which has about 80% probability. It is possible that this concentration profile represents a stable state which gives rise to the prominence of the [0, 2] pattern. The occupancy patterns for +200 mV have a more even spread of probabilities, indicating that the concentration profile may be an amalgam of several states. The patterns [1, 1] and [1, 2] make up over 50% of the probability, which could explain the peak near the cytoplasmic mouth. All four dominant patterns have ions in the right half of the channel: these ions may be in different places and this could explain the confusion of peaks in and near the selectivity filter.

In summary, this attempt to model the KcsA channel by Brownian dynamics simulation can only be regarded as a mixed success. The lack of ion concentration in the central cavity is a major deviation from experimental results, and the requirement for a large dielectric constant is probably wrong. However, the model channel has many similarities to the real channel. It has comparable conductance, and current through it saturates as in a real potassium channel. It also has sharp concentrations of ions in the selectivity filter similar to those in the KcsA channel. The values of the fixed charges, fitted to maximize conductance, are quite reasonable. These similarities suggest that the basic approach is sound, but that the model channel needs to be improved and made closer to the experimental structure, and that methods

of estimating the electrostatic forces need to be improved. Nevertheless, the effort has established that a model based on diffusion and electrostatics can produce a working multi-ion channel. In addition the way that the model channel seems to conduct by states and transitions may provide insight into conductance in multi-ion channels in general, and the reasons for the success of RRT in channels despite its dubious physical assumptions.

Chapter 9

Conclusion

The major technical challenge of this project was the production of fast, flexible, and accurate solutions to Poisson's equation. The iterative method is flexible but slow: it produces solutions for a wide variety of channel shapes, but can not produce these solutions quickly enough to allow useful BD simulations. The analytical method is faster and more accurate, but is limited to a toroidal channel boundary, and is still not quick enough for a BD simulation to predict conductance. The lookup table method gives access to the flexible solutions of the iterative method with sufficient speed to allow long BD simulations capable of predicting conductance. Although the analytical method might seem to be rendered obsolete, it is still very useful for checking the iterative and lookup table methods. The ability to compare solutions of Poisson's equation arrived at by completely different methods gives us a high level of confidence in the correct operation of our programs.

When used in Brownian dynamics simulations, these techniques for rapidly solving Poisson's equation produce quantitative predictions from model channels. The results from a single ion channel show that a narrow pore through a low dielectric medium presents a large energy barrier to permeating ions. Dipoles in the channel wall are needed to overcome this barrier, which is not removed by the presence of counter-ions free to diffuse. The results for a multi-ion channel show reasonable agreement with the conductance characteristics of real channels. They also suggest that multiple ions form states in the channel, with permeation occurring by transition between these states. Although complicated and computer intensive, our theory of conductance in ion channels is based on physical principles, and makes quantitative predictions from channel structure. In addition, the predictions made from an experimentally based channel model are at least similar to the expected values.

Despite this progress, there are many improvements that could be made to the theory, and much more work that should be done. An obvious need is for detailed comparison with experimental conductance results, to rigor-

ously test the theory. One difficulty here is finding good conductance data and structural data for the same channel. Now that the structure of the KcsA channel has been determined, this channel will likely become the subject of many experimental studies, so this is one good prospect. Another approach is structural modelling, attempting to match the experimental characteristics of a channel by guessing the structure. This requires a good understanding of how changes to the structure of the model affect its conductance, an understanding that we do not yet have. It also tends to rely on the accuracy of predictions from the theory, rather than verifying these predictions. Nevertheless, attempts at structural modelling may draw attention to weaknesses in our theory and techniques, and start to produce an intuitive understanding of the link between channel structure and conductance.

Improvements could be made to the iterative and lookup table methods, and the Brownian dynamics techniques. A new iterative algorithm based on a three dimensional grid would be desirable, as it would be able to accommodate changes in dielectric constant throughout the simulation in a self-consistent way. Some difficulties would be dealing with a smoothly curving dielectric boundary, and providing enough accuracy in the critical neck region of the channel. The lookup table algorithms need to be revised, to avoid the interpolation errors that can occur at the mouth of the channel, to improve the accuracy of interpolation for the 2d table, and perhaps to reduce the size of the tables to the extent that the algorithm is efficient on a RISC architecture machine. While the basic BD algorithm is a good one, able to cope with timesteps of any length, the algorithms describing the boundaries of the simulation are somewhat arbitrary. Better stochastic boundaries would allow the electro-chemical potentials of the reservoirs to be set, rather than estimated. Note that in Fig 8.8 the concentrations in the reservoirs have to measured from the simulations in order to correctly predict the reversal potential. The reflective boundaries and ion exclusion algorithms (section 5.3.2) are also undesirable. This problem could be solved by an adaptive timestep algorithm that varied the timestep from long to short depending on the proximity of ions to each other or the boundary. Such an algorithm would allow the reflective boundaries to be replaced by short range forces.

However, one of the ideas produced by the current algorithms shows great promise for future research, perhaps of more significance than making incremental improvements the existing theory. The observation that the model potassium channel may exhibit states and transition probabilities raises the prospect of providing reaction rate theory with a physical basis in channels, perhaps resulting in a simple theory of channel conductance with better explanatory power than a complex simulation. The first step would be to confirm the link between RRT and the potassium channel model, by doing an RRT analysis of the model's conductance, and comparing this to an improved state analysis of the movement of ions in the model channel.

Turning such a link into a useful theory would be harder, as diffusion over a barrier is theoretically much more complicated than hopping over a barrier. In kinetic hopping, energy is conserved, so the probability of crossing depends only on the barrier's height. Diffusion, however, is a dispersive process, and the shape and width of the barrier affect the probability of crossing. Nevertheless, this avenue should be pursued.

Bibliography

[1] M. Abramowitz and I. A. Stegun. *Handbook of Mathematical Functions*. Dover, New York, 1965.

[2] D. J. Adams, T. M. Dwyer, and B. Hille. The permeability of the endplate channel to monovalent and divalent metal cations. *Journal of General Physiology*, 75:493–510, 1980.

[3] C. Adcock, G. R. Smith, and M. S. P. Sansom. Electrostatics and ion selectivity of ligand-gated channels. *Biophysical Journal*, 75:1121–1222, 1998.

[4] M. P. Allen and D. J. Tildesley. *Computer Simulation of Liquids*. Clarendon Press, Oxford, 1987.

[5] T. W. Allen, S. Kuyucak, and S.-H. Chung. The effect of hydrophobic and hydrophilic channel walls on the structure and diffusion of water and ions. *Journal of Chemical Physics*, 111:7985–7999, 1999.

[6] T. W. Allen, S. Kuyucak, and S.-H. Chung. Molecular dynamics study of the KcsA potassium channel. *Biophysical Journal*, 77:2502–2516, 1999.

[7] P. W. Atkins. *Physical Chemistry*. Oxford University Press, Oxford, fifth edition, 1994.

[8] S. Bek and E. Jakobsson. Brownian dynamics study of a multiply-occupied cation channel: Application to understanding permeation in potassium channels. *Biophysical Journal*, 66:1028–1038, 1994.

[9] H. J. C. Berendsen, J. P. M. Postma, W. F. van Gunsteren, and J. Hermans. Interaction models for water in relation to protein hydration. In B. Pullman, editor, *Intermolecular Forces*, number 14 in Jerusalem Symposium on Quantum Chemistry and Biochemistry, pages 331–342. D. Reidel Publishing Company, Dordrecht, Holland, 1981.

[10] J. O'M. Bockris and A. K. N. Reddy. *Modern Electrochemistry*, volume 1. Plenum Press, New York, 1970.

[11] B. R. Brooks, R. E. Bruccoleri, B. D. Olafson, D. J. States, S. Swaminathan, and M. Karplus. CHARMM: a program for macromolecular energy, minimization and dynamic calculations. *Journal of Computational Chemistry*, 4:187–217, 1983.

[12] F. Buda, G. L. Chiarotti, R. Car, and M. Parrinello. Proton diffusion in silicon. *Physical Review Letters*, 63:294–297, 1989.

[13] R. Car and M. Parrinello. Unified approach for molecular dynamics and density-functional theory. *Physical Review Letters*, 55:2471–2474, 1985.

[14] D. Chen, J. Lear, and R. Eisenberg. Permeation through an open channel: Poisson-Nernst-Plank theory of a synthetic ion channel. *Biophysical Journal*, 72:97–116, 1997.

[15] D. Chen, Le Xu, A. Tripathy, G. Meissner, and B. Eisenberg. Permeation through the calcium release channel of cardiac muscle. *Biophysical Journal*, 73:1337–1354, 1997.

[16] D. Chen, Le Xu, A. Tripathy, G. Meissner, and B. Eisenberg. Selectivity and permeation through the calcium release channel of cardiac muscle: Alkali metal ions. *Biophysical Journal*, 76:1346–1366, 1999.

[17] S.-W Chiu, J. A. Novotny, and E. Jakobsson. The nature of ion and water barrier crossings in a simulated ion channel. *Biophysical Journal*, 64:98–108, 1993.

[18] S.-H. Chung, M. Hoyles, T. Allen, and S. Kuyucak. Study of ionic currents across a model membrane channel using Brownian dynamics. *Biophysical Journal*, 75:793–809, 1998.

[19] R. Coronado, R. L. Rosenberg, and C. Miller. Ionic selectivity, saturation, and block in a K^+-selective channel from sarcoplasmic reticulum. *Journal of General Physiology*, 76:425–446, 1980.

[20] J. A. Dani and D. G. Levitt. Diffusion and kinetic approaches to describe permeation in ionic channels. *Journal of Theoretical Biology*, 146:289–301, 1990.

[21] D. A. Doyle, J. M. Cabral, R. A. Pfuetzner, A. Kuo, J. M. Gulbis, S. L. Cohen, B. T. Chait, and R. MacKinnon. The structure of the potassium channel: Molecular basis of K^+ conduction and selectivity. *Science*, 280:69–73, 1998.

[22] T. M. Dwyer, D. J. Adams, and B. Hille. The permeability of the endplate channel to organic cations in frog muscle. *Journal of General Physiology*, 75:469–492, 1980.

[23] R. S. Eisenberg. Computing the field in proteins and channels. *The Journal of Membrane Biology*, 150:1–25, 1996.

[24] R. S. Eisenberg. From structure to function in open ionic channels. *The Journal of Membrane Biology*, 171:1–24, 1999.

[25] H. Eyring. The activated complex in chemical reactions. *Journal of Chemical Physics*, 3:107–115, 1935.

[26] H. Eyring. Viscosity, plasticity, and diffusion as examples of absolute reaction rates. *Journal of Chemical Physics*, 4:283–291, 1936.

[27] E. M. Fenwick, A. Marty, and E. Neher. A patch-clamp study of bovine chromaffin cells and of their sensitivity to acetylcholine. *Journal of Physiology*, 331:577–597, 1982.

[28] R. P. Feynman, R. B. Leighton, and M. Sands. *The Feynman Lectures on Physics*, volume II. Addison-Wesley Publishing Company, Reading, Massachusetts, 1964.

[29] J. Hermans, H. J. C. Berendsen, W. F. van Gunsteren, and J. P. M. Postma. A consistent empirical potential for water-protein interactions. *Biopolymers*, 23:1513–1518, 1984.

[30] T. L. Hill. *Statistical Mechanics*. McGraw-Hill, New York, 1956.

[31] B. Hille. *Ionic Channels of Excitable Membranes*. Sinauer Associates, Sunderland, Massachusetts, second edition, 1992.

[32] W. G. J. Hol, P. T. van Duijnen, and H. J. C. Berendsen. The α-helix dipole and the properties of proteins. *Nature*, 273:443–446, 1978.

[33] M. Hoyles, S. Kuyucak, and S.-H. Chung. Energy barrier presented to ions by the vestibule of the biological membrane channel. *Biophysical Journal*, 70:1628–1642, 1996.

[34] M. B. Jackson and H. Lecar. Single postsynaptic channel currents in tissue cultured muscle. *Nature*, 282:863–864, 1979.

[35] E. Jakobsson. Hierarchies of simulation methods in understanding biomolecular function. In *International Journal of Quantum Chemistry*, number 20 in Quantum Biology Symposium, pages 25–36. John Wiley & Sons, Inc., 1993.

[36] P. C. Jordan. Energy barriers for passage of ions through channels. Exact solution of two electrostatic problems. *Biophysical Chemistry*, 13:203–212, 1981.

[37] P. C. Jordan. Effect of pore structure on energy barriers and applied voltage profiles. I. Symmetrical channels. *Biophysical Journal*, 45:1091–1100, 1984.

[38] P. C. Jordan. Effect of pore structure on energy barriers and applied voltage profiles. II. Unsymmetrical channels. *Biophysical Journal*, 45:1101–1107, 1984.

[39] P. C. Jordan. Ion permeation and chemical kinetics. *Journal of General Physiology*, 114:601–603, 1999.

[40] M. Karplus. Molecular dynamics simulations in biology. *Nature*, 347:631–639, 1990.

[41] M. G. Kurnikova, R. D. Coalson, P. Graf, and A. Nitzan. A lattice relaxation algorithm for three-dimensional Poisson-Nernst-Plank theory with application to ion transport through the gramicidin A channel. *Biophysical Journal*, 76:652–656, 1999.

[42] S. Kuyucak, M. Hoyles, and S.-H. Chung. Analytical solutions of poisson's equation for realistic geometrical shapes of membrane ion channels. *Biophysical Journal*, 74:22–36, 1998.

[43] D. G. Levitt. Electrostatic calculations for an ion channel. I. Energy and potential profiles and interactions between ions. *Biophysical Journal*, 22:209–219, 1978.

[44] D. G. Levitt. Electrostatic calculations for an ion channel. II. Kinetic behavior of the gramicidin A channel. *Biophysical Journal*, 22:221–248, 1978.

[45] S. C. Li, M. Hoyles, S. Kuyucak, and S.-H. Chung. Brownian dynamics study of ion transport in the vestibule of membrane channels. *Biophysical Journal*, 74:37–47, 1998.

[46] J. D. Love. The dielectric ring in a uniform, axial, electrostatic field. *Journal of Mathematical Physics*, 13:1297–1304, 1972.

[47] R. M. Lynden-Bell and J. C. Rasaiah. Mobility and solvation of ions in channels. *Journal of Chemical Physics*, 105:9266–9280, 1996.

[48] D. Marx, M. Sprik, and M. Parrinello. Ab initio molecular dynamics of ion solvation: The case of Be^{2+} in water. *Chemical Physics Letters*, 273:360–366, 1997.

[49] R. J. Maurer. Deviations from ohm's law in soda lime glass. *Journal of Chemical Physics*, 9:579–584, 1941.

[50] L. M. Milne-Thompson. *The Calculus of Finite Differences*. Macmillan and Co., Ltd., London, 1960.

[51] L. A. Moran, K. G. Scrimgeour, H. R. Horton, R. S. Ochs, and J. D. Rawn. *Biochemistry*. Neil Patterson Publishers/Prentice-Hall, Inc., Englewood Cliffs, NJ, second edition, 1994.

[52] P. M. Morse and H. Feshbach. *Methods of Theoretical Physics*, volume II. McGraw-Hill, New York, 1953.

[53] W. Nonner, D. P. Chen, and B. Eisenberg. Progress and prospects in permeation. *Journal of General Physiology*, 113:773–782, 1999.

[54] W. Nonner and B. Eisenberg. Ion permeation and glutamate residues linked by Poisson-Nernst-Plank theory in l-type calcium channels. *Biophysical Journal*, 75:1287–1305, 1998.

[55] United States National Bureau of Standards Computation Laboratory. *Tables of Associated Legendre Functions*. Columbia University Press, New York, 1945.

[56] A. Parsegian. Energy of an ion crossing a low dielectric membrane: Solutions to four relevant electrostatic problems. *Nature*, 221:844–846, 1969.

[57] M. B. Partenskii and P. C. Jordan. Nonlinear dielectric behaviour of water in transmembrane ion channels: Ion energy barriers and the channel dielectric constant. *Journal of Physical Chemistry*, 96:3906–3910, 1992.

[58] W. H. Press, B. P. Flannery, S. A. Teukolsky, and W. T. Vetterling. *Numerical Recipes*. Cambridge University Press, New York, second edition, 1992.

[59] J. L. Rae, R. A. Levis, and R. S. Eisenberg. Ionic channels in ocular epithelia. In T. Narahashi, editor, *Ion Channels*, volume 1, pages 283–327. Plenum Press, New York, 1988.

[60] A. A. Rashin and B. Honig. Reevaluation of the born model of ion hydration. *Journal of Physical Chemistry*, 89:5588–5593, 1985.

[61] F. Reif. *Fundamentals of Statistical and Thermal Physics*. McGraw-Hill Kogakusha, Tokyo, 1965.

[62] D. K. Remler and P. A. Madden. Molecular dynamics without effective potentials via the Car-Parrinello approach. *Molecular Physics*, 70:921–966, 1990.

[63] R. A. Robinson and R. H. Stokes. *Electrolyte Solutions*. Butterworths Scientific Publications, London, 1959.

[64] B. Roux and M. Karplus. Ion transport in a model gramicidin channel: Structure and thermodynamics. *Biophysical Journal*, 59:961–981, 1991.

[65] M. S. P. Sansom, C. Adcock, and G. R. Smith. Modelling and simulation of ion channels: Applications to the nicotinic acetylcholine receptor. *Journal of Structural Biology*, 121:246–262, 1998.

[66] M. S. P. Sansom, G. R. Smith, C. Adcock, and P. C. Biggin. The dielectric properties of water within model transbilayer pores. *Biophysical Journal*, 73:2404–2415, 1997.

[67] H. Schrempf, O. Schmidt, R. Kümmerlen, S. Hinnah, D. Müller, M. Betzler, T. Steinkamp, and R. Wagner. A prokaryotic potassium ion channel with two predicted transmembrane segment from *Steptomyces lividans*. *The EMBO Journal*, 14:5170–5178, 1995.

[68] G. R. Smith and M. S. P. Sansom. Dynamic properties of Na^+ ions in models of ion channels: a molecular dynamics study. *Biophysical Journal*, 75:2767–2782, 1997.

[69] F. H. Stillinger and A. Rahman. Improved simulation of liquid water by molecular dynamics. *Journal of Chemical Physics*, 60:1545–1557, 1974.

[70] C. Toyoshima and N. Unwin. Ion channel of acetylcholine receptor reconstructed from images of postsynaptic membranes. *Nature*, 336:247–250, 1988.

[71] N. Unwin. The structure of ion channels in membranes of excitable cells. *Neuron*, 3:665–676, 1989.

[72] W. F. van Gunsteren and H. J. C. Berendsen. Algorithms for Brownian dynamics. *Molecular Physics*, 45:637–647, 1982.

[73] R. C. Weast, editor. *CRC Handbook of Chemistry and Physics*. CRC Press, Inc., Boca Ration, Florida, 1983.

[74] L. Zhang, H. T. Davis, D. M. Kroll, and H. S. White. Molecular dynamics simulations of water in a spherical cavity. *Journal of Physical Chemistry*, 99:2878–2884, 1995.